

# ALMA-IMF

## XV The core mass function in the high-mass star-formation regime

F. Louvet<sup>1,2</sup>, P. Sanhueza<sup>3,4</sup>, A. Stutz<sup>5</sup>, A. Men'shchikov<sup>6</sup>, F. Motte<sup>1</sup>, R. Galván-Madrid<sup>7</sup>, S. Bontemps<sup>8</sup>, Y. Pouteau<sup>1</sup>, A. Ginsburg<sup>9</sup>, T. Csengeri<sup>8</sup>, J. Di Francesco<sup>10</sup>, P. Dell'Ova<sup>11</sup>, M. González<sup>6</sup>, P. Didelon<sup>6</sup>, J. Braine<sup>8</sup>, N. Cunningham<sup>1</sup>, B. Thomasson<sup>1</sup>, P. Lesaffre<sup>11</sup>, P. Hennebelle<sup>6</sup>, M. Bonfand<sup>25</sup>, A. Gusdorf<sup>11,12</sup>, R. H. Álvarez-Gutiérrez<sup>5</sup>, T. Nony<sup>7</sup>, G. Busquet<sup>13,14,15</sup>, F. Olguin<sup>16</sup>, L. Bronfman<sup>2</sup>, J. Salinas<sup>5</sup>, M. Fernandez-Lopez<sup>17</sup>, E. Moraux<sup>1</sup>, H.L. Liu<sup>18</sup>, X. Lu<sup>19</sup>, V. Hwei-Ru<sup>16</sup>, A. Towner<sup>26</sup>, M. Vaille-Manet<sup>8</sup>, N. Brouillet<sup>8</sup>, F. Herpin<sup>8</sup>, B. Lefloch<sup>8</sup>, T. Baug<sup>21</sup>, L. Maud<sup>22</sup>, A. Lopez-Sepulcre<sup>1,23</sup>, and B. Svodoba<sup>24</sup>

(Affiliations can be found after the references)

Received January 25, 2023; accepted July 25, 2024

### ABSTRACT

The stellar initial mass function (IMF) is critical to our understanding of star formation and the effects of young stars on their environment. On large scales, it enables us to use tracers such as UV or H $\alpha$  emission to estimate the star formation rate of a system and interpret unresolved star clusters across the universe. So far, there is little firm evidence of large-scale variations of the IMF, which is thus generally considered "universal". Stars form from cores and it is now possible to estimate core masses and compare the core mass function (CMF) with the IMF, which it presumably produces. The goal of the ALMA-IMF large program is to measure the core mass function at high linear resolution (2700 au) in 15 typical Milky Way protoclusters spanning a mass range of  $2.5 \times 10^3$  to  $32.7 \times 10^3 M_{\odot}$ . In this work, we used two different core extraction algorithms to extract  $\approx 680$  gravitationally bound cores from these 15 protoclusters. We adopt per core temperature using the temperature estimate from the PPMAP Bayesian method. A power-law fit to the CMF of the sub-sample of cores above the  $1.64 M_{\odot}$  completeness limit — 330 cores — through the maximum likelihood estimate technique yields a slope of  $1.97 \pm 0.06$ , significantly flatter than the 2.35 Salpeter slope. Assuming a self-similar mapping between the CMF and the IMF, this result implies that these 15 high-mass protocluster will generate atypical IMFs. This sample is the largest to date produced and analysed self-consistently, derived at matched physical resolution, with per-core temperature estimates and cores as massive as  $150 M_{\odot}$ . We provide the raw source extraction catalogues and the source derived size, temperature, mass, and spectral indices in the 15 protoclusters.

**Key words.** Stars: formation – Infrared: ISM – Submillimeter: ISM – Methods: data analysis – Techniques: image processing

### 1. Introduction

In 1955, Edwin Salpeter reported that the high-mass tail of the initial mass function of stars, the IMF, could be represented by a power law in the form  $\frac{dN}{dM} \propto M^{-\alpha}$  with  $\alpha = 2.35$ . Since then, numerous studies reported its universality (see the review by Bastian et al. 2010), and studied its origin (e.g. Hennebelle & Chabrier 2008). To investigate the origin of the IMF, astronomers studied the fragmentation of molecular clouds, in the form of small substructures ( $\lesssim 0.03$  pc) — the cores — and the link between the core mass function (CMF) and the IMF (e.g. Motte et al. 1998; Fiorellino et al. 2021). Because of observational limitations, until 2018 these studies focused mostly on nearby clouds ( $\sim 140$ – $400$  pc), which mainly form low- and intermediate-mass stars; they all reported CMF slopes at the high-mass end compatible with the slope of the IMF, suggesting that the IMF directly inherits its shape from the CMF (e.g. Alves et al. 2007; Könyves et al. 2010).

In 2018, taking advantage of the angular resolution and sensitivity of the Atacama Large Millimetre/submillimetre Array (ALMA), Motte et al. (2018) studied the high-mass protocluster W43-MM1, at a distance of  $\approx 5.5$  kpc. They reported a CMF with a high-mass tail flatter than the canonical IMF, with  $\alpha = 1.96 \pm 0.13$ . Since then, other teams reported similar results in other high-mass protoclusters but often using single pointing ob-

servations, thus narrow fields not imaging pc-scale clouds (e.g. Liu et al. 2018; Cheng et al. 2018; Kong 2019; O'Neill et al. 2021). These results cast doubt on the universality of the IMF or on the direct link between the CMF and the IMF, or even on both. However, the comparison of core samples between these studies — which are captured at different evolutionary stages — becomes complex or impossible when the observations are carried out at disparate physical resolutions and/or sensitivities. Thus, it became imperative to obtain a sample of high-mass protoclusters representative of the Milky Way observed homogeneously.

To directly address this, we present in this article the results of the ALMA-IMF Large Program (PIs: F. Motte, A. Ginsburg, F. Louvet, P. Sanhueza). ALMA-IMF observed 15 high-mass protoclusters at comparable sensitivity and physical resolution. The main driver of the protocluster selection is a mass criteria, first choosing protoclusters with inner parts of at least  $500 M_{\odot}$ , as described in detail in the Sect. 2.1 of Motte et al. (2022). A second criteria is the distance of the protoclusters. Not too close by ( $> 2$  kpc) to permit imaging a large area with mosaic observations and not too far ( $< 6$  kpc) to prevent for excessive integration time. Our final sample consists of 15 protoclusters that were observed with continuum sensitivity below 60 mK at 1.3 mm, and at similar physical resolution ( $\sim 2$  kau).

In this article, we determine and analyse the combined CMF of all 15 protoclusters from ALMA-IMF. We show the 1.3 and

3 mm continuum images in Sect. 2, first presented in Ginsburg et al. (2022). We describe the source extraction in Sect. 3. We describe the source selection and core mass derivation in Sect. 4, paying special attention to freefree emission and temperature of the cores. We present the global CMF for all 15 fields. We discuss our results regarding the current knowledge about CMF in Sect. 6, and we summarize our conclusions in Sect. 7.

## 2. Observations

The data were taken from the ALMA-IMF large program (Project ID: 2017.1.01355.L), entitled *ALMA transforms our view of the origin of stellar masses*. Motte et al. (2022), hereafter referred to as Paper I, described the project, its choice of targets, datasets, objectives and first results. Ginsburg et al. (2022), hereafter referred to as Paper II, described the reduction pipeline for the continuum emission maps at 1.3 mm and 3 mm in the ALMA-IMF sample. Paper II presented two versions of the continuum maps: the `BSENS` and the `CLEANEST`. The `BSENS` maps were constructed using the full range of the continuum spectral windows — which may include significant molecular emission, especially toward hot cores. The `CLEANEST` maps were constructed flagging all channels contaminated by molecular emission (see Fig. 3 in Paper II). Since we wish to assemble the most reliable sample of cores, we use the `CLEANEST` continuum maps, publicly available on the ALMA-IMF website<sup>1</sup>. Table 1 lists the fifteen regions investigated by ALMA-IMF together with observational characteristics, taken from Papers I and II, relevant to the present paper. We refer to Paper I for an in depth description of the 15 regions.

## 3. Source extraction

### 3.1. Extraction tools

To extract sources in the continuum emission maps, we used two extraction tools: *getsf* (v210414, Men'shchikov 2021b) and *GExt2D* (v210603, Bontemps et al., in prep.). This approach permits us to assess the biases inherent to our source extraction algorithms.

The multi-scale, multi-wavelength source and filament extraction method *getsf* supersedes the previous algorithms *getsources*, *getfilaments*, and *getimages* (Men'shchikov et al. 2012; Men'shchikov 2013, 2017, respectively). The *getsf* method separates the structural components of sources, filaments, and background in the observations into independent images of the different components. Source and filament extraction are done with their respective images, where the contributions of the other components are largely removed. For more details on *getsf*, illustrations of its applications, quantitative extraction performance, and comparisons with *getsources*, readers are referred to Men'shchikov (2021a,b).

*GExt2D* is based on the same idea as the *cutex* tool (Molinari et al. 2011). It uses as a first step the second derivative of the maps to identify the locations of maximum curvature as indicative of compact sources. It starts from the strongest curvatures down to fainter and shallower fluctuations close to the ones expected from measured local noise. The second step involves source boundaries identification and removal of background emission as the interpolated values in the map inside the boundaries. The third step corresponds to automated Gaussian fitting at each locations of compact sources after subtracting the derived background.

<sup>1</sup> <https://www.almaimf.com/>

### 3.2. Source extraction at native angular resolutions

With both *getsf* and *GExt2D*, the source extraction strategy has the same two steps. Firstly, we detected source candidates in the continuum images at 1.3 mm (Band 6) without primary beam correction. These images have a homogeneous noise level across the entire field. This choice permits the detection of sources with a constant signal-to-noise ratio threshold. Secondly, we measured the sources' fluxes and sizes in the continuum maps at 1.3 mm and 3 mm (Band 3) after primary beam correction. This way, the fluxes we obtained account for any attenuation resulting from being farther from the phase centre of the fields. This strategy replicates that applied in Pouteau et al. (2022), hereafter referred to as Paper III, dedicated to the W43-MM2 and W43-MM3 protoclusters. Considering all 15 protoclusters together, we extracted 820 sources with *getsf*, and 930 with *GExt2D*. *GExt2D* detects the sources in the observed image, while *getsf* decomposes the image first and requires detecting a source in successive scales to validate its detection. Hence *getsf* is more conservative and extracts fewer sources than *GExt2D*.

The distances of the protoclusters range from 2.5 to 5.5 kpc (see Table 1 in Paper I). The ALMA-IMF large program aimed to image the 15 protoclusters with the same spatial resolution of 2100 au, requesting the corresponding angular resolution for each field. Despite this effort, the available antenna configurations at the observatory led to variations in the spatial resolutions by up to a factor of two (see Table 1 and Paper I). These variations in physical scale impact the size and mass of the sources one may extract. Indeed, Louvet et al. (2021) performed convolution tests on projected density cubes obtained from hydrodynamical simulations, plus column density maps created from *Herschel* observations, and showed that the sizes and integrated fluxes of extracted sources closely follow the size of the linear scale. The left panel of Fig. 1 shows a linear dependency between the mean source size and the linear resolution. To obtain a homogeneous sample of sources the data must be smoothed to a matched spatial resolution.

### 3.3. Source extraction at matched physical resolution

To extract a spatially homogeneous core sample, we smoothed the 1.3 and 3 mm maps to the lowest native resolution of  $\approx 2700$  au. We convolved each map with a Gaussian kernel whose width,  $\theta_{\text{conv}}$ , is calculated as:

$$\theta_{\text{conv}} = \sqrt{\left(\frac{2700 \text{ au}}{D}\right)^2 - \theta_{\text{native}}^2} \quad (1)$$

where  $D$  is the distance to the target expressed in parsecs, and  $\theta_{\text{native}}$  is the native angular resolution of the map. Table 2 lists the angular resolution of each field after smoothing. We present the smoothed continuum emission maps at 1.3 mm in Fig. 2.

We adopted the same strategy as explained in Sect. 3.2 to extract sources in the smoothed maps. In total, we retrieve about 680 sources with *getsf*, and 1020 with *GExt2D*<sup>2</sup>. Table 2 lists the number of sources extracted per field with both algorithms, Fig. 2 shows the sources extracted with *getsf* and Fig. C.1 shows the sources extracted with both algorithms. The right panel of Fig. 1 shows the sizes of the sources we extracted with *getsf*

<sup>2</sup> One can download the extraction catalogues from both *getsf* and *GExt2D*, at the native and smoothed angular resolutions on the website of the ALMA-IMF Large Program (<https://www.almaimf.com/>), and on CDS in a machine readable format.

Table 1: General properties of the ALMA-IMF fields.

Protocluster cloud name	Phase center		Evolutionary stage	$D$ [pc]	$\nu_{1.3\text{ mm}}$ [GHz]	$\theta$ [']	Scale [au]	max [']	$\sigma_{1.3\text{ mm}}$ [mK]	$\nu_{3\text{ mm}}$ [GHz]	$\sigma_{3\text{ mm}}$ [mK]
	RA[J2000] (1)	DEC[J2000] (1)	(1)	(1)	(2)	(3)	(4)	(5)	(6)	(2)	(6)
G327.29	15:53:08.130	-54:37:08.60	Young	2500	229.507	0.66	1650	8.3	25	101.776	5
G328.25	15:57:59.680	-53:57:57.43	Young	2500	227.575	0.55	1365	7.1	35	101.500	3
G337.92	16:41:10.620	-47:08:02.90	Young	2700	227.503	0.55	1475	6.6	15	101.602	23
G338.93	16:40:34.420	-45:41:40.60	Young	3900	229.226	0.54	2100	5.8	15	100.882	10
W43-MM1	18:47:47.000	-01:54:26.00	Young	5500	229.680	0.45	2470	12.0	26	99.759	17
W43-MM2	18:47:36.610	-02:00:51.10	Young	5500	227.597	0.47	2580	8.1	15	101.017	23
W43-MM3	18:47:41.460	-02:00:27.60	Intermediate	5500	228.931	0.49	2685	11.5	9	100.911	17
W51-E	19:23:44.180	14:30:29.50	Intermediate	5400	228.918	0.31	1650	4.5	60	101.426	26
G351.77	17:26:42.620	-36:09:22.47	Intermediate	2000	227.991	0.78	1560	8.9	21	100.228	16
G353.41	17:30:26.280	-34:41:51.67	Intermediate	2000	229.431	0.80	1600	9.1	14	100.547	9
G008.67	18:06:21.072	-21:37:14.84	Intermediate	3400	228.732	0.67	2270	9.1	22	100.526	14
G010.62	18:10:28.840	-19:55:48.30	Evolved	4950	229.268	0.47	2310	6.4	14	100.704	23
G012.80	18:14:13.370	-17:55:47.17	Evolved	2400	229.080	0.90	2155	9.5	20	100.680	21
G333.60	16:22:09.360	-50:06:00.87	Evolved	4200	229.062	0.56	2335	11.8	22	100.756	24
W51-IRS2	19:23:39.810	14:31:03.50	Evolved	5400	228.530	0.48	2575	7.0	13	101.263	24

**Notes.** (1) Phase center, evolutionary stage and distance to the region taken from Tables 1 and 4 of Paper I. (2) Central frequencies in Band 6 ( $\approx 1.3$  mm) and in Band 3 ( $\approx 3.0$  mm) taken from Table D.1 of Paper II. (3) Angular resolution in Band 6 (geometric average over the major and minor axis of the beam). (4) Spatial resolution on source in Band 6. (5) Largest angular scale recovered in Band 6. (6) Standard deviations of the noise level in Band 6 and in Band 3.

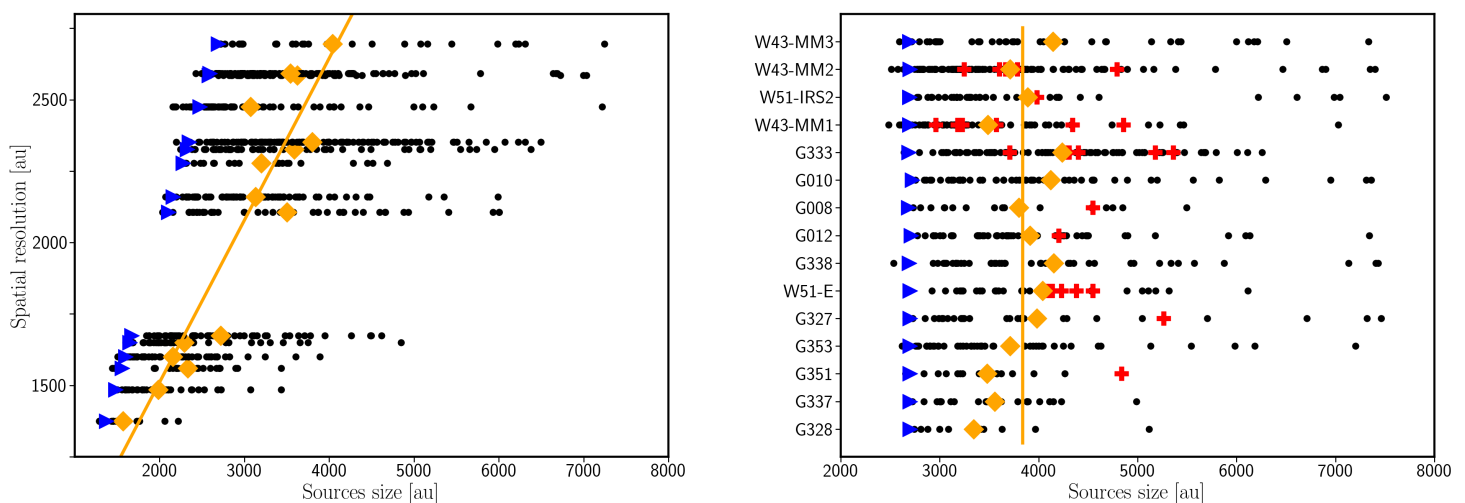


Fig. 1: Scatter plots of the source size (black dots), extracted with *getsf*, before (left) and after (right) smoothing the maps to a homogeneous spatial resolution of 2700 au. The blue triangles display the beam sizes. The orange diamonds display the mean sizes of sources. On the left panel, the  $y$ -axis is the linear scale (beam  $\times$  distance) of the maps in Band 6, and the orange line shows the fit to the mean source sizes distribution for each field. On the right panel, the orange line shows the mean core size of all 15 protoclusters and the red crosses illustrate the cores exceeding  $25 M_{\odot}$ .

for each field. The mean size is similar for each field with  $L = 3840 \pm 270$  au.<sup>3</sup>

## 4. Results

### 4.1. *getsf* versus *GExt2D* extraction methods

In total, we retrieve 677 sources with *getsf*, and 1020 with *GExt2D*. We see a good agreement between these extractions as  $\sim 80\%$  of the sources found by *getsf* are also found by *GExt2D* (Table 2). To compare the source flux measurements, we con-

<sup>3</sup> A similar figure for *GExt2D* extractions is shown in Appendix B.1.

Table 2: Resolutions, noise levels, and sources extracted after smoothing to a linear scale of 2700 au.

Protocluster cloud name	$\theta^{(1)}$ [ $''$ ]	$\sigma^{(2)}$ [mJy.beam $^{-1}$ ]	$\sigma^{(3)}$ [ $M_{\odot}$ ]	<i>getsf</i>	<i>GExt2D</i>	Common <sup>(4)</sup>	
G327.29	1.08	0.30	0.03	32	49	28	Table D.1
G328.25	1.08	0.19	0.02	11	26	9	Table D.2
G337.92	1.00	0.09	0.01	22	42	19	Table D.3
G338.93	0.69	0.12	0.03	42	50	31	Table D.4
W43-MM1	0.49	0.09	0.01	71	94	62	Table D.6
W43-MM2	0.49	0.11	0.06	40	34	27	Table D.9
W43-MM3	0.49	0.08	0.04	38	21	20	Table D.9
W51-E	0.50	0.06	0.03	31	75	22	Table D.10
G351.77	1.35	0.28	0.02	19	40	18	Table D.11
G353.41	1.35	0.19	0.02	46	68	39	Table D.12
G008.67	0.79	0.25	0.05	20	30	16	Table D.14
G010.62	0.55	0.12	0.03	50	59	37	Table D.15
G012.80	1.13	0.52	0.05	57	125	57	Table D.17
G333.60	0.64	0.24	0.07	95	175	64	Table D.19
W51-IRS2	0.50	0.12	0.03	109	136	94	Table D.22
Total <sup>(5)</sup>				677	1020	539	

**Notes.** (1) Angular resolution after smoothing Band 3 and 6 images to a matched spatial resolution of 2700 au. (2) Standard deviation of the noise level in Band 6. (3) Equivalent mass to the standard deviation in Band 6, using Eq. 4, assuming  $S_{1.3\text{mm}}^{\text{peak}} / (\Omega^{1.3\text{mm}} \times B(20\text{K}, \nu)) \rightarrow 1$ . (4) Number of sources in common between the *getsf* and *GExt2D* extractions. (5) The total number of sources differs from the direct sum per field because two pairs of fields host sources in common. In the *getsf* extractions, sources number 3, 20, 30, and 31 in W51-E correspond to sources 3, 22, 38, and 108 in W51-IRS2, respectively; sources number 10 and 46 in W43-MM2 correspond to sources 2 and 37 in W43-MM3, respectively. In the *GExt2D* extractions, sources number 29, 32, and 46 in W51-E correspond to sources 21, 11, and 28 in W51-IRS2, respectively; source number 14 in W43-MM2 corresponds to source number 4 in W43-MM3.

structed the source flux functions (SFFs) and complementary cumulative SFFs for both algorithms (Fig. 3). The first function shows that the source fluxes range between 10 mJy and 10 Jy for both algorithms, with a similar median value at  $\approx 12$  mJy. It also shows that the additional sources found by *GExt2D* are low and intermediate flux sources from  $\sim 30$  mJy to 200 mJy. The complementary SFF permits to estimate the slope of the high-flux end of the SFF. We fit the cumulative SFF with a power law from the median value of the samples, that is 12 mJy, up to the flux at which the number of cores is below ten<sup>4</sup>. The fitted high-flux slopes are similar for both catalogues, with  $\zeta' \approx 0.85$ . These exponents, adjusted onto the complementary cumulative SFFs, correspond to power-laws with exponents  $\zeta = \zeta' + 1 \approx 1.85$ . This analysis proves that the overall statistics of source flux is independent of the two extraction algorithms we employed. In the following, we choose to focus on the extractions performed by *getsf* since it is more conservative than *GExt2D*, which is confirmed by the large fraction of *getsf* sources confirmed with *GExt2D*. Comparing the sources extracted at the native angular resolutions (see Sect. 3.2) to the sources extracted in the smoothed maps (see Sect. 3.3), there is better agreement between the *getsf* catalogues than between *GExt2D* catalogues. Indeed,  $\approx 95\%$  of the sources extracted in the smoothed maps were also extracted at the native angular resolutions with the *getsf* algorithm. This fraction drops to  $\approx 75\%$  in the case of the *GExt2D* extractions.

<sup>4</sup> We illustrate the cumulative complementary SFFs with constant logarithm flux interval. This method introduces a constant weight for each bin, whatever the number of sources constituting the bin. Therefore it artificially creates a bias for relatively unpopulated bins. For this reason, we ignored the last 10 sources from the fit.

## 4.2. From source flux to core mass

### 4.2.1. Removing contaminated sources

The integrated fluxes comprise thermal dust emission and potentially free-free emission for the more evolved sources. In the following, we filter the sources that are arguably contaminated by free-free emission. To do so, we used the integrated flux measurements at 1.3 and 3 mm, when available, to compute their spectral index. To correct from the source size differences between 1.3 and 3 mm extractions, we adjusted the integrated fluxes at 3 mm linearly:  $S_{3\text{mm}}^{\text{int}*} = S_{3\text{mm}}^{\text{int}} \times \left( \frac{\Theta_A^{1.3\text{mm}} \times \Theta_B^{1.3\text{mm}}}{\Theta_A^{3\text{mm}} \times \Theta_B^{3\text{mm}}} \right)$ , where  $\Theta_A$  and  $\Theta_B$  are the major and minor axes of the sources, respectively, at 1.3 or 3 mm. This operation corrects the 3 mm fluxes by 17% in average. This flux rescaling replicates the method we used in Paper III. This rescaling works both for an optically thick emission and for an optically thin emission of an isothermal protostellar envelope with a density profile  $\rho(r) \propto r^{-2}$ , where  $r$  is the radius of the envelope. We then compute the spectral index as:

$$\gamma = \frac{\log(S_{1.3\text{mm}}^{\text{int}}/S_{3\text{mm}}^{\text{int}*})}{\log(\nu_{1.3\text{mm}}/\nu_{3\text{mm}})} \quad (2)$$

where  $\nu_{1.3\text{mm}}$  and  $\nu_{3\text{mm}}$  are the central frequencies of the ALMA Band 6 and Band 3 respectively (see Table 1). We remove 68 sources with  $\gamma < 2$ , which are presumably contaminated by free-free emission. These sources are represented by the pink ellipses in Fig. 4.

To investigate the  $\approx 500$  sources that lack measurements at 3 mm, we built the spectral index map for each field, using Eq. 2 on a pixel-by-pixel basis by replacing  $S_{1.3\text{mm}}^{\text{int}}$  and  $S_{3\text{mm}}^{\text{int}}$  with the pixel intensities. We point out that the angular resolutions and pixel sizes of the images at 1.3 mm equal that of the images at

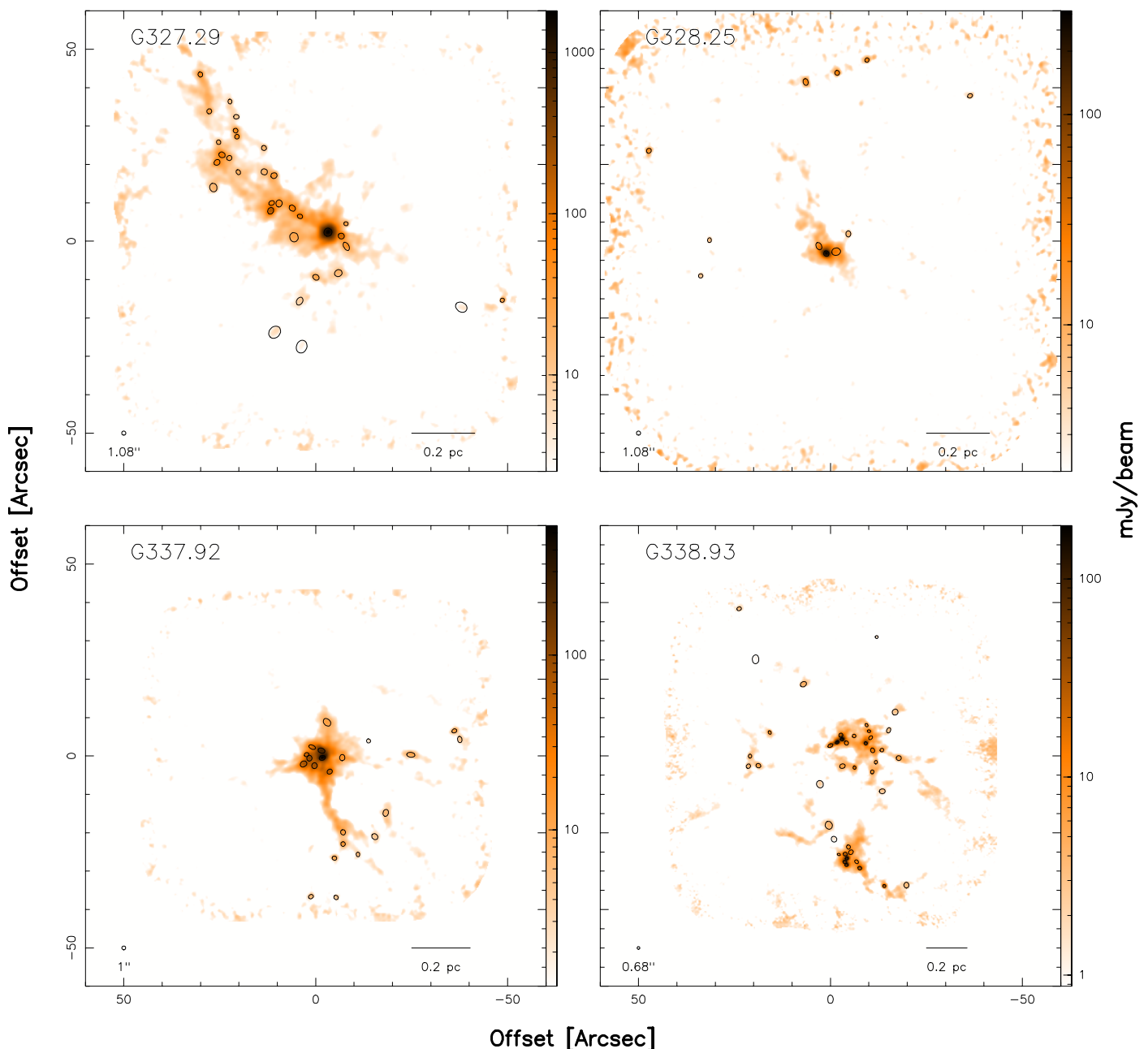


Fig. 2: The 15 ALMA-IMF protoclusters as traced by their continuum emission at 1.3 mm at a matched spatial resolution of 2700 au. The ellipses locate all the cores found by *getsf*. The name of the field is indicated in the top left corner of each panel and the beam size is shown in the bottom left corner. For each protocluster, the center coordinates are those specified in Table 1.

3 mm. We show the spectral index maps in Fig. 4. The red areas ( $\gamma > 2$ ) represent pixels with thermal dust emission, those in green ( $0 < \gamma < 2$ ) pixels contaminated by free-free emission, and those in blue ( $\gamma < 0$ ) pixels dominated by free-free emission. We manually selected all the sources lying over free-free emission areas ( $\gamma < 2$ , see yellow ellipses in Fig. 4). For the sources undetected at 3 mm we estimate their flux,  $S_{3\text{mm}}^{\text{upper}}$ , using the integrated flux in the aperture corresponding to the footprint of the source detected at 1.3 mm. We emphasise that although *getsf* did not detect these 1.3 mm sources as compact sources at 3 mm they do have a background emission above  $3\sigma$  at 3 mm, by definition of the spectral index maps. We use this upper limit to

compute an upper limit on their spectral index as:

$$\gamma = \frac{\log(S_{1.3\text{mm}}^{\text{int}}/S_{3\text{mm}}^{\text{upper}})}{\log(\nu_{1.3\text{mm}}/\nu_{3\text{mm}})} \quad (3)$$

and we rejected the 16 sources with spectral index below 1, those for which free-free emissions could substantially contribute to the emission.

These filtering rejected 84 of the 677 sources extracted by *getsf*. The degree of rejection depends on the evolutionary stages of the regions:  $\approx 0.5\%$  in the young regions,  $\approx 10\%$  in the intermediate regions, and  $\approx 25\%$  in the evolved regions. Table 3 lists, for each field, the number of sources rejected when applying these two levels of filtering.

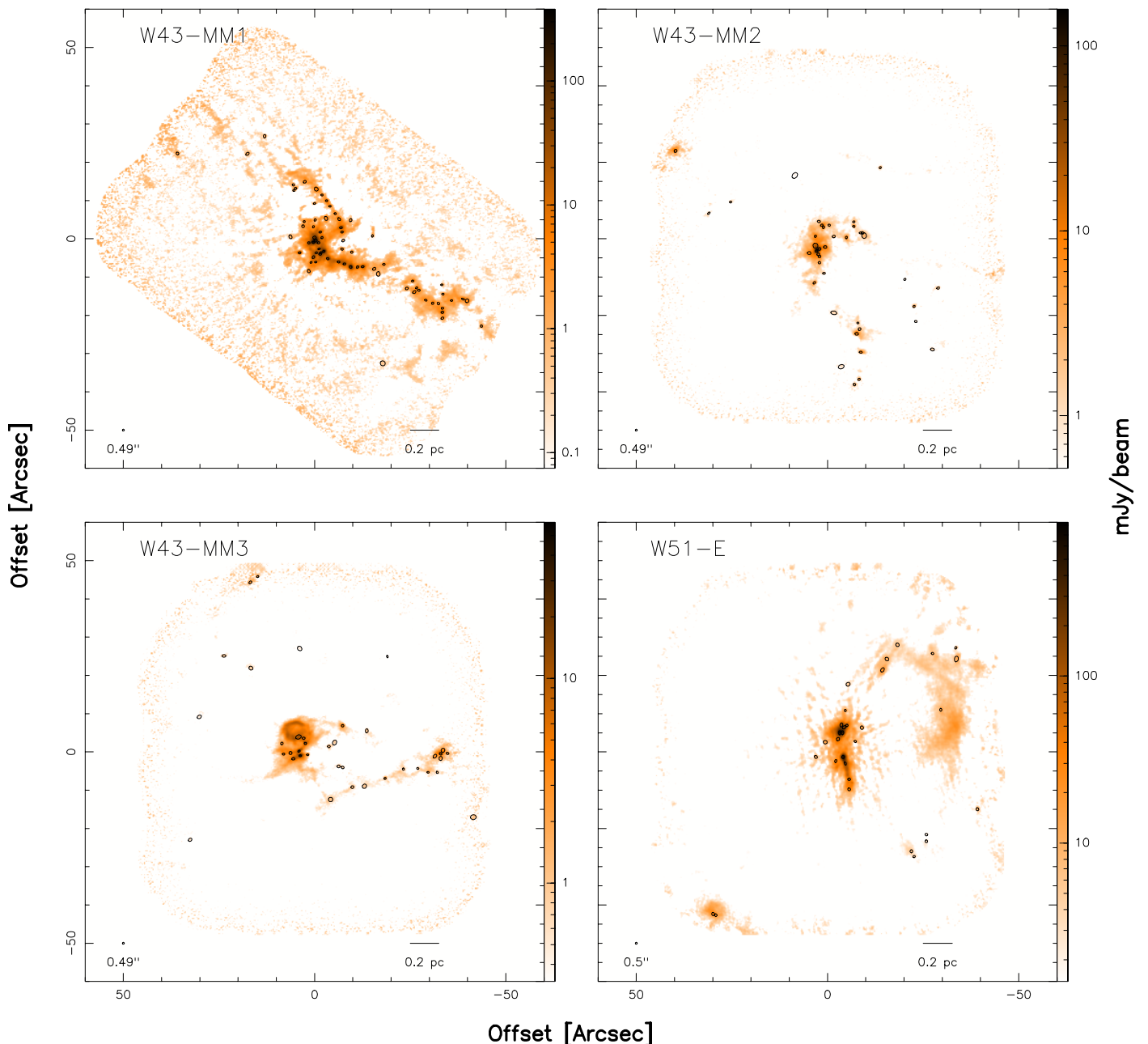


Fig. 2: Continuum emission maps (continued).

#### 4.2.2. Core temperatures

Following the pilot study by [Motte et al. \(2018\)](#), we used the Bayesian procedure *PPMAP* ([Marsh et al. 2015](#); [Dell’Ova et al. 2024](#)) to build the temperature maps of the ALMA-IMF protoclusters. The procedure uses several continuum emission maps to compute a cube of column densities as a function of dust temperature. Our *PPMAP* algorithm takes, along with the ALMA data in Band 6 decontaminated from free-free emission ([Galván-Madrid et al. subm.](#)), the following maps as input:

- SOFIA/HAWC+ data at  $214 \mu\text{m}$  with an angular resolution of  $19.0''$  (only for G012.80, G351.77, W51-E and W51-IRS2, [Vaillancourt 2016](#); [Pillai & Simplifi Team 2023](#)).
- Herschel/PACS and Herschel/SPIRE data at 70, 160, 250, 350,  $500 \mu\text{m}$  with angular resolutions of 5.6, 10.7, 17.6, 23.9 and  $35.2''$ , respectively ([Molinari et al. 2010](#); [Motte et al. 2010](#)).

- APEX/SABOCA data at  $350 \mu\text{m}$  with an angular resolution of  $7.8''$  ([Lin et al. 2019](#)).
- APEX/LABOCA data at  $870 \mu\text{m}$  with an angular resolution of  $19.2''$  ([Schuller et al. 2009](#)).

We refer to [Dell’Ova et al. \(2024\)](#) for an in-depth description of the method. Finally, we obtain a unique temperature for each core at an angular resolution of  $2.5''$ . The derived temperatures vary from 19.4 to 62.8 K (see Tables [D.14](#) to [D.22](#)). The error associated with *PPMAP* derivation is  $\approx 5$  K; to account for potential systematic contributions, we adopt a 25% error on the *PPMAP* temperature estimates<sup>5</sup>.

We adopted the *PPMAP* temperatures for all cores except for the hot core candidates for which we adopted the method proposed in [Bonfand et al. \(2024\)](#): we cross-correlated the position of continuum sources (see Sect. 3.3) with methyl formate

<sup>5</sup> We adopt an uncertainty of 5 K for sources below 20 K.

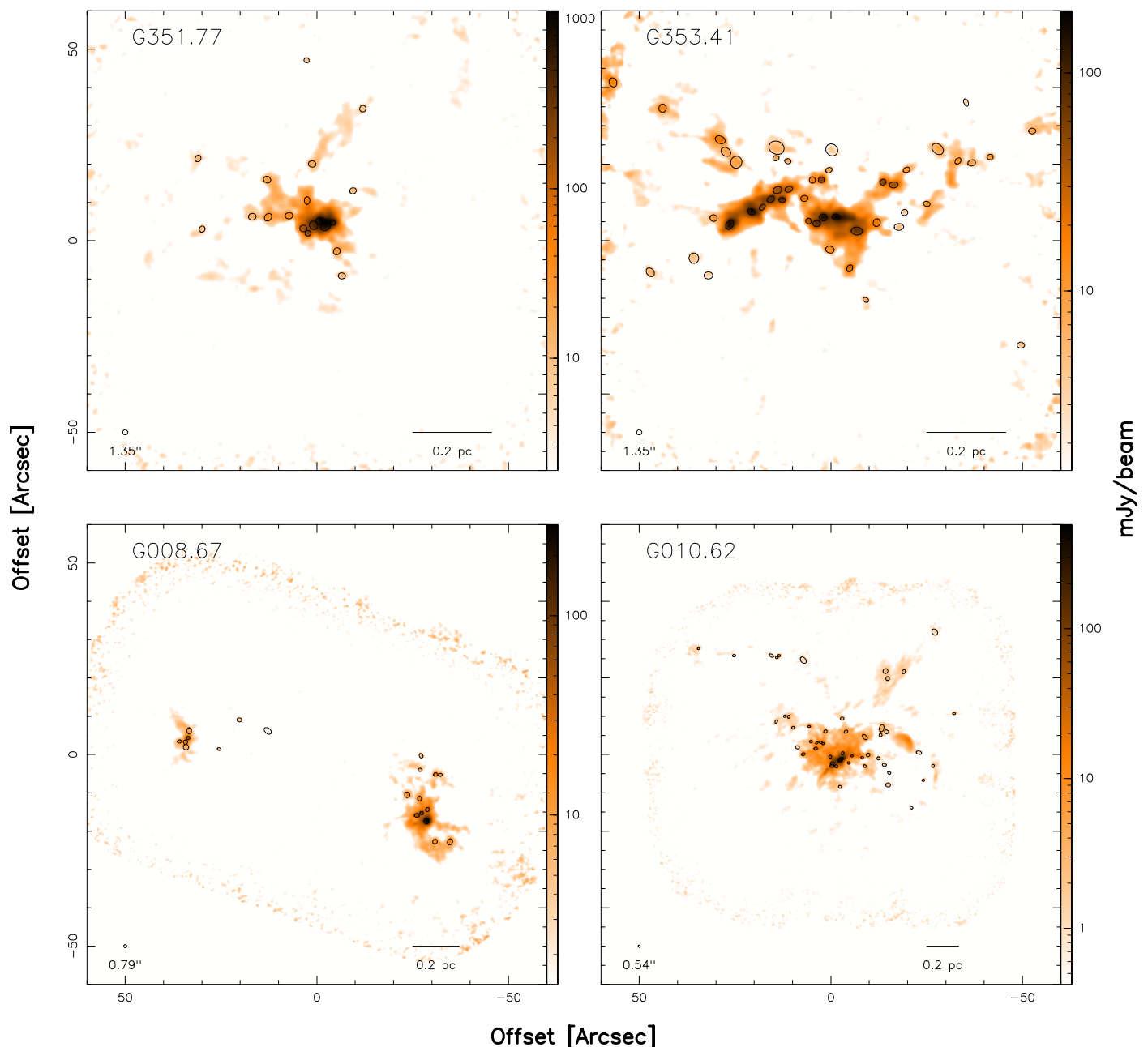


Fig. 2: Continuum emission maps (continued).

(CH<sub>3</sub>OCHO) emission maps that were observed by ALMA-IMF. Methyl formate forms at the surface of dust grains in lukewarm (30-40 K) regions, and is then released in the gas phase when the temperature reaches  $\sim 100$  K (e.g. Garrod et al. 2009). Methyl formate can be used as a proxy to trace regions where heating is present and dust surface products have started to sublimate. Following the method discussed in Bonfand et al. (2024), we set  $100 \pm 50$  K to the 49 sources whose position corresponds to the peaks of extended methyl formate emission; these sources are classified as hot core candidates.

Additionally, we set  $300 \pm 100$  K to sources n°1, n°2, and n°1 in W51-IRS2, W51-E and G327.29 respectively, following their detailed modelling by Ginsburg et al. (2017), Goddi et al. (2020), and the adopted temperature in Bonfand et al. (2024), respectively. These three sources are associated with strong and

extended emission structures in the methyl formate emission maps.<sup>6</sup>

#### 4.2.3. Core mass and boundedness

We converted the measured integrated flux at 1.3 mm,  $S_{1.3 \text{ mm}}^{\text{int}}$ , into a mass using the formula presented in Paper III that includes a first order correction for the optical thickness:

$$M_{\text{core}} = -\Omega_{\text{beam}}^{1.3 \text{ mm}} \frac{D^2}{\kappa_{1.3 \text{ mm}}} \frac{S_{1.3 \text{ mm}}^{\text{int}}}{S_{1.3 \text{ mm}}^{\text{peak}}} \ln \left( 1 - \frac{S_{1.3 \text{ mm}}^{\text{peak}}}{\Omega_{\text{beam}}^{1.3 \text{ mm}} B(T, \nu)} \right) \quad (4)$$

<sup>6</sup> Bonfand et al. (2024) report 6 sources with temperatures estimated at  $300 \pm 100$  K. The 3 additional sources with respect to ours are either classified as freefree contaminated (source W51-E-MF1) or not matching our continuum extractions (sources W51-E-MF2 and W51-IRS2-MF3).

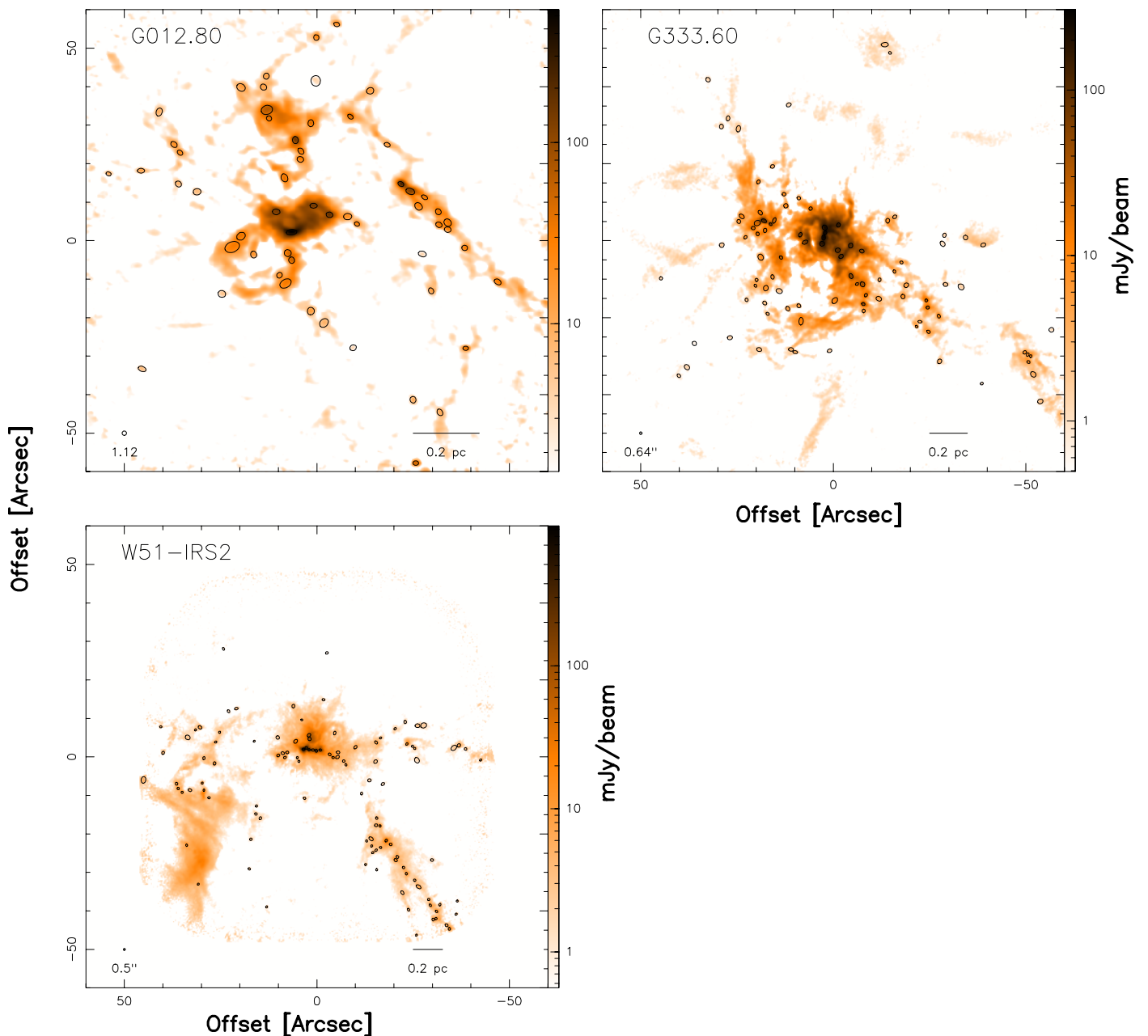


Fig. 2: Continuum emission maps (continued).

where  $D$  is the distance to the target,  $\kappa_{1.3\text{mm}} = 0.1(\nu/1000\text{GHz})^\beta \text{cm}^2 \text{g}^{-1}$  is the dust opacity per unit mass (dust + gas), with an opacity index  $\beta = 1.5$  typical of cold and dense environment (Ossenkopf & Henning 1994), and  $B(T, \nu)$  is the Planck function computed at the representative frequency of the observations in Band 6 with the dust temperature  $T$  (see Table 1 for central frequencies and distances, and Tables D.14 to D.22 for source temperature).

Errors on the masses mostly arise from the uncertainties on the opacity index  $\beta$  and on the dust temperature,  $T$ . Masses would be a factor of two smaller using  $\beta = 2$  instead of  $\beta = 1.5$ . As for the temperature, a 25% difference leads to a mass shift by  $\lesssim 40\%$ .

To address the boundedness of cores, we computed the ratio  $M_{\text{BE}}/M_{\text{core}}$  where  $M_{\text{core}}$  is the core mass and  $M_{\text{BE}}$  is the mass of the critical Bonnor-Ebert sphere (Bonnor 1956) whose size matches that of the core:  $M_{\text{BE}} = 2.4 \times R \times \sigma_{\text{th}}^2/G$ . Here,  $R$  is

the equivalent core radius, estimated as  $R = (a \times b^2)^{1/3} \times D^7$ , where  $a$  and  $b$  are the major and minor axis of the source ellipse, respectively. Moreover,  $\sigma_{\text{th}}$  is the thermal broadening of lines, as  $\sigma_{\text{th}} = \sqrt{\gamma k_B T / (\mu \times m_p)}$  where  $\gamma = 1$  is the adiabatic index (isothermal),  $k_B$  is the Boltzmann constant,  $\mu = 2.4$  is the mean molecular weight per free particle, and  $m_p$  is the mass of a proton. We consider that the sources are gravitationally bound if  $M_{\text{BE}}/M_{\text{source}} < 2$  (see e.g. Louvet et al. 2021). As listed in Table 3, this filter excludes no sources. We note that this is a first-order check of the boundedness of cores. A more accurate determination would require computing the equilibrium of each source taking into account its turbulence, external pressure, and magnetic field support in addition to the thermal support. Unfortunately, we lack all these pieces of information at the moment.

<sup>7</sup> We stress that choosing 3D oblate core shape ( $V \propto a^2 \times b$ ) has no effect on the boundedness of the cores.



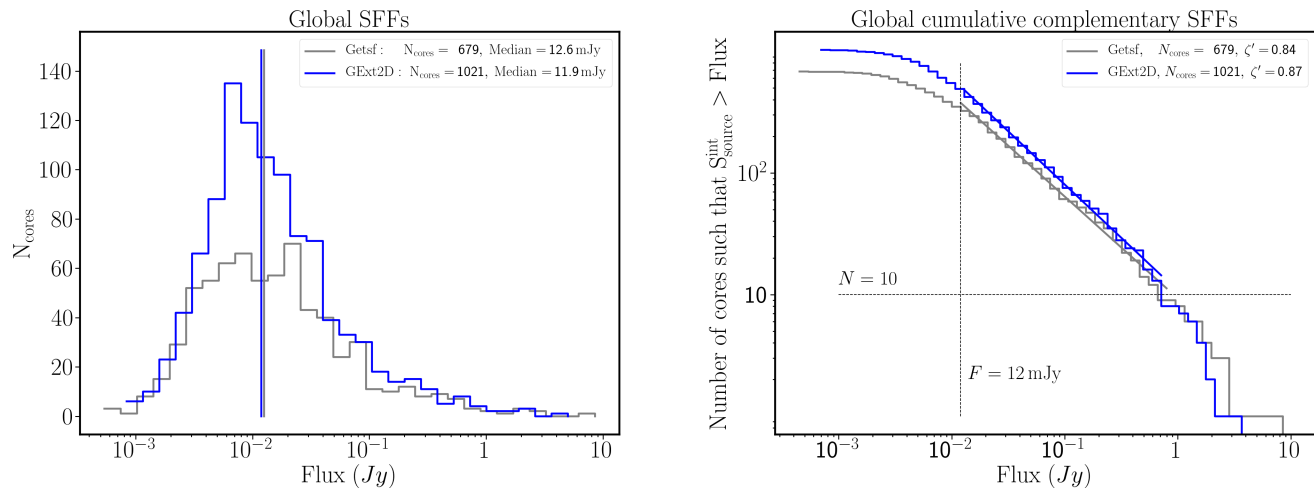


Fig. 3: The left panel displays the source flux functions (SFFs) of the sources extracted by *getsf*, in grey, and by *GExt2D* in blue. The vertical blue and grey lines indicate the median values for each source catalogues, which differ by  $\approx 5\%$ . The right panel displays the complementary cumulative SFFs from the *getsf* source extraction (in grey) and from the *GExt2D* source extraction (in blue). The grey and blue lines display the best fits from linear regressions on the complementary cumulative SFFs from the median value at 12 mJy up to the flux at which the number of cores is less than 10. The corresponding  $\zeta$  power-law indexes are indicated in the top right corner.

Table 3: Evolution of the core sample through the selection process

Protocluster	All <sup>(1)</sup>	$\gamma < 2$ <sup>(2)</sup>	$S_{3\text{mm}}^{\text{theo}} < \sigma_{3\text{mm}}^{\text{(3)}}$	Unbound <sup>(4)</sup>	Bound <sup>(5)</sup>	$M_{\text{low}}^{\text{(6)}}$ [ $M_{\odot}$ ]	$M > M_{\text{low}}^{\text{(7)}}$	$M > 1.64 M_{\odot}^{\text{(8)}}$
G327.29	32	0	0	0	32	1.53	26	25
G328.25	11	0	0	0	11	1.53	7	7
G337.92	22	0	0	0	22	1.13	14	11
G338.93	42	0	0	0	42	1.41	31	29
W43-MM1	71	1	0	0	70	1.54	53	49
W43-MM2	40	0	0	0	40	1.60	24	24
W43-MM3	36	1	0	0	37	1.33	16	12
W51-E	31	7	1	0	23	3.86	20	20
G351.77	19	1	0	0	18	0.80	11	6
G353.41	46	1	0	0	45	1.18	23	17
G008.67	20	1	0	0	19	1.53	15	14
G010.62	50	8	0	0	42	0.96	29	22
G012.80	57	9	4	0	44	1.30	30	25
G333.60	95	34	7	0	54	1.28	30	23
W51-IRS2	109	6	4	0	99	1.64	67	66
Total <sup>(9)</sup>	677	68	16	0	593		393	350 <sup>(10)</sup>

**Notes.** (1) Number of sources extracted by *getsf*. (2) Number of sources contaminated by freefree. (3) Number of sources whose emission could be contaminated by freefree. (4) Number of sources not gravitationally bound. (5) Number of sources gravitationally bound. (6) Mass completeness limit in the field. (7) Number of gravitationally bound cores exceeding the field's completeness level (see Sect. 5.1). (8) Number of gravitationally bound cores exceeding the global completeness level (see Sect. 5.1). (9) The total number of sources differs from the direct sum per field because two pairs of fields host sources in common (see Table 2). (10) The total number of sources reduces to 330 when discarding W51-E.

In Figs. 2 we show the thermal-dust cores for each field. The Tables D.1 to D.24 list all the sources detected by the *getsf* extraction algorithm in each field. The first group of sources in each table corresponds to thermal dust cores that are gravitationally bound, and the second group corresponds to sources whose fluxes are arguably contaminated by free-free emission. For each

source, the last column indicates whether it was also detected by *GExt2D*, which is true for 80% of the extracted sources.

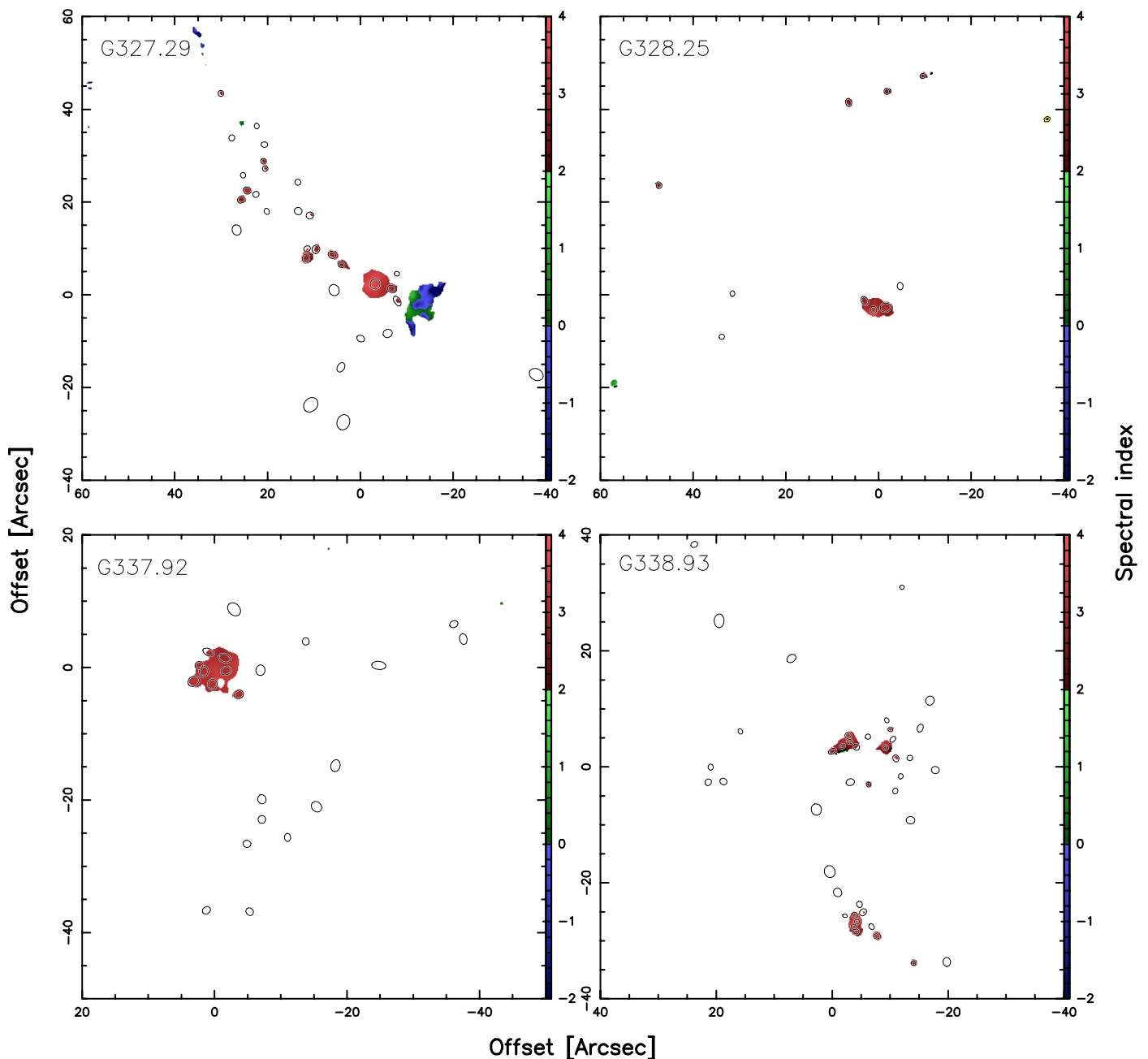


Fig. 4: The maps display the spectral index in the fifteen ALMA-IMF fields. We chose the colours such that red traces dust thermal emission, blue traces free-free emission and green likely traces a mixture of dust and free-free emissions. The maps display the spectral index value only where the 3 mm intensity exceeds  $3\sigma$ . The black ellipses display the sources extracted by *getsf*.

## 5. Core mass function

### 5.1. Completeness tests

In order to draw a coherent sample gathering cores from the 15 ALMA-IMF protoclusters, we need to ascertain that the core extractions are complete at the selected lower mass limit. To do so, we performed completeness tests in each protocluster: we injected synthetic cores on top of their background emission (i.e. the emission subtracted from each source). The synthetic cores are injected in the form of 2D circular Gaussian with a FWHM corresponding to 3840 au — the mean core size (see Sect. 3.3). We inject these synthetic sources randomly, provided the centre of the cores are separated by more than  $2.5''$ . We forbid the injection of sources within  $5''$  of the border of the maps, where the

noise increases due to the primary beam correction (see Fig. 2). The flux of the synthetic sources ranges from equivalent masses of  $0.5$  to  $5 M_{\odot}$  in all fields for gas at 20 K, except in W51-E where we adopted a mass range of 1 to  $10 M_{\odot}$ . The fluxes are equally split into ten bins of flux. From these fluxes, we compute the mass of the synthetic cores when adopting the mean temperature of the cores extracted in the corresponding region. We then extract the synthetic cores with the *getsf* method (see Sect. 3.1). To obtain a good statistics in each bin of mass, we repeated this procedure four times per field. Cumulating the four draws we obtain  $\approx 3800$  cores in total in each field (or  $\approx 380$  per bin) and we probe  $\approx 80\%$  of the background area. We plot the percentage of synthetic cores extracted as a function of their mass in Fig. A.1. Following Paper III, we consider reaching the com-

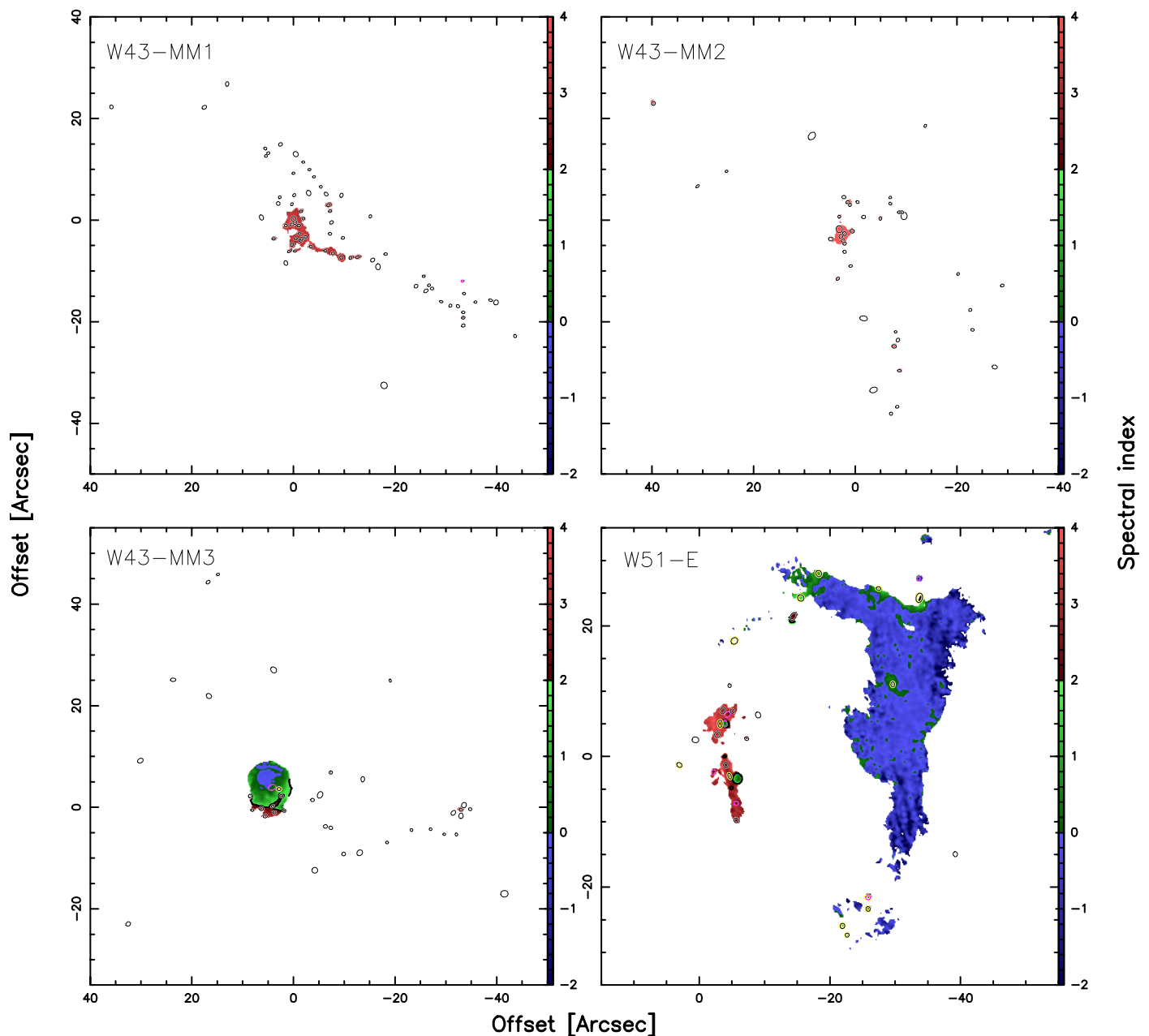


Fig. 4: Spectral index maps (continued). The ellipses in pink highlight sources automatically flagged due to their spectral index; those in yellow display the sources whose spectral index were further checked manually (see Eq. 2).

pleteness limit when 90 % of the synthetic cores are extracted. The mass completeness varies from  $0.80$  to  $1.64 M_{\odot}$  with a mean value of  $1.34 M_{\odot}$  and a standard deviation of  $0.2 M_{\odot}$ . These numbers exclude W51-E, for which we find completeness as high as  $3.9 M_{\odot}$ . We exclude W51-E from the analysis of the global CMF (see Sect. 6.1) and we restrict the core samples to cores exceeding  $1.64 M_{\odot}$  to fit the high-mass tail of the CMF.

## 5.2. Fitting core mass functions

### 5.2.1. Method

The representation of a distribution in the form of histograms, as in Fig. 3, further fitted through linear regression may give inaccurate results (Clauset et al. 2009). In addition, the representation in the form of a CMF in log-log scales prohibits esti-

imating the fit uncertainty since the noise is not Gaussian. Moreover, the choice of the bin width induces a free parameter that thwarts any uncertainty estimate. The representation in the form of a cumulative CMF, however, prevents the estimation of the uncertainty as the data are not independent. To circumvent these issues, we choose to fit the high-mass end of the CMF using maximum likelihood estimates (MLE). We follow the procedure presented by Clauset et al. (2009), and use its implementation in the python package `powerlaw` presented by Alstott et al. (2014). If we assume that the CMF can be represented by a power-law  $p(x) = Cx^{-\alpha}$ , where  $C$  is a constant, there must be some lower mass value,  $x_{\min}$ , from which the power-law fit is accurate, and prevents the divergence of  $p$  when  $x \rightarrow 0$ . After normalisation

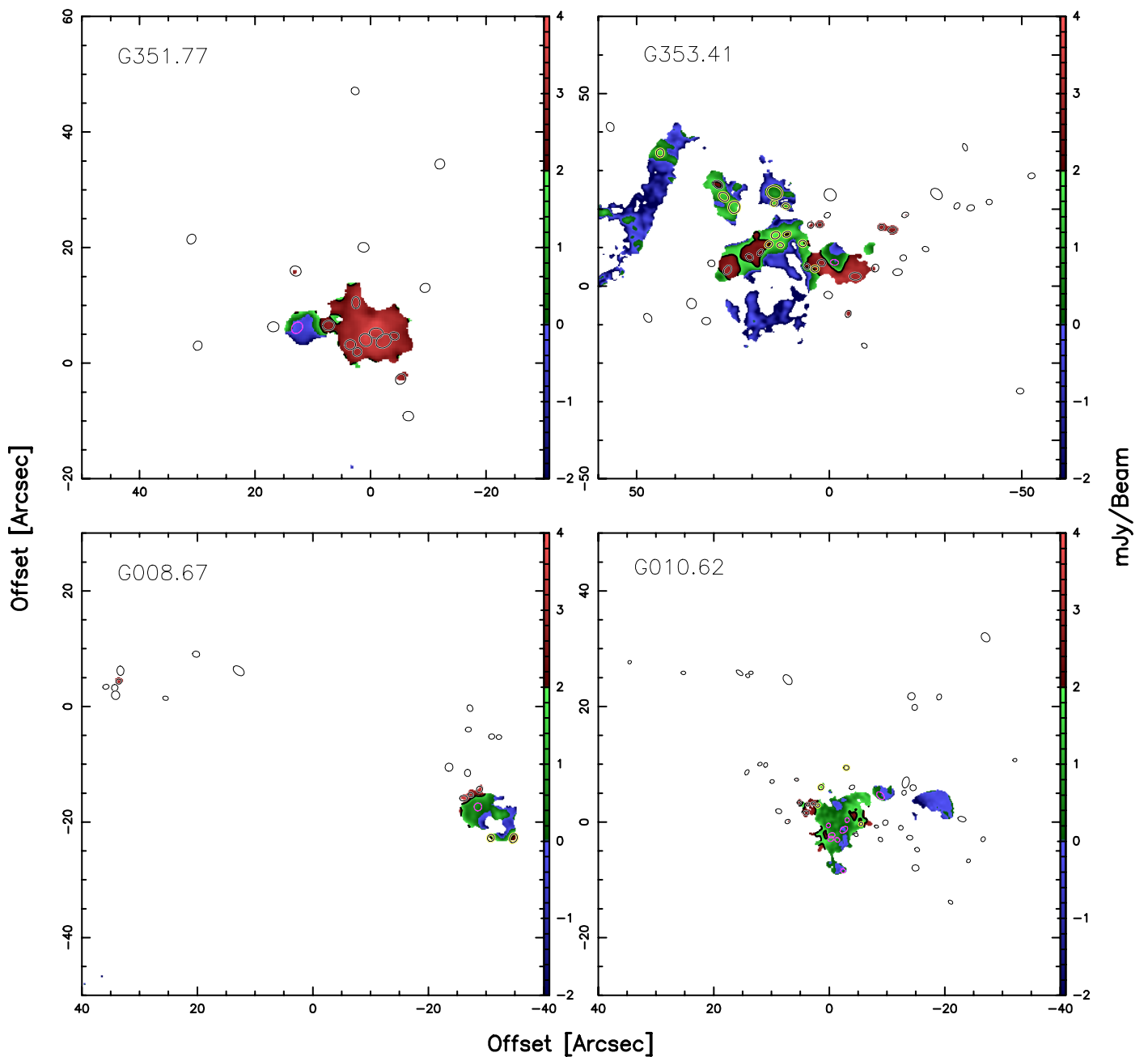


Fig. 4: Spectral index maps (continued).

(imposing that  $\int_{x_{\min}}^{+\infty} p(x) dx = 1$ ) it comes:

$$p(x) = \frac{\alpha - 1}{x_{\min}} \left( \frac{x}{x_{\min}} \right)^{-\alpha} \quad (5)$$

When  $x_{\min}$  is known, the MLE gives an estimate of the exponent of the power-law as:

$$\alpha = 1 + n \left[ \sum_{i=1}^n \ln \frac{x_i}{x_{\min}} \right]^{-1} \quad (6)$$

where  $x_i$  is the mass of the core  $i$  (provided  $x_i \geq x_{\min}$ ), and the uncertainty on  $\alpha$  reads:

$$\sigma = \frac{\alpha - 1}{\sqrt{n}} + O\left(\frac{1}{n}\right) \quad (7)$$

where  $O$  is the mathematical notation for: not negligible in front of.

The originality of the method by [Clauset et al. \(2009\)](#) is to propose a method to determine the best parameters  $x_{\min}$  and  $\alpha$  using the Kolmogorov-Smirnov (KS) distance. First, the method computes  $\alpha$  for  $x_{\min}$  taking successively each mass value of the core sample. Then it computes the maximal distance — the KS distance,  $KS_D$  — between the observational CMF for all elements whose mass exceeds  $x_{\min}$  and the synthetic CMF following a probability distribution function as defined by Eq. 5. The best value for the parameters  $x_{\min}$  and  $\alpha$  is that which minimizes the  $KS_D$ . Figure 5 shows the evolution of  $\alpha$  and  $KS_D$  for all  $x_{\min}$  values. In our case, we need to select the highest value between the  $x_{\min}$  that minimizes the  $KS_D$  and our completeness limit (see Sect. 5.1). The first minimum in the  $KS_D$  is met for  $x_{\min} = 1.40 M_{\odot}$ , below our completeness level at  $1.64 M_{\odot}$ .

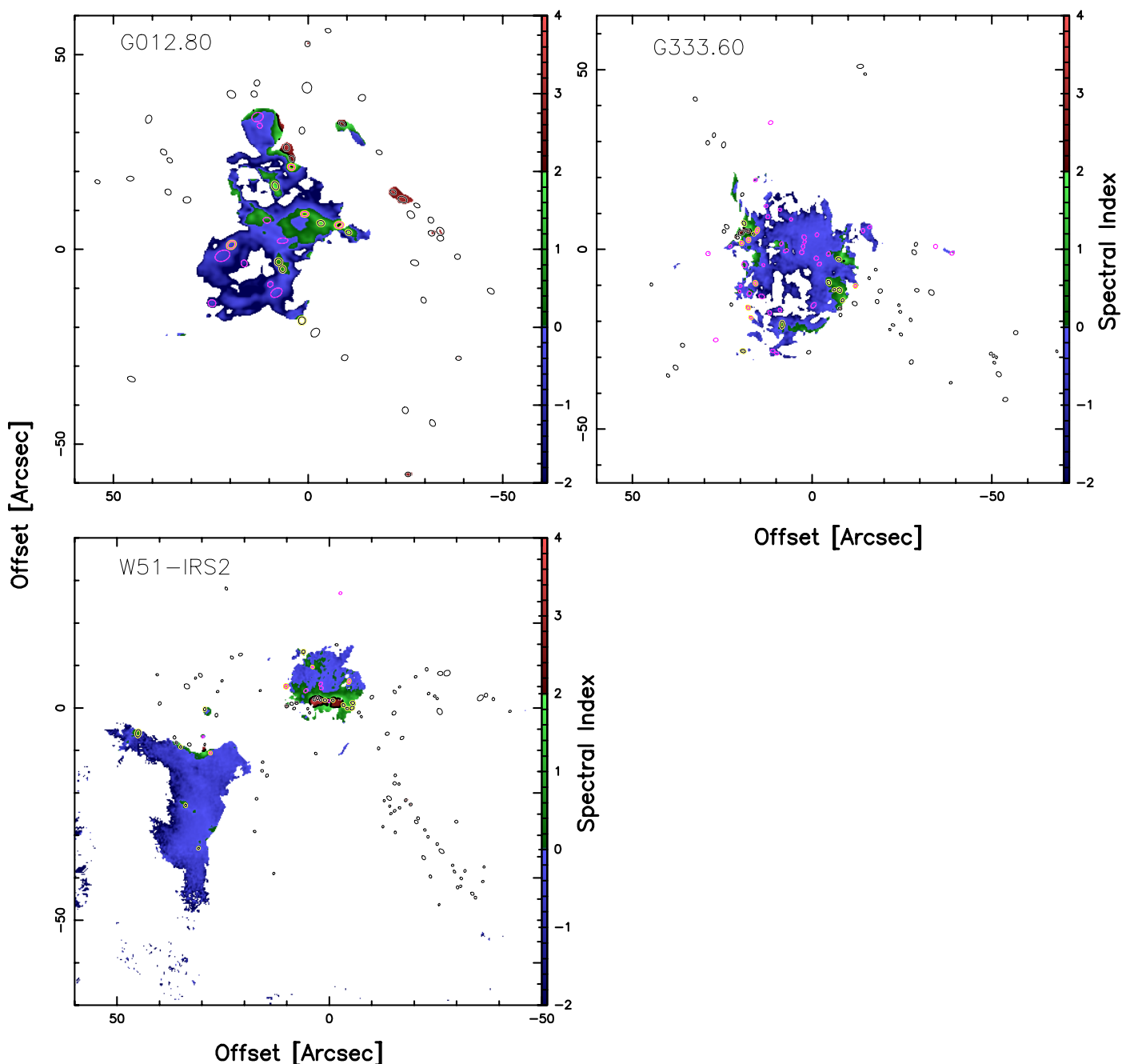


Fig. 4: Spectral index maps (continued).

We, therefore, select  $x_{\min} = 1.64 M_{\odot}$ , which corresponds to a core sample of 330 elements (excluding W51-E). From that subsample, we obtain a power-law index fit  $\alpha = 2.11 \pm 0.06$ <sup>8</sup>. We put forward that 330 cores above the completeness limit convey a statistically conclusive sample. [Clauset et al. \(2009\)](#) report stable index values when the sample exceeds  $\approx 50$  elements above the completeness limits. Consistently, [Louvet et al. \(2021\)](#) report stable index values when the sample exceeds  $\approx 40$  elements above the completeness limits.

<sup>8</sup> We note that  $x_{\min} = 1.40 M_{\odot}$  corresponds to  $\alpha = 2.07 \pm 0.06$ , compatible with the  $\alpha$  associated with  $x_{\min} = 1.64 M_{\odot}$ .

### 5.2.2. Uncertainty of the fit

As pointed out in Sect. 4.2.3, errors in the mass estimates arise primarily from the uncertainties on the opacity index and core temperature. To study how these uncertainties affect the slope of the CMF, we performed a Monte Carlo simulation on our 330 cores by allowing their opacity index, their temperature as well as their source flux to vary simultaneously. About the latter, we used the Gaussian error associated with the flux measurement. [Koen & Kondlo \(2009\)](#) showed that including such errors on the fluxes flattens the distribution. However, since our relative uncertainty diminishes for brighter sources, we expect this effect to be marginal on the high-mass end of our CMF. In our Monte Carlo simulation, the opacity index  $\beta$  can take random normal values with a mean value of 1.5 ([Ossenkopf & Henning 1994](#))

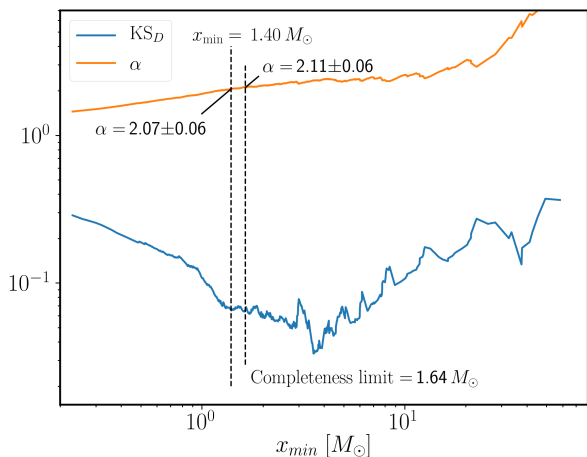


Fig. 5: Convergence towards the best fit of a power-law through MLE and  $KS_D$  method for the global *getsf* bound core catalogue without the free-free sources. The left vertical dashed line highlights the first minimal  $KS_D$  (in blue), occurring at  $x_{\min} = 1.40 M_{\odot}$ . The right vertical dashed line highlights the completeness limits at  $x_{\min} = 1.64 M_{\odot}$ . The orange curve shows the exponent of the power law fit of the high-mass tail of the CMF as a function of  $x_{\min}$ .

and a standard deviation of 0.2 for each core. In parallel, we allow the core temperature to take random normal values with the mean and standard deviation as described in Sect. 4.2.2. We show the resulting cumulative CMFs generated from  $10^3$  trials in Fig. 6. Each draw is fitted via MLE (see Sect. 5.2.1), fixing  $x_{\min}$  to  $1.64 M_{\odot}$ . We obtain a mean exponent value for the slope of the CMF of  $1.97 \pm 0.06$ , where the uncertainty is the quadratic sum of the statistical uncertainty from Eq. 7 ( $\sigma \approx 0.06$ ) and from the uncertainties on the temperature, opacity index, and flux measurement uncertainties ( $\sigma \approx 0.02$ ). We show in Appendix E.1 the results of the  $10^3$  trials for a power-law fit.

### 5.2.3. Comparison with the Salpeter-slope

The ALMA-IMF large program aims to test if the high-mass slope of the CMF differs from the high-mass slope of the canonical IMF ( $\alpha = 2.35$  when fitted by a power-law, Salpeter 1955). To see if our sample of 330 cores (with  $M > x_{\min} = 1.64 M_{\odot}$ ) permits such a claim, we selected 330 sources from a perfect mass distribution with an exponent of 2.35 and fitted the slope of its high-mass tail through the MLE. We repeated the operation  $10^5$  times. Figure 7 shows the probability of retrieving an exponent  $\alpha$  when the parental distribution has a slope  $\alpha=2.35$ . With 330 cores, the probability of retrieving a slope compatible with ALMA-IMF,  $\alpha = 1.97 \pm 0.06$ , is lower than 1% ( $\sigma \approx 2.4$ ). Therefore, we report that the CMF in the protoclusters studied by ALMA-IMF is flatter than, and cannot reasonably be reconciled with the Salpeter-IMF slope to a  $2.4\sigma$  level<sup>9</sup>.

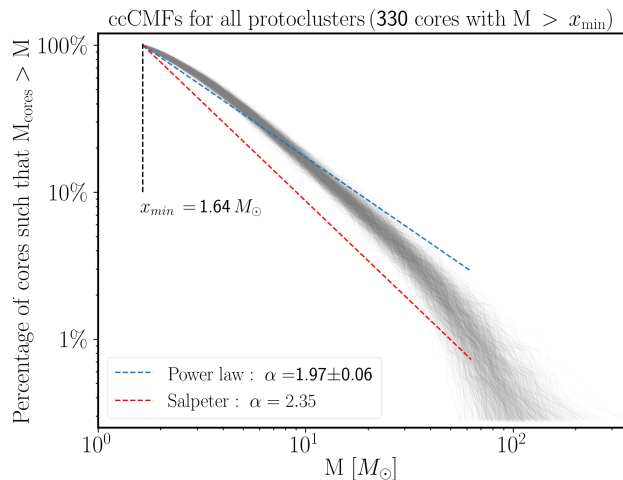


Fig. 6: The grey curves show the complementary cumulative CMFs (ccCMFs) of the  $10^3$  core samples obtained by including flux measurement uncertainties, varying core temperatures, and applying opacity index variations on a per-regions basis (see Sect. 5.2.2), overlaid with the average fit by a power-law (in blue) and the best fit with a power-law of index 2.35.

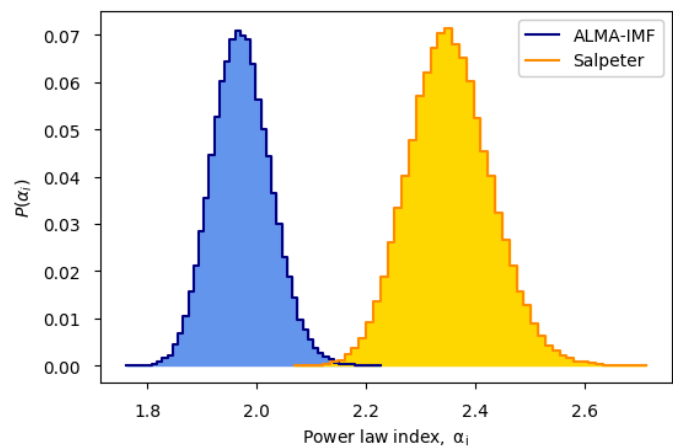


Fig. 7: The figure illustrates the power-law exponents  $\alpha$  retrieved when sorting 330 cores from a synthetic core sample whose CMF has a power-law exponent of 1.97 (in blue) and 2.35 (in orange).

## 6. Discussion

### 6.1. A global top-heavy core mass function

In Sects. 5.2.1 and 5.2.2, we presented the best fit to the high-mass tail of the CMF by a power law. The best-fit yields  $\alpha = 1.97 \pm 0.06$ . This result, based on 330 cores, confirms the many investigations led in recent years that reported top-heavy CMFs in high-mass protoclusters (e.g. Motte et al. 2018; Cheng et al. 2018; Sanhueza et al. 2019; Kong 2019; Moser et al. 2020). We show that this slope cannot be reconciled, at the  $2.4\sigma$  level, with the canonical IMF slope ( $\alpha = 2.35$ , see Sect. 5.2.3) even after the inclusion of all known uncertainties.

Observing top-heavy CMFs in high-mass protoclusters contrasts with nearby low-mass star-forming regions where a high-mass tail compatible with Salpeter is consistently found (see,

<sup>9</sup>  $\sigma$  refers to a confidence interval of a Gaussian distribution.

e.g., Table 6 of [Fiorellino et al. 2021](#) for all CMF exponents from the Herschel Gould Belt Survey).

## 6.2. From the CMF to the IMF

To link the CMF to the IMF, one must assume that cores constitute the mass reservoir for the accretion of protostars. One also assumes a fragmentation cascade and a mass transfer efficiency  $\epsilon$  from cores to protostars. Regarding the latter, the common assumption is that one core will give birth to one star — and therefore assumes no sub-fragmentation — and that  $\epsilon$  remains constant whatever the mass of the cores. If we adopt these assumptions, since our massive protoclusters display a top-heavy CMF they shall engender a top-heavy IMF with a high-mass slope equals to that of the CMF:  $\alpha \approx 1.97$ . Meanwhile, [Bon-temps et al. \(2010\)](#), [Louvet et al. \(2014\)](#) and [Csengeri et al. \(2017\)](#) showed that  $\epsilon$  actually depends almost linearly on the local density. As a matter of facts, the massive cores —  $>25 M_{\odot}$  — spread equally over the observed size range and are therefore, on average, denser than low- and intermediate-mass cores (see red crosses in Figure 1). This suggests that massive cores will convert gas into stars more efficiently than low- and intermediate-mass cores, giving birth to a flatter IMF than the parental CMF. In the past ten years some examples of top-heavy IMFs have been reported in young massive clusters in and out of our Galaxy (see for example [Lu et al. 2013](#); [Schneider et al. 2018](#)). As a consequence, we speculate that the ALMA-IMF protoclusters might be the precursors of star-clusters whose IMF is top-heavy. From another perspective, we now observe more regularly star-forming regions with at top-heavy CMF than star clusters with a top-heavy IMF. To reconcile these two observables, we hypothesise that some of the star-forming regions hosting a top-heavy CMF will evolve to produce a Salpeter-like IMF.

## 6.3. Limitations and perspectives

We recognize two limitations in our study:

- Free-free emission: in Sect. 4.2, we rejected all sources that are arguably contaminated by free-free emission from our core sample. We ended up rejecting 84 sources (see Table 3). Galván-Madrid et al. *subm.* gives estimates of the free-free contribution, based on the  $H_{41\alpha}$  recombination lines collected by ALMA-IMF. This characterization will allow us to correct and re-introduce these sources in the core sample. These sources, with free-free emission, arise from massive young stellar objects and would steepen our CMF even further. Therefore, our conclusions will stay unchanged by the inclusion of the free-free contaminated cores.
- Sub-fragmentation: we probed the cores at a spatial resolution of 2700 au. Recent observations in the high-mass protostellar core G335 showed that a binary system, and perhaps even a triple system, could take place below 1000 au ([Olguin et al. 2021, 2022](#)). Similar results were obtained by [Izquierdo et al. \(2018\)](#) in W33A. However, other works reported no fragmentation in G336.01-0.82 ([Olguin et al. 2023](#)) or HH80-81 ([Girart et al. 2018](#)). At present date, it is thus uncertain how will be the multiplicity in the ALMA-IMF fields. A straightforward path would consist in conducting observations at a yet higher angular resolution to reach a spatial resolution of  $\approx 200$  au, the typical scale of Solar-type proto-planetary disks (e.g. [Louvet et al. 2018](#)). The main difficulty consists in obtaining high sensitivities with an optically thin tracer at the scale of protoclusters.

## 7. Conclusions

We present the core catalogues of the 15 high-mass protoclusters observed by the ALMA-IMF large programme. At a homogeneous sensitivity and spatial resolution (2700 au), we collected about 680 sources. Rejecting sources arguably contaminated by free-free emission, we analysed a core sample of  $\approx 600$  elements. We performed completeness tests and found the matched-physical resolution core catalogues to be complete down to  $1.64 M_{\odot}$ , with the exception of the W51-E protocluster whose cores were discarded from the CMF analysis. In total, we analysed 330 cores with masses above the completeness limit of  $1.64 M_{\odot}$  and with little to no free-free contamination.

We fit the high-mass slope of the core mass function (CMF) with the maximum likelihood estimate technique and found a best-fit power law probability distribution function (PDF)  $\frac{dN}{dM} \propto M^{-\alpha}$  with  $\alpha = 1.97 \pm 0.06$ . Such an exponent is flatter than, and cannot be reconciled with, the Salpeter-IMF slope of  $\alpha \approx 2.35$ . We confirm that the CMF in a representative sample of high-mass Galactic protoclusters is shallower than the Salpeter slope. We suggest that these massive protoclusters will give birth to top-heavy stellar clusters, or, in order to reconcile with the Universal IMF, the CMF needs to evolve and become Salpeter-like at latter stages of the cluster formation.

Together with this article, we provide the core catalogues for the 15 protoclusters at both the native (1300 to 2700 au) and smoothed (2700 au) linear resolutions. These catalogues include, among other, the sources position, size (in arcsec and in au), peak and integrated fluxes at both 1.3 and 3 mm, their temperature estimates from PPMAP and their estimated mass.

*Acknowledgements.* This paper makes use of the following ALMA data: ADS/JAO.ALMA#2017.1.01355.L. ALMA is a partnership of ESO (representing its member states), NSF (USA) and NINS (Japan), together with NRC (Canada), MOST and ASIAA (Taiwan), and KASI (Republic of Korea), in cooperation with the Republic of Chile. The Joint ALMA Observatory is operated by ESO, AUI/NRAO and NAOJ. This paper also use the following ALMA data: ADS/JAO.ALMA#2013.1.01365.S and ADS/JAO.ALMA#2015.1.01273.S. FL acknowledges support by the Marie Curie Action of the European Union (project *MagiKStar*, Grant agreement number 841276). FM acknowledges the support of the French Agence Nationale de la Recherche (ANR) under reference ANR-20-CE31-009, of the Programme National de Physique Stellaire and Physique et Chimie du Milieu Interstellaire (PNPS and PCMI) of CNRS/INSU (with INC/INP/IN2P3). AG acknowledges support from the NSF under grants AST 2008101 and CAREER 2142300. PS was supported by a Grant-in-Aid for Scientific Research (KAKENHI Number JP22H01271 and JP23H01221) of the Japan Society for the Promotion of Science (JSPS). P.S. and H.-L.L. gratefully acknowledge the support from the NAOJ Visiting Fellow Program to visit the National Astronomical Observatory of Japan in 2019, February. SB acknowledges support by the French Agence Nationale de la Recherche (ANR) through the project *GENESIS* (ANR-16-CE92-0035-01). T. Cs. has received financial support from the French State in the framework of the IdEx Université de Bordeaux Investments for the future Program. RG-M and TN acknowledge support from UNAM-PAPIIT project IN108822 and from CONACYT Ciencia de Frontera project ID: 86372. AS gratefully acknowledges support by the Fondecyt Regular (project code 1220610), and ANID BASAL project FB210003. LB gratefully acknowledges support by the ANID BASAL projects ACE210002 and FB210003. NC acknowledges funding from the ERC under the European Union's Horizon 2020 research and innovation programme (ECOGAL, grant agreement no. 855130). GB acknowledges funding from the State Agency for Research (AEI) of the Spanish MCIU through the AYA2017-84390-C2-2-R grant. GB and ALS acknowledges funding from the European Research Council (ERC) under the European Union's Horizon 2020 research and innovation programme, for the Project "The Dawn of Organic Chemistry" (DOC), grant agreement No 741002. TB acknowledges the support from S. N. Bose National Centre for Basic Sciences under the Department of Science and Technology, Govt. of India. MB is a postdoctoral fellow in the University of Virginia's VICO collaboration and is funded by grants from the NASA Astrophysics Theory Program (grant number 80NSSC18K0558) and the NSF Astronomy & Astrophysics program (grant number 2206516). The project leading to this publication has received support from ORP, that is funded by the European Union's Horizon 2020 research and innovation programme under grant agreement No 101004719.

## References

- Alstott, J., Bullmore, E., & Plen, D. 2014, PLoS ONE, 9, e85777
- Alves, J., Lombardi, M., & Lada, C. J. 2007, A&A, 462, L17
- Bastian, N., Covey, K. R., & Meyer, M. R. 2010, ARA&A, 48, 339
- Bonfand, M., Csengeri, T., Bontemps, S., et al. 2024, arXiv e-prints, arXiv:2402.15023
- Bonnor, W. B. 1956, MNRAS, 116, 351
- Bontemps, S., Motte, F., Csengeri, T., & Schneider, N. 2010, A&A, 524, A18
- Cheng, Y., Tan, J. C., Liu, M., et al. 2018, ApJ, 853, 160
- Clauset, A., Shalizi, C. R., & Newman, M. E. J. 2009, SIAM Review, 51, 661
- Csengeri, T., Bontemps, S., Wyrowski, F., et al. 2017, A&A, 600, L10
- Dell’Ova, P., Motte, F., Gusdorf, A., et al. 2024, arXiv e-prints, arXiv:2407.07610
- Fiorellino, E., Elia, D., André, P., et al. 2021, MNRAS, 500, 4257
- Garrod, R. T., Vasyunin, A. I., Semenov, D. A., Wiebe, D. S., & Henning, T. 2009, ApJ, 700, L43
- Ginsburg, A., Csengeri, T., Galván-Madrid, R., et al. 2022, A&A, 662, A9
- Ginsburg, A., Goddi, C., Kruijssen, J. M. D., et al. 2017, ApJ, 842, 92
- Girart, J. M., Fernández-López, M., Li, Z. Y., et al. 2018, ApJ, 856, L27
- Goddi, C., Ginsburg, A., Maud, L. T., Zhang, Q., & Zapata, L. A. 2020, ApJ, 905, 25
- Hennebelle, P. & Chabrier, G. 2008, ApJ, 684, 395
- Izquierdo, A. F., Galván-Madrid, R., Maud, L. T., et al. 2018, MNRAS, 478, 2505
- Koen, C. & Kondlo, L. 2009, MNRAS, 397, 495
- Kong, S. 2019, ApJ, 873, 31
- Könyves, V., André, P., Men’shchikov, A., et al. 2010, A&A, 518, L106
- Lin, Y., Csengeri, T., Wyrowski, F., et al. 2019, A&A, 631, A72
- Liu, M., Tan, J. C., Cheng, Y., & Kong, S. 2018, ApJ, 862, 105
- Louvet, F., Dougados, C., Cabrit, S., et al. 2018, A&A, 618, A120
- Louvet, F., Hennebelle, P., Men’shchikov, A., et al. 2021, A&A, 653, A157
- Louvet, F., Motte, F., Hennebelle, P., et al. 2014, A&A, 570, A15
- Lu, J. R., Do, T., Ghez, A. M., et al. 2013, ApJ, 764, 155
- Marsh, K. A., Whitworth, A. P., & Lomax, O. 2015, MNRAS, 454, 4282
- Men’shchikov, A. 2013, A&A, 560, A63
- Men’shchikov, A. 2017, A&A, 607, A64
- Men’shchikov, A. 2021a, A&A, 654, A78
- Men’shchikov, A. 2021b, A&A, 649, A89
- Men’shchikov, A., André, P., Didelon, P., et al. 2012, A&A, 542, A81
- Molinari, S., Schisano, E., Faustini, F., et al. 2011, A&A, 530, A133
- Molinari, S., Swinyard, B., Bally, J., et al. 2010, PASP, 122, 314
- Moser, E., Liu, M., Tan, J. C., et al. 2020, ApJ, 897, 136
- Motte, F., André, P., & Neri, R. 1998, A&A, 336, 150
- Motte, F., Bontemps, S., Csengeri, T., et al. 2022, A&A, 662, A8
- Motte, F., Nony, T., Louvet, F., et al. 2018, Nature Astronomy, 2, 478
- Motte, F., Zavagno, A., Bontemps, S., et al. 2010, A&A, 518, L77
- Olguin, F. A., Sanhueza, P., Chen, H.-R. V., et al. 2023, ApJ, 959, L31
- Olguin, F. A., Sanhueza, P., Ginsburg, A., et al. 2022, ApJ, 929, 68
- Olguin, F. A., Sanhueza, P., Guzmán, A. E., et al. 2021, ApJ, 909, 199
- O’Neill, T. J., Cosentino, G., Tan, J. C., Cheng, Y., & Liu, M. 2021, ApJ, 916, 45
- Ossenkopf, V. & Henning, T. 1994, A&A, 291, 943
- Pillai, T. & Simplif Team. 2023, in American Astronomical Society Meeting Abstracts, Vol. 55, American Astronomical Society Meeting Abstracts, 308.03
- Pouteau, Y., Motte, F., Nony, T., et al. 2022, arXiv e-prints, arXiv:2203.03276
- Salpeter, E. E. 1955, ApJ, 121, 161
- Sanhueza, P., Contreras, Y., Wu, B., et al. 2019, ApJ, 886, 102
- Schneider, F. R. N., Sana, H., Evans, C. J., et al. 2018, Science, 359, 69
- Schuller, F., Menten, K. M., Contreras, Y., et al. 2009, A&A, 504, 415
- Vaillancourt, J. 2016, Characterizing the FIR polarization spectrum in Galactic Clouds, SOFIA Proposal, Cycle 5, ID. 05\_0038
- <sup>8</sup> Laboratoire d’astrophysique de Bordeaux, Univ. Bordeaux, CNRS, B18N, allée Geoffroy Saint-Hilaire, 33615 Pessac, France
- <sup>9</sup> Department of Astronomy, University of Florida, PO Box 112055, USA
- <sup>10</sup> Herzberg Astronomy and Astrophysics Research Centre, National Research Council of Canada, 5071 West Saanich Road, Victoria, BC CANADA V9E 2E7
- <sup>11</sup> Laboratoire de Physique de l’École Normale Supérieure, ENS, Université PSL, CNRS, Sorbonne Université, Université de Paris, Paris, France
- <sup>12</sup> Observatoire de Paris, PSL University, Sorbonne Université, LERMA, 75014, Paris, France
- <sup>13</sup> Departament de Física Quàntica i Astrofísica (FQA), Universitat de Barcelona (UB), c. Martí i Franquès, 1, 08028 Barcelona, Spain
- <sup>14</sup> Institut de Ciències del Cosmos (ICCUB), Universitat de Barcelona (UB), c. Martí i Franquès, 1, 08028 Barcelona, Spain
- <sup>15</sup> Institut d’Estudis Espacials de Catalunya (IEEC), 08340, Barcelona, Catalonia, Spain
- <sup>16</sup> Institute of Astronomy, National Tsing Hua University, Hsinchu 30013, Taiwan
- <sup>17</sup> Instituto Argentino de Radioastronomía (CCT-La Plata, CONICET; CICPBA), C.C. No. 5, 1894, Villa Elisa, Buenos Aires, Argentina
- <sup>18</sup> Department of Astronomy, Yunnan University, Kunming, 650091, PR China
- <sup>19</sup> Shanghai Astronomical Observatory, Chinese Academy of Sciences, 80 Nandan Road, Shanghai 200030, People’s Republic of China
- <sup>20</sup> Department of Astronomy, The University of Tokyo, 7-3-1 Hongo, Bunkyo, Tokyo 113-0033, Japan
- <sup>21</sup> S. N. Bose National Centre for Basic Sciences, Block JD, Sector III, Salt Lake, Kolkata 700106, India
- <sup>22</sup> ESO Headquarters, Karl-Schwarzschild-Str 2 D-85748 Garching
- <sup>23</sup> Institut de Radioastronomie Millimétrique (IRAM), 300 rue de la Piscine, 38406 Saint-Martin-D’Hères, France
- <sup>24</sup> National Radio Astronomy Observatory, PO Box O, Socorro, NM 87801 USA
- <sup>25</sup> Departments of Astronomy and Chemistry, University of Virginia, Charlottesville, VA 22904, USA
- <sup>26</sup> Steward Observatory, University of Arizona, 933 North Cherry Avenue, Tucson, AZ 85721, USA
- <sup>27</sup> Université Paris Cité, Université Paris-Saclay, CEA, CNRS, AIM, F-91190 Gif-sur-Yvette, France

<sup>1</sup> Univ. Grenoble Alpes, CNRS, IPAG, 38000 Grenoble, France. e-mail: fabien.louvet@univ-grenoble-alpes.fr

<sup>2</sup> DAS, Universidad de Chile, 1515 camino el observatorio, Las Condes, Santiago, Chile

<sup>3</sup> National Astronomical Observatory of Japan, National Institutes of Natural Sciences, 2-21-1 Osawa, Mitaka, Tokyo 181-8588, Japan

<sup>4</sup> Department of Astronomical Science, SOKENDAI (The Graduate University for Advanced Studies), 2-21-1 Osawa, Mitaka, Tokyo 181-8588, Japan

<sup>5</sup> Departamento de Astronomía, Universidad de Concepción, Casilla 160-C, 4030000 Concepción, Chile

<sup>6</sup> Université Paris-Saclay, Université Paris Cité, CEA, CNRS, AIM, 91191 Gif-sur-Yvette, France

<sup>7</sup> Instituto de Radioastronomía y Astrofísica, Universidad Nacional Autónoma de México, Morelia, Michoacán 58089, México



## Appendix A: Core completeness tests in ALMA-IMF observations

We display the completeness tests for each of the 15 ALMA-IMF fields. We define the completeness as the mass limit above which more than 90 % of the synthetic cores get extracted.

## Appendix B: Effect of the smoothing on the *GExt2D* extractions

We show the effect of smoothing the maps on the source sizes derived by *GExt2D*. Figure B.1 shows the scatter plot of all source sizes before (left panel) and after (right panel) smoothing the maps to a match spacial scale of 2700 au.

## Appendix C: Continuum maps overlaid by both *getsf* and *GExt2D* sources

In this Appendix, we display for each field the sources extracted by *getsf* and by *GExt2D*. In Fig. C.1, we show the sources extracted by *getsf* only with blue ellipses, those extracted by *GExt2D* only with green ellipses, and those extracted by both algorithms with black ellipses.

## Appendix D: Table of sources, after smoothing the maps

In this Appendix, we show the core catalogues for each of the 15 protoclusters. The first group of sources in each table corresponds to thermal dust cores that are gravitationally bound, and the second group corresponds to sources whose fluxes are arguably contaminated by free-free emission. All the tables are available on the ALMA-IMF website (<https://www.almaimf.com/>), and on CDS.

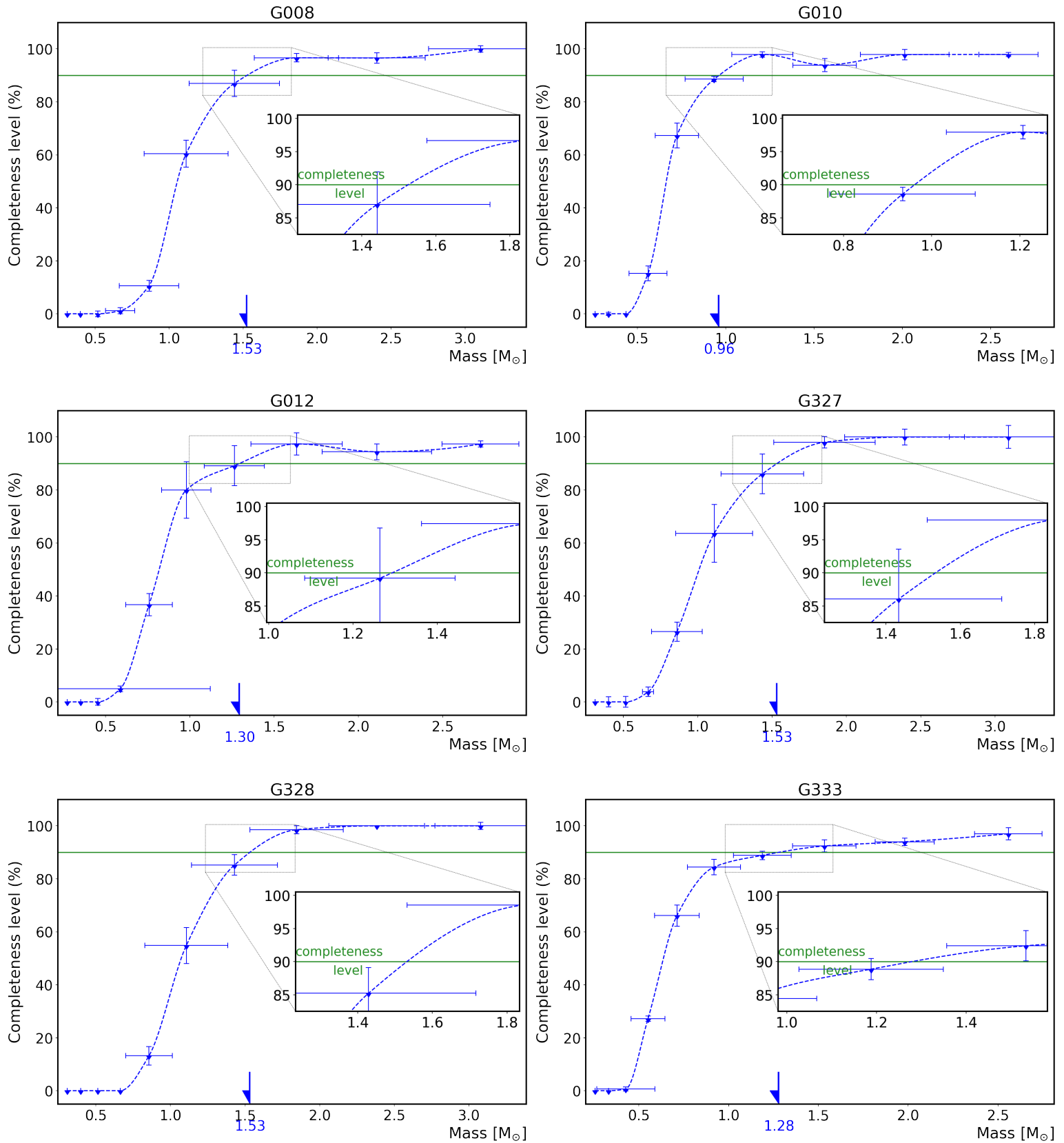


Fig. A.1: Core completeness tests on the ALMA-IMF fields. The curve shows the percentage of synthetic cores extracted as a function of their mass. The green line shows the 90 % threshold.

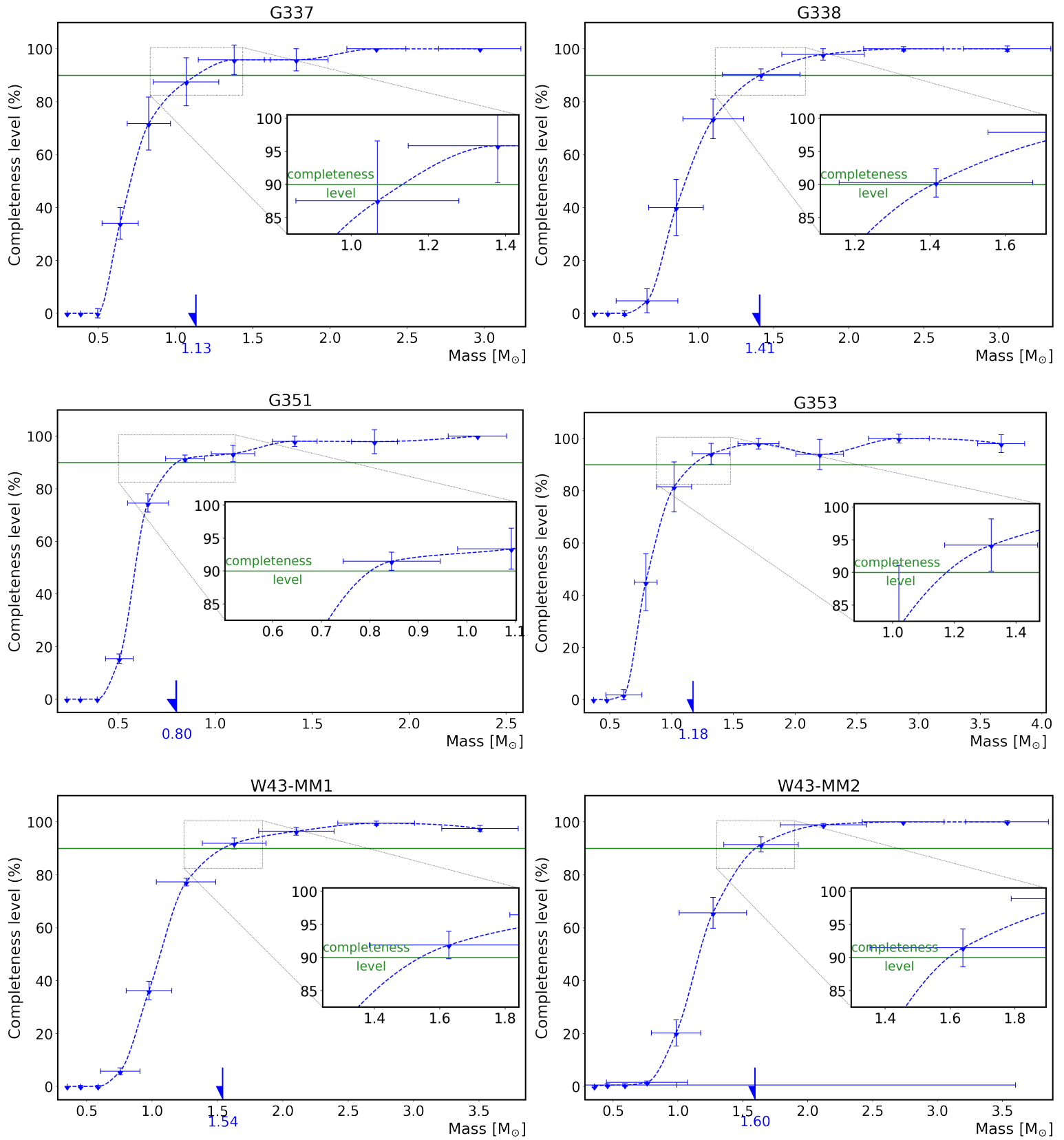


Fig. A.1: Completeness tests (continued).

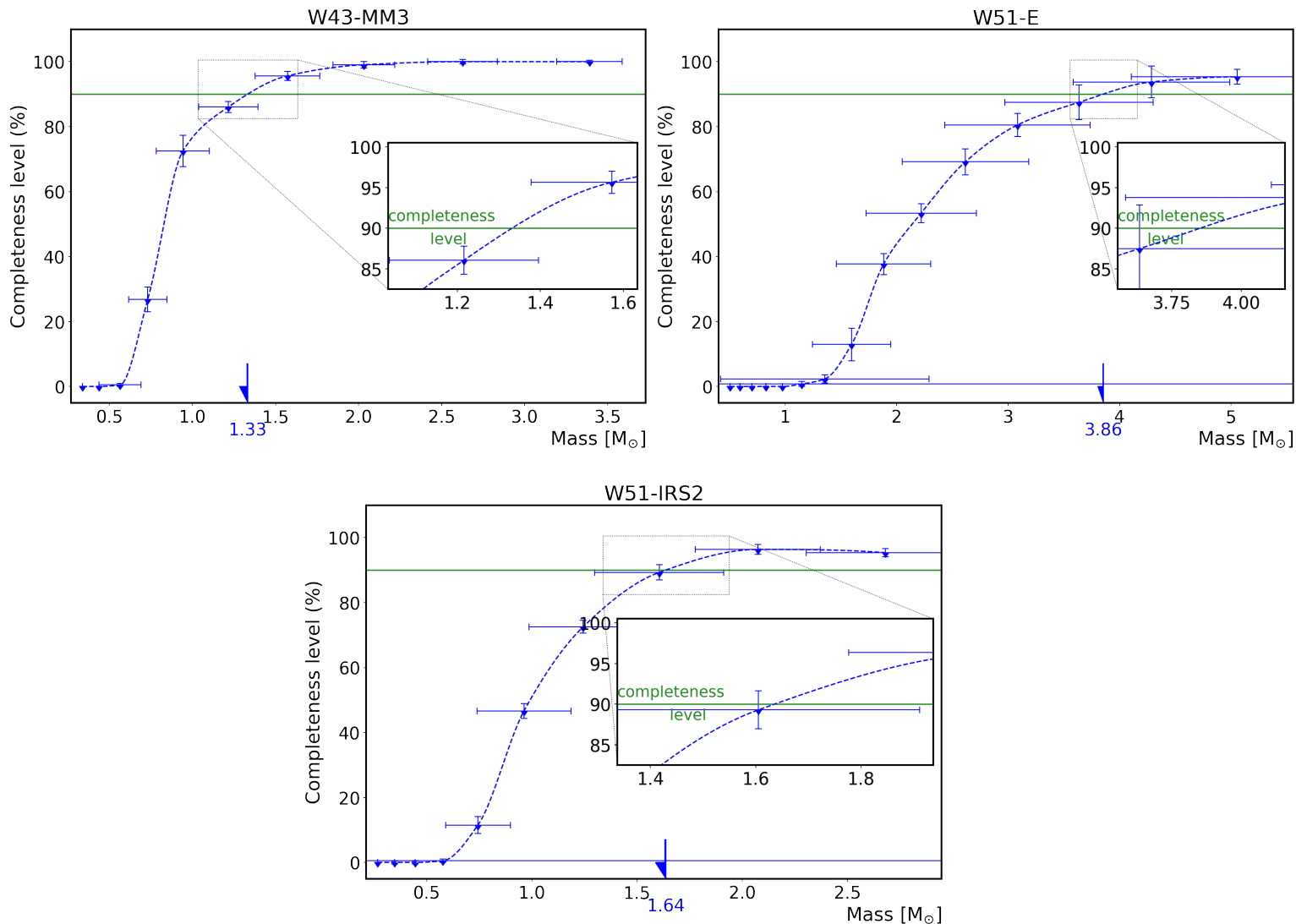


Fig. A.1: Completeness tests (continued).

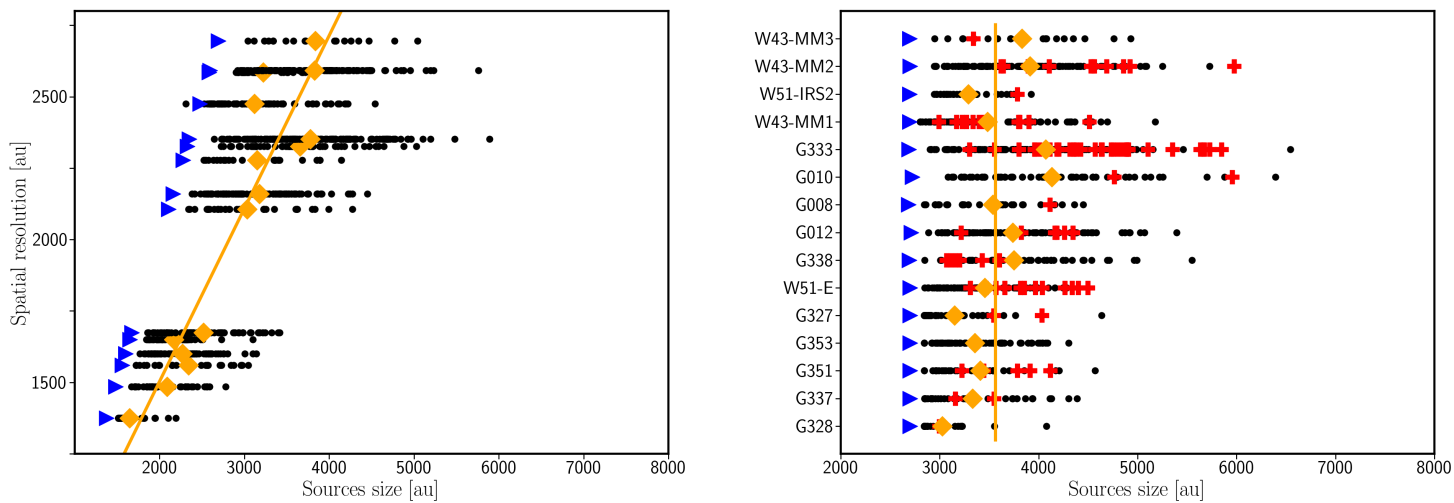


Fig. B.1: Same as Fig. 1 for the sources extracted by GExt2D.

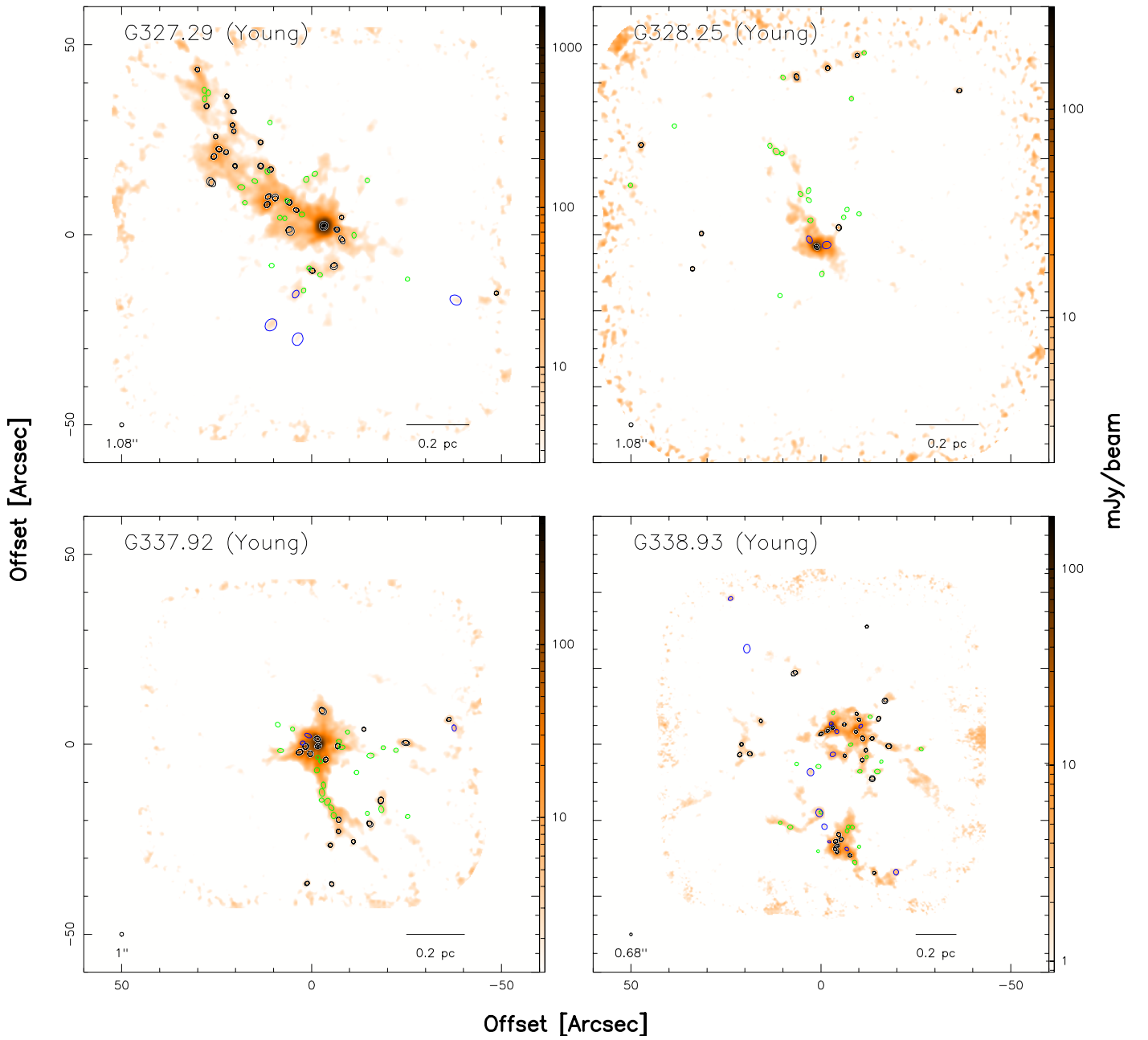


Fig. C.1: Continuum emission maps at 1.3 mm for the 15 ALMA-IMF fields with a spatial resolution of 2700 au. The ellipses locate all the cores found by *getsf* in blue, by *GExt2D* in green, and by both algorithms in black. The field name is indicated in the top left corner of each panel, its evolutionary stage next to the field name, and the beam size in the bottom left corner.

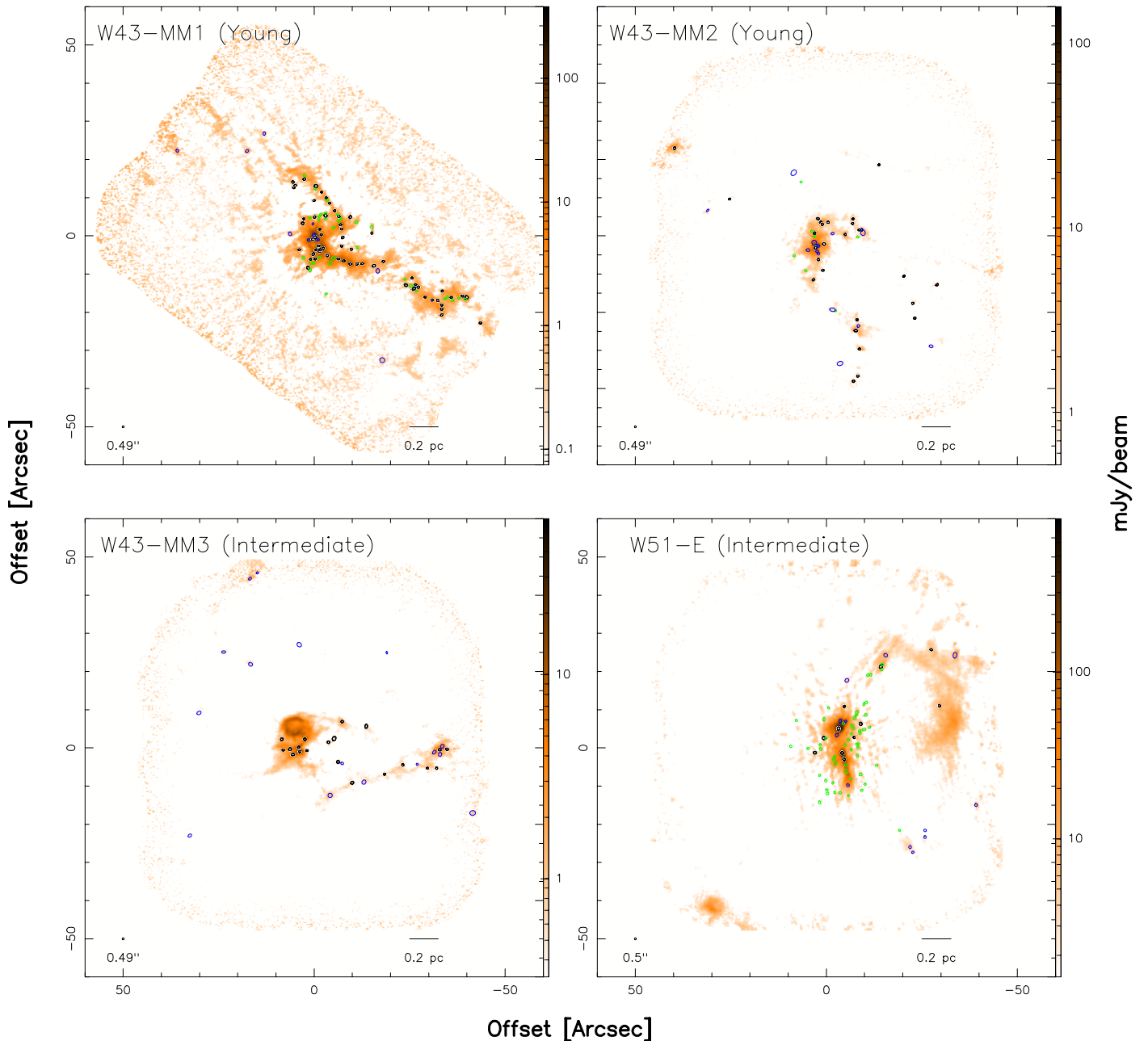


Fig. C.1: Continuum emission maps at 1.3 mm. Continued.

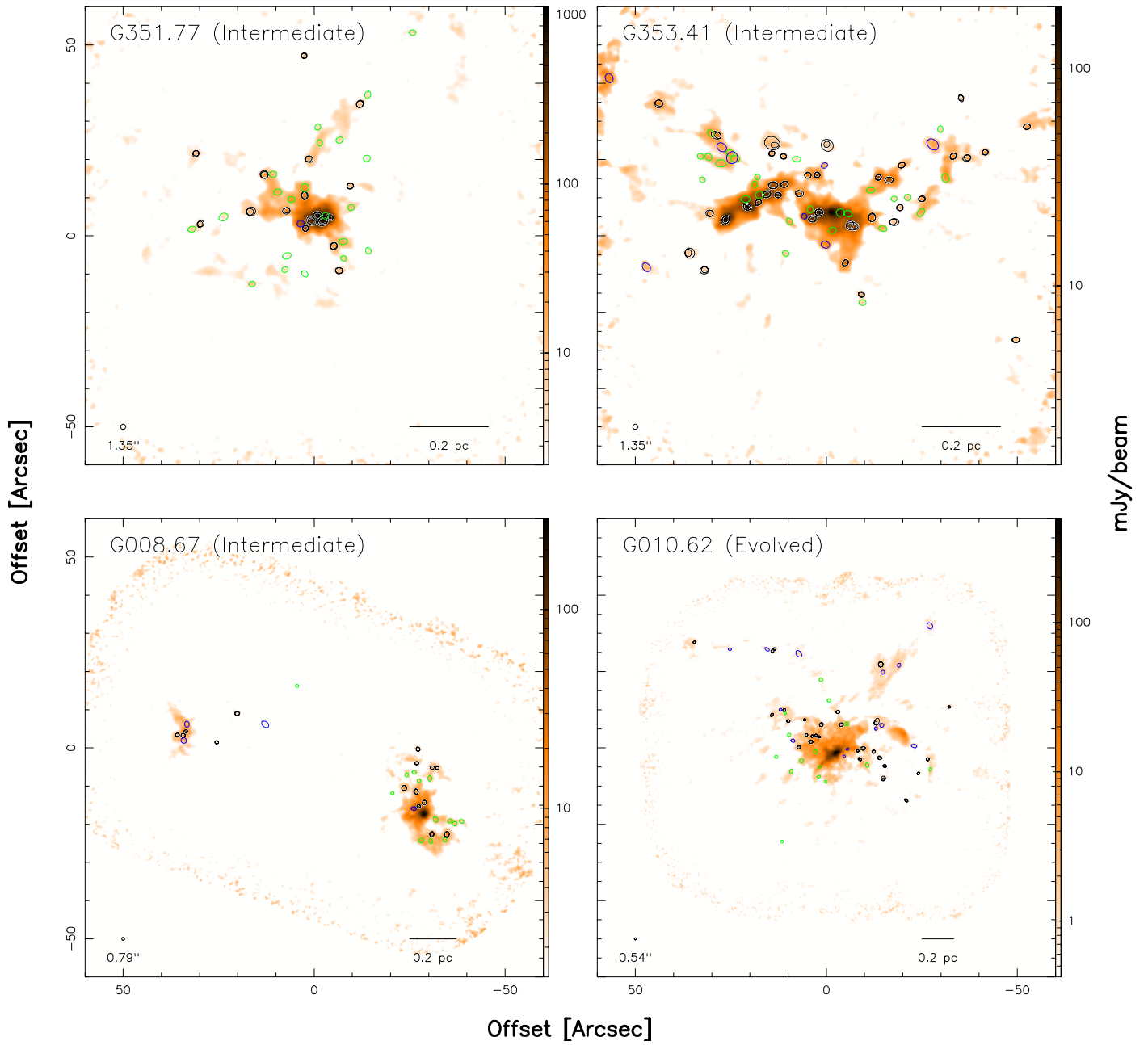


Fig. C.1: Continuum emission maps at 1.3 mm. Continued.

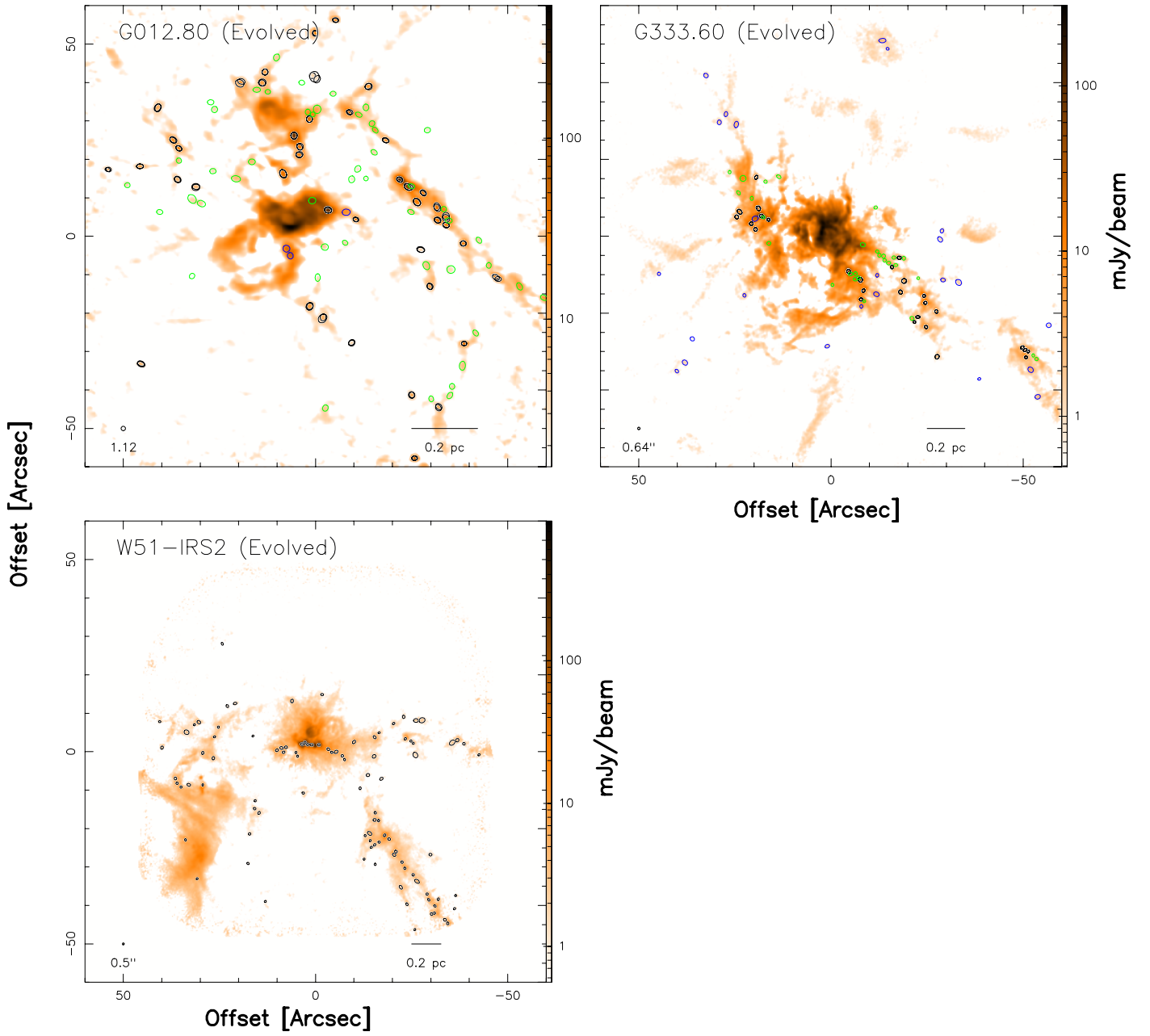


Fig. C.1: Continuum emission maps at 1.3 mm. Continued.



Table D.1: Compact sources extracted by *getsf* in G327, after smoothing.

n	Core name	RA [IRCS]	DEC [ICRS]	1.3 mm				3 mm				T [K]	Mass <sup>(1)</sup> [ $M_{\odot}$ ]	Size <sup>(1)</sup> [au]	$\alpha_{BE}^{(1)}$	$\alpha$	GExt2D
				$a \times b$ ["x"/']	PA [deg]	$S^{Peak}$ [mJy.Beam <sup>-1</sup> ]	$S^{int}$ [mJy]	$a \times b$ ["x"/']	PA [deg]	$S^{Peak}$ [mJy.Beam <sup>-1</sup> ]	$S^{int}$ [mJy]						
1	238.28234-54.61840	15:53:7.760	-54:37:6.250	2.14x2.09	164	1781.0±10.1	7896.0±24.0	2.22x2.10	24	90.7±0.8	392.9±1.7	300±100	49.5±0.1	5264	0.13	3.7	T
2	238.28948-54.61686	15:53:9.480	-54:37:0.680	1.78x1.50	152	169.8±6.7	383.0±8.3	1.75x1.52	128	17.2±0.7	34.9±0.8	100±50	7.0±0.1	3972	0.23	2.9	T
3	238.28066-54.61868	15:53:7.360	-54:37:7.250	1.62x1.47	62	118.9±7.7	195.6±6.0	1.52x1.28	79	9.8±1.1	17.8±1.0	42±11	9.3±0.3	3790	0.07	2.9	T
4	238.29370-54.61149	15:53:10.49	-54:36:41.37	1.20x1.19	7	51.8±1.9	62.1±1.7	1.33x1.19	176	3.9±0.6	4.0±0.4	27±07	4.7±0.1	2990	0.07	3.4	T
5	238.29559-54.61280	15:53:10.94	-54:36:46.10	1.70x1.45	64	73.4±4.0	150.3±4.4	1.62x1.42	70	5.9±0.5	11.8±0.6	100±50	2.7±0.1	3824	0.56	3.1	T
6	238.29386-54.61105	15:53:10.53	-54:36:39.78	1.24x1.19	53	48.9±2.2	62.2±2.1	1.35x1.14	49	5.3±0.5	5.9±0.4	27±07	4.8±0.2	3022	0.07	2.9	T
7	238.29620-54.61335	15:53:11.09	-54:36:48.07	1.60x1.41	129	52.0±4.1	100.1±4.3	1.43x1.30	100	6.8±0.5	12.7±0.7	25±06	8.4±0.3	3676	0.05	2.5	T
8	238.29831-54.60699	15:53:11.59	-54:36:25.17	1.32x1.19	16	43.9±4.5	55.1±3.8	1.46x1.19	52	3.9±0.8	4.4±0.6	27±07	4.3±0.3	3082	0.08	3.1	T
9	238.28583-54.61726	15:53:8.600	-54:37:2.120	1.39x1.13	73	57.6±10.2	70.4±7.9	1.40x1.21	70	7.0±0.8	8.6±0.6	36±09	3.9±0.4	3032	0.11	2.6	T
10	238.26055-54.62332	15:53:2.530	-54:37:23.96	1.16x1.04	134	31.4±3.1	30.3±2.4	1.23x0.98	45	2.6±0.4	2.1±0.3	25±06	2.6±0.2	2700	0.10	3.3	T
11	238.28003-54.61943	15:53:7.210	-54:37:9.940	2.35x1.32	32	38.0±3.1	89.3±5.7	-	-	-	-	36±09	5.0±0.3	4000	0.12	-	T
12	238.28385-54.62167	15:53:8.120	-54:37:18.01	1.72x1.38	59	21.9±2.3	39.1±2.2	1.94x1.64	48	2.8±0.3	4.9±0.3	27±07	3.0±0.2	3708	0.14	2.5	T
13	238.29034-54.61231	15:53:9.680	-54:36:44.31	1.35x1.26	36	16.7±1.8	24.8±2.0	-	-	-	-	25±06	2.1±0.2	3230	0.16	-	T
14	238.29716-54.60965	15:53:11.32	-54:36:34.75	1.34x1.26	163	22.3±4.1	28.1±3.2	-	-	-	-	27±07	2.2±0.2	3216	0.16	-	T
15	238.28677-54.61666	15:53:8.830	-54:36:59.98	1.76x1.44	47	46.8±8.7	84.5±8.0	1.91x1.48	55	5.3±0.7	9.4±0.6	33±08	5.2±0.5	3850	0.10	2.7	T
16	238.28910-54.61430	15:53:9.380	-54:36:51.49	1.64x1.47	114	31.8±5.7	60.8±5.6	1.79x1.58	124	2.9±0.6	5.1±0.5	27±07	4.7±0.4	3816	0.09	3.0	T
17	238.28939-54.61629	15:53:9.450	-54:36:58.64	1.48x1.21	114	36.6±5.0	49.8±3.9	-	-	-	-	29±07	3.5±0.3	3246	0.11	-	T
18	238.28010-54.61779	15:53:7.220	-54:37:4.040	1.14x1.03	76	21.1±6.1	19.8±4.7	1.19x1.11	58	2.5±0.8	2.2±0.5	36±09	1.1±0.3	2656	0.36	2.7	T
19	238.28106-54.62136	15:53:7.450	-54:37:16.90	1.99x1.76	113	12.1±2.0	33.5±2.5	-	-	-	-	28±07	2.4±0.2	4586	0.22	-	T
20	238.29353-54.61406	15:53:10.45	-54:36:50.60	1.36x1.10	26	12.2±2.3	14.1±1.8	1.38x1.15	0	2.1±0.4	2.4±0.3	25±06	1.2±0.1	2946	0.25	2.2	T
21	238.29600-54.61189	15:53:11.04	-54:36:42.81	1.18x1.12	15	13.5±3.7	14.2±2.8	-	-	-	-	25±06	1.2±0.2	2854	0.25	-	T
22	238.28844-54.61632	15:53:9.230	-54:36:58.77	1.83x1.64	171	21.9±5.2	41.7±4.3	1.99x1.32	171	3.2±0.6	6.0±0.6	29±07	3.0±0.3	4250	0.17	2.4	T
23	238.29468-54.61303	15:53:10.72	-54:36:46.92	1.37x1.29	113	17.3±4.9	23.1±3.8	-	-	-	-	26±07	1.9±0.3	3300	0.19	-	T
24	238.26565-54.62382	15:53:3.760	-54:37:25.76	3.18x2.47	59	5.7±0.6	37.0±1.1	-	-	-	-	24±06	3.2±0.1	6710	0.21	-	F
25	238.28657-54.61877	15:53:8.780	-54:37:7.560	2.44x2.21	17	12.8±4.2	50.2±5.3	-	-	-	-	33±08	3.0±0.3	5706	0.26	-	T
26	238.29665-54.61517	15:53:11.20	-54:36:54.61	2.24x1.92	16	11.5±3.3	34.0±3.7	-	-	-	-	23±06	3.2±0.3	5046	0.14	-	T
27	238.29457-54.60894	15:53:10.70	-54:36:32.20	1.24x1.02	8	10.1±2.3	10.8±2.3	-	-	-	-	26±07	0.9±0.2	2728	0.33	-	T
28	238.28899-54.62564	15:53:9.360	-54:37:32.31	3.44x2.78	138	5.3±1.1	38.1±1.8	-	-	-	-	21±05	4.0±0.2	7460	0.16	-	F
29	238.29030-54.61403	15:53:9.670	-54:36:50.52	1.66x1.56	59	9.4±3.4	16.5±2.9	-	-	-	-	26±07	1.3±0.2	3978	0.31	-	T
30	238.29380-54.61005	15:53:10.51	-54:36:36.19	1.43x1.18	88	7.4±2.6	9.4±2.0	-	-	-	-	25±06	0.8±0.2	3140	0.42	-	T
31	238.28564-54.62668	15:53:8.550	-54:37:36.06	3.37x2.73	159	3.1±0.8	18.5±1.5	-	-	-	-	21±05	1.9±0.2	7320	0.34	-	F
34	238.28568-54.62339	15:53:8.610	-54:37:24.21	2.18x1.52	149	5.4±1.6	17.4±2.3	-	-	-	-	23±06	1.6±0.2	4282	0.24	-	F

Notes. The coordinates are given at the J2000 Epoch. (1) Estimated from the measures at 1.3 mm. (2) Indicates if the source found by *getsf* was also found by GExt2D (True or False). The \* next to the uncertainty indicates that the true value is <0.05.

Table D.2: Compact sources extracted by *getsf* in G328, after smoothing.

n	Core name	RA [J2000]	DEC [J2000]	1.3 mm			3 mm			$S^{\text{int}}$ [mJy]	T [K]	Mass <sup>(1)</sup> [ $M_{\odot}$ ]	Size <sup>(1)</sup> [au]	$\alpha_{\text{BE}}^{(1)}$	$\alpha$	GExt2D <sup>(2)</sup>
				$a \times b$ ["x"]	PA [deg]	$S^{\text{Peak}}$ [mJy.Beam <sup>-1</sup> ]	$a \times b$ ["x"]	PA [deg]	$S^{\text{Peak}}$ [mJy.Beam <sup>-1</sup> ]							
1	239.4918-53.96685	15:57:59.80	-53:58:0.660	1.49x1.32	29	300.3±2.5	599.2±4.1	1.54x1.42	10	20.2±0.3	37.3±0.4	100±50	11.5±0.1	0.12	3.4	T
2	239.49784-53.95377	15:57:59.48	-53:57:13.58	1.28x1.16	12	25.3±1.6	30.5±1.4	1.25x1.17	95	3.0±0.1	3.4±0.1	24±06	2.8±0.1	0.10	2.7	T
3	239.50170-53.95443	15:58:0.410	-53:57:15.96	1.81x1.30	14	21.2±1.2	39.6±1.3	1.52x1.36	52	2.4±0.2	4.5±0.2	24±06	3.6±0.1	0.10	2.7	T
4	239.49716-53.95284	15:57:58.60	-53:57:10.24	1.15x1.07	135	23.0±1.4	23.2±1.2	1.38x0.85	111	3.0±0.2	3.2±0.2	23±06	2.2±0.1	0.12	2.5	T
5	239.52100-53.95941	15:58:5.040	-53:57:33.87	1.32x1.19	145	16.2±1.6	20.0±1.3	1.61x1.23	173	2.0±0.2	2.9±0.2	24±06	1.8±0.1	0.17	2.4	T
6	239.48150-53.95543	15:57:55.56	-53:57:19.55	1.34x1.07	118	9.3±0.9	11.2±0.8	1.69x1.35	142	1.6±0.2	1.9±0.1	23±06	1.1±0.1	0.25	2.2	T
7	239.51352-53.96588	15:58:3.250	-53:57:57.15	1.23x1.01	175	6.8±0.6	6.9±0.5	-	-	-	-	24±06	0.6±0.1*	0.42	-	T
8	239.51462-53.96846	15:58:3.510	-53:58:6.460	1.14x1.12	108	5.8±0.7	5.9±0.5	-	-	-	-	24±06	0.5±0.1*	0.53	-	T
9	239.50009-53.96631	15:58:0.020	-53:57:58.72	2.02x1.41	30	17.5±2.6	39.5±2.0	-	-	-	-	38±10	2.1±0.1	0.29	-	F
10	239.49797-53.96671	15:57:59.51	-53:58:0.160	2.31x1.93	102	15.8±4.0	44.6±4.1	-	-	-	-	38±10	2.3±0.2	0.34	-	F
11	239.49647-53.96543	15:57:59.15	-53:57:55.53	1.60x1.26	3	7.0±2.1	10.9±2.1	-	-	-	-	34±09	0.6±0.1	0.74	-	T

**Notes.** The coordinates are given at the J2000 Epoch. (1) Estimated from the measures at 1.3 mm. (2) Indicates if the source found by *getsf* was also found by GExt2D (True or False). The \* next to the uncertainty indicates that the true value is <0.05.

Table D.3: Compact sources extracted by *getsf* in G337, after smoothing.

n	Core name	RA [J2000]	DEC [J2000]	1.3 mm			3 mm			T [K]	Mass <sup>(1)</sup> [ $M_{\odot}$ ]	Size <sup>(1)</sup> [au]	$\alpha_{\text{BE}}^{(1)}$	$\alpha$	GExt2D
				$a \times b$ ["x"]	PA [deg]	$S^{\text{Peak}}$ [mJy.Beam <sup>-1</sup> ]	$S^{\text{int}}$ [mJy]	$a \times b$ ["x"]	PA [deg]						
1	250.29355-47.13427	16:41:10.45	-47:08:3.380	1.61x1.23	105	491.9±13.3	1007.0±16.9	1.43x1.12	101	41.5±1.1	86.8±1.6	23.7±0.4	0.06	3.0	T
2	250.29362-47.13375	16:41:10.47	-47:08:1.490	1.85x1.27	69	181.6±13.6	392.8±14.7	1.83x1.29	64	17.4±1.1	37.9±1.2	8.7±0.3	0.18	2.9	T
3	250.29490-47.13430	16:41:10.78	-47:08:3.480	1.51x1.35	170	56.4±13.0	105.1±12.0	1.52x1.34	7	4.4±1.2	8.0±1.1	6.2±0.7	0.10	3.2	T
4	250.29226-47.14153	16:41:10.14	-47:08:29.50	1.22x1.06	73	12.0±0.7	15.3±0.6	1.08x1.03	69	1.2±0.1	1.4±0.1	1.8±0.1	0.14	2.9	T
5	250.29556-47.13472	16:41:10.93	-47:08:4.970	1.80x1.46	124	45.1±11.1	98.4±11.0	1.70x1.43	120	3.1±0.9	7.0±1.0	6.1±0.7	0.11	3.3	T
6	250.29135-47.14051	16:41:9.920	-47:08:25.83	1.19x1.15	8	13.2±1.0	17.7±0.9	1.17x1.05	69	1.2±0.1	1.4±0.1	2.0±0.1	0.14	3.1	T
7	250.27949-47.13232	16:41:7.080	-47:07:56.35	1.30x1.01	115	13.0±0.8	18.3±0.8	-	-	-	-	2.1±0.1	0.13	-	T
8	250.29275-47.13527	16:41:10.26	-47:08:6.960	1.46x1.21	122	42.0±10.1	71.0±10.1	1.38x1.22	122	3.8±0.8	6.6±0.8	4.4±0.6	0.12	3.0	T
9	250.29438-47.13484	16:41:10.65	-47:08:5.410	1.52x1.40	162	40.0±14.2	73.4±13.1	1.37x1.34	29	2.9±1.0	5.4±1.1	4.3±0.8	0.14	3.2	T
10	250.28414-47.13405	16:41:8.190	-47:08:2.580	2.14x1.24	83	8.7±0.9	23.1±1.2	1.68x1.44	99	1.2±0.5	3.1±0.7	2.5±0.1	0.15	2.5	T
12	250.29477-47.14432	16:41:10.74	-47:08:39.54	1.29x1.09	122	6.5±1.0	8.6±0.8	-	-	-	-	1.1±0.1	0.23	-	T
13	250.29304-47.13170	16:41:10.33	-47:07:54.11	2.23x1.68	43	8.3±2.3	34.0±3.7	-	-	-	-	2.9±0.3	0.20	-	T
14	250.29521-47.13404	16:41:10.85	-47:08:2.540	1.23x1.06	111	18.3±8.2	21.6±6.3	1.27x1.15	101	1.5±0.6	1.7±0.4	1.4±0.4	0.33	3.2	F
15	250.29207-47.14437	16:41:10.10	-47:08:39.74	1.22x1.06	37	4.8±0.7	5.7±0.6	-	-	-	-	0.7±0.1	0.33	-	T
16	250.28861-47.13304	16:41:9.270	-47:07:58.96	1.09x1.03	15	3.9±0.8	4.1±0.7	-	-	-	-	0.4±0.1	0.67	-	T
17	250.29464-47.13350	16:41:10.71	-47:08:0.580	1.81x1.05	66	13.8±6.5	18.7±5.0	1.76x1.06	68	1.3±0.6	1.9±0.5	1.2±0.3	0.43	2.8	F
18	250.28795-47.13998	16:41:9.110	-47:08:23.91	1.71x1.44	46	3.4±0.7	7.2±0.7	-	-	-	-	0.9±0.1	0.43	-	T
19	250.27892-47.13295	16:41:6.940	-47:07:58.60	1.63x1.14	8	4.3±0.7	6.8±0.7	-	-	-	-	0.8±0.1	0.40	-	F
20	250.28678-47.13825	16:41:8.830	-47:08:17.70	1.82x1.41	165	4.2±0.9	9.7±1.3	-	-	-	-	1.1±0.1	0.36	-	T
21	250.28977-47.14126	16:41:9.540	-47:08:28.54	1.21x0.92	2	5.1±0.9	5.2±0.7	-	-	-	-	0.6±0.1	0.36	-	T
23	250.29133-47.13966	16:41:9.920	-47:08:22.78	1.40x1.26	19	6.9±2.5	11.8±2.5	-	-	-	-	1.2±0.3	0.30	-	T
25	250.29142-47.13425	16:41:9.940	-47:08:3.300	1.61x1.36	174	7.1±3.5	8.5±3.5	-	-	-	-	0.6±0.3	0.77	-	T

**Notes.** The coordinates are given at the J2000 Epoch. (1) Estimated from the measures at 1.3 mm. (2) Indicates if the source found by *getsf* was also found by GExt2D (True or False). The \* next to the uncertainty indicates that the true value is <0.05.

Table D.4: Compact sources extracted by *getsf* in G338, after smoothing.

n	Core name	RA [J2000]	DEC [J2000]	1.3 mm			3 mm			T [K]	Mass <sup>(1)</sup> [ $M_{\odot}$ ]	Size <sup>(1)</sup> [au]	$\alpha_{\text{BE}}^{(1)}$	$\alpha$	GExT2D <sup>(2)</sup>
				$a \times b$ [" $\times$ "']	PA [deg]	$S^{\text{Peak}}$ [mJy.Beam <sup>-1</sup> ]	$S^{\text{int}}$ [mJy]	$a \times b$ [" $\times$ "']	PA [deg]						
1	250.14220-45.69340	16:40:34.13	-45:41:36.25	0.89×0.79	84	177.1±2.1	284.3±2.6	0.94×0.85	52	10.0±0.2	17.0±0.3	0.10	3.4	T	
2	250.14273-45.69362	16:40:34.25	-45:41:37.04	0.97×0.73	124	167.8±2.4	271.5±2.5	1.03×0.77	124	14.9±0.3	24.9±0.3	0.10	2.9	T	
3	250.14270-45.70202	16:40:34.01	-45:42:7.290	0.86×0.79	92	119.8±2.5	168.6±2.5	0.88×0.81	110	5.1±0.3	6.9±0.3	0.16	3.9	T	
4	250.14275-45.69370	16:40:34.54	-45:41:37.31	0.87×0.82	7	80.1±1.7	140.0±2.4	0.90×0.86	29	6.3±0.1	11.5±0.2	0.21	3.0	T	
5	250.14274-45.70250	16:40:34.02	-45:42:9.000	0.86×0.79	89	75.4±2.8	103.2±2.5	0.95×0.85	81	6.2±0.3	9.5±0.4	0.04	2.9	T	
6	250.14192-45.70228	16:40:34.06	-45:42:8.210	1.00×0.86	65	68.5±2.8	125.2±3.5	0.96×0.74	77	3.5±0.3	6.9±0.5	0.04	3.5	T	
7	250.13785-45.70402	16:40:33.08	-45:42:14.48	0.81×0.76	56	31.4±1.3	40.7±1.3	0.91×0.75	9	3.2±0.1	4.7±0.1	0.05	2.6	T	
8	250.14340-45.69385	16:40:34.42	-45:41:37.88	1.42×0.88	119	33.8±1.5	59.7±1.4	1.23×0.86	121	2.7±0.2	4.9±0.2	0.04	3.1	T	
9	250.14972-45.69291	16:40:35.93	-45:41:34.47	0.98×0.75	29	11.6±0.4	20.9±0.5	0.94×0.78	48	0.7±0.1	1.0±0.1	0.06	3.7	T	
10	250.14039-45.70273	16:40:33.69	-45:42:9.820	1.02×0.88	63	34.7±2.8	67.8±3.2	1.03×0.87	75	2.1±0.2	3.9±0.2	0.48	3.5	T	
11	250.14093-45.69545	16:40:33.82	-45:41:43.63	0.87×0.74	15	18.6±1.4	24.2±1.2	0.88×0.78	42	1.8±0.1	2.2±0.1	0.09	2.9	T	
12	250.14450-45.69665	16:40:34.68	-45:41:47.94	1.99×1.75	16	2.2±0.9	12.2±1.1	-	-	-	-	0.27	-	F	
13	250.14232-45.69310	16:40:34.16	-45:41:35.17	1.06×1.04	129	26.0±2.2	44.4±1.7	1.02×0.82	112	1.5±0.3	2.8±0.3	0.06	3.4	F	
14	250.13943-45.69282	16:40:33.46	-45:41:34.15	0.87×0.70	72	15.7±2.2	18.5±1.7	1.05×0.79	90	0.9±0.1	1.0±0.1	0.12	3.5	T	
15	250.14619-45.68941	16:40:35.09	-45:41:21.89	1.68×1.26	124	4.4±0.4	19.3±0.7	-	-	-	-	0.13	-	T	
16	250.14189-45.70171	16:40:34.05	-45:42:6.150	1.06×0.98	72	17.5±3.1	29.0±2.4	-	-	-	-	0.15	-	T	
17	250.13904-45.69420	16:40:33.37	-45:41:39.13	1.25×1.05	20	11.3±1.6	26.2±1.7	-	-	-	-	0.16	-	T	
18	250.15086-45.69531	16:40:36.21	-45:41:43.12	1.28×1.10	63	4.9±0.8	12.9±0.9	-	-	-	-	0.15	-	T	
19	250.14094-45.69316	16:40:33.83	-45:41:35.39	0.92×0.89	118	6.5±1.3	9.6±1.1	-	-	-	-	0.25	-	T	
21	250.15286-45.68395	16:40:36.69	-45:41:2.230	1.23×0.99	114	3.4±0.4	9.9±0.5	-	-	-	-	0.19	-	F	
22	250.14358-45.69963	16:40:34.46	-45:41:58.65	2.09×1.82	21	3.3±0.9	21.8±1.6	-	-	-	-	0.17	-	F	
23	250.13909-45.69577	16:40:33.38	-45:41:44.75	1.01×0.89	170	5.8±1.4	10.6±1.4	-	-	-	-	0.26	-	T	
24	250.13864-45.68600	16:40:33.27	-45:41:9.610	0.78×0.75	86	1.9±0.3	2.3±0.2	-	-	-	-	0.60	-	T	
25	250.14176-45.69367	16:40:34.02	-45:41:37.20	1.12×1.03	40	9.2±2.5	16.4±1.9	-	-	-	-	0.17	-	F	
27	250.13967-45.69238	16:40:33.52	-45:41:32.56	0.92×0.73	32	6.0±2.1	7.4±1.6	-	-	-	-	0.27	-	T	
28	250.13871-45.69506	16:40:33.29	-45:41:42.21	0.93×0.81	172	5.1±1.8	7.0±1.4	-	-	-	-	0.42	-	T	
29	250.14130-45.70157	16:40:33.91	-45:42:5.660	1.33×1.10	129	6.4±2.1	14.2±1.9	-	-	-	-	0.34	-	T	
30	250.15173-45.69462	16:40:36.42	-45:41:40.63	1.06×0.88	180	3.8±1.2	7.5±1.2	-	-	-	-	0.21	-	T	
31	250.13807-45.69418	16:40:33.14	-45:41:39.06	1.00×0.91	112	4.7±1.9	7.4±1.5	-	-	-	-	0.46	-	T	
33	250.14155-45.70120	16:40:33.97	-45:42:4.310	1.10×1.00	21	4.5±2.0	7.9±1.5	-	-	-	-	0.46	-	T	
34	250.15190-45.69535	16:40:36.46	-45:41:43.25	1.21×1.05	144	2.6±1.1	5.8±1.0	-	-	-	-	0.32	-	T	
35	250.14306-45.70063	16:40:34.33	-45:42:2.250	1.52×1.39	30	2.3±0.7	8.0±1.0	-	-	-	-	0.43	-	F	
37	250.13670-45.69143	16:40:32.81	-45:41:29.16	1.57×1.47	155	3.4±0.6	14.7±0.8	-	-	-	-	0.23	-	T	
38	250.13556-45.70396	16:40:32.53	-45:42:14.24	1.53×1.29	180	2.4±0.9	7.9±1.0	-	-	-	-	0.32	-	F	
39	250.15117-45.68761	16:40:36.28	-45:41:15.40	2.35×1.71	179	1.1±0.3	6.9±0.7	-	-	-	-	0.48	-	F	
40	250.14253-45.70174	16:40:34.21	-45:42:6.270	0.83×0.57	71	4.8±2.2	4.5±1.7	-	-	-	-	0.57	-	F	
41	250.13635-45.69476	16:40:32.72	-45:41:41.14	1.33×1.24	80	3.9±1.4	11.0±1.5	-	-	-	-	0.32	-	T	
42	250.13806-45.69716	16:40:33.13	-45:41:49.79	1.50×1.26	90	2.0±0.7	6.4±1.0	-	-	-	-	0.45	-	T	
43	250.13925-45.69329	16:40:33.42	-45:41:35.84	1.20×0.80	134	4.0±2.0	7.4±1.6	-	-	-	-	0.42	-	F	
45	250.13739-45.69275	16:40:32.97	-45:41:33.90	1.44×0.97	157	2.3±1.0	5.8±1.2	-	-	-	-	0.53	-	T	
46	250.14069-45.70226	16:40:33.77	-45:42:8.150	1.11×0.82	38	6.0±2.4	9.3±1.8	-	-	-	-	0.44	-	F	

Table D.5: Continuation of Table D.4

n	Core name	RA	DEC	1.3 mm			3 mm			T	Mass <sup>(1)</sup>	Size <sup>(1)</sup>	$\alpha_{\text{BE}}^{(1)}$	$\alpha$	GExt2D <sup>(2)</sup>
				$a \times b$	PA	$S^{\text{Peak}}$	$S^{\text{int}}$	$a \times b$	PA						
47	250.14219-45.69534	16:40:34.12	-45:41:43.23	1.47×1.17	106	3.4±1.3	9.7±1.4	-	-	27±07	1.8±0.3	4930	0.30	-	F

**Notes.** The coordinates are given at the J2000 Epoch. (1) Estimated from the measures at 1.3 mm. (2) Indicates if the source found by *getsf* was also found by *GExt2D* (True or False). The \* next to the uncertainty indicates that the true value is  $<0.05$ .



Table D.7: Continuation of Table D.6

n	Core name	RA	DEC	1.3 mm			3 mm			T	Mass <sup>(1)</sup>	Size <sup>(1)</sup>	$\alpha_{\text{BE}}^{(1)}$	$\alpha$	GExt2D <sup>(2)</sup>
				a × b	PA	S <sup>Peak</sup>	a × b	PA	S <sup>Peak</sup>						
43	281.95581-1.901030	18:47:49.39	-01:54:33.710	0.76×0.69	28	2.3±0.3	5.0±0.4	-	25±06	2.0±0.2	3928	0.20	-	F	
44	281.94660-1.905970	18:47:47.18	-01:54:21.49	0.56×0.54	153	4.4±1.3	5.1±1.0	-	25±06	2.1±0.4	2984	0.14	-	T	
45	281.94470-1.904850	18:47:46.73	-01:54:17.47	0.62×0.44	92	5.5±1.2	6.0±0.9	-	25±06	2.5±0.4	2722	0.11	-	T	
46	281.94732-1.903710	18:47:47.36	-01:54:13.36	0.57×0.54	120	2.7±0.4	3.3±0.3	-	23±06	1.4±0.1	3030	0.20	-	T	
47	281.93503-1.911600	18:47:44.41	-01:54:41.77	0.79×0.44	71	5.1±0.6	7.3±0.8	-	25±06	3.0±0.3	2946	0.10	-	T	
48	281.93775-1.911680	18:47:45.06	-01:54:42.04	0.68×0.45	74	2.8±0.6	3.5±0.6	-	24±06	1.5±0.2	2852	0.19	-	T	
49	281.94080-1.909080	18:47:45.79	-01:54:32.68	0.69×0.52	89	2.9±0.6	4.0±0.4	-	24±06	1.6±0.2	3134	0.19	-	T	
50	281.94944-1.899780	18:47:47.87	-01:53:59.20	0.91×0.67	176	1.2±0.2	2.5±0.2	-	24±06	1.1±0.1	4068	0.37	-	F	
51	281.93825-1.910960	18:47:45.18	-01:54:39.45	0.66×0.55	85	2.7±0.7	3.5±0.6	-	25±06	1.4±0.2	3204	0.23	-	T	
52	281.93654-1.912260	18:47:44.77	-01:54:44.14	0.65×0.52	92	3.0±1.1	3.7±0.8	-	25±06	1.5±0.3	3068	0.20	-	T	
53	281.94573-1.908910	18:47:46.98	-01:54:32.08	0.60×0.42	97	8.1±3.4	8.0±2.7	-	25±06	3.2±1.1	2594	0.08	-	T	
54	281.93682-1.911920	18:47:44.84	-01:54:42.93	0.69×0.60	54	2.6±1.1	3.7±0.8	-	24±06	1.6±0.3	3442	0.22	-	T	
55	281.94150-1.909400	18:47:45.96	-01:54:33.85	0.89×0.71	124	1.8±0.4	3.9±0.4	-	24±06	1.6±0.2	4230	0.25	-	T	
56	281.93914-1.910830	18:47:45.39	-01:54:38.98	0.77×0.69	123	1.8±0.7	3.1±0.5	-	24±06	1.3±0.2	3958	0.30	-	T	
58	281.94654-1.903080	18:47:47.17	-01:54:11.09	0.80×0.66	130	2.3±0.8	4.2±0.7	-	24±06	1.8±0.3	3874	0.21	-	T	
59	281.94666-1.906310	18:47:47.20	-01:54:22.72	0.74×0.69	15	2.6±1.1	5.0±1.0	-	25±06	2.0±0.4	3908	0.20	-	T	
60	281.93474-1.911720	18:47:44.34	-01:54:42.20	1.00×0.93	152	2.8±0.6	9.0±0.6	-	25±06	3.6±0.3	5226	0.15	-	T	
61	281.94737-1.903310	18:47:47.37	-01:54:11.90	0.61×0.54	64	1.6±0.4	2.2±0.3	-	23±06	1.0±0.1	3114	0.31	-	T	
62	281.93649-1.911240	18:47:44.76	-01:54:40.45	0.58×0.50	84	2.0±0.8	2.2±0.6	-	24±06	0.9±0.2	2878	0.30	-	T	
63	281.94088-1.916260	18:47:45.81	-01:54:58.54	1.33×1.25	38	0.3±0.1	1.4±0.2	-	27±07	0.5±0.1	7026	1.46	-	F	
64	281.94162-1.907010	18:47:45.99	-01:54:25.24	0.64×0.51	166	2.0±0.5	2.4±0.4	-	25±06	1.0±0.2	3026	0.30	-	T	
66	281.94120-1.909770	18:47:45.89	-01:54:35.17	1.19×0.91	4	1.4±0.5	5.3±0.7	-	24±06	2.3±0.3	5466	0.23	-	F	
67	281.94591-1.906350	18:47:47.02	-01:54:22.86	0.65×0.46	149	3.3±1.3	3.4±1.0	-	26±07	1.3±0.4	2828	0.22	-	F	
68	281.94756-1.907070	18:47:47.42	-01:54:25.46	1.07×0.77	23	1.2±0.4	3.4±0.5	-	25±06	1.4±0.2	4740	0.35	-	F	
69	281.94626-1.909570	18:47:47.10	-01:54:34.44	0.90×0.73	17	2.3±1.1	5.5±1.1	-	24±06	2.3±0.5	4326	0.18	-	T	
70	281.94499-1.905740	18:47:46.80	-01:54:20.67	1.09×0.86	23	2.3±1.0	5.0±1.2	-	24±06	2.1±0.5	5108	0.24	-	T	
73	281.94581-1.905850	18:47:46.99	-01:54:21.07	0.66×0.53	143	2.3±1.1	3.0±0.8	-	25±06	1.2±0.3	3148	0.26	-	T	
74	281.94323-1.905860	18:47:46.37	-01:54:21.10	0.82×0.65	161	1.7±0.7	3.2±0.9	-	25±06	1.3±0.3	3856	0.30	-	T	
75	281.94376-1.907350	18:47:46.50	-01:54:26.45	0.82×0.61	129	1.6±0.5	2.3±0.7	-	25±06	0.9±0.3	3716	0.42	-	T	
19	281.93657-1.910560	18:47:44.78	-01:54:38.01	0.57×0.46	91	3.2±0.2	3.6±0.2	0.65×0.51	118	1.0±0.1	2696	-	1.5	T	

**Notes.** The coordinates are given at the J2000 Epoch. (1) Estimated from the measures at 1.3 mm. (2) Indicates if the source found by *getsf* was also found by *GExt2D* (True or False). The \* next to the uncertainty indicates that the true value is <0.05.

Table D.8: Compact sources extracted by *getsf* in W43-MM2, after smoothing.

n	Core name	RA [J2000]	DEC [J2000]	1.3 mm			3 mm			T [K]	Mass <sup>(1)</sup> [ $M_{\odot}$ ]	Size <sup>(1)</sup> [au]	$\alpha_{BE}^{(1)}$	$\alpha$	GExt2D <sup>(2)</sup>
				$a \times b$ [" $\times$ "']	PA [deg]	$S^{Peak}$ [mJy.Beam <sup>-1</sup> ]	$S^{int}$ [mJy]	$a \times b$ [" $\times$ "']	PA [deg]						
1	281.90332-2.015080	18:47:36.80	-02:00:54.27	0.76×0.70	147	152.4±1.1	423.6±3.2	1.04×0.52	9	6.6±0.1	24.8±0.2	3980	0.04	3.5	T
2	281.90313-2.022430	18:47:36.03	-02:01:20.74	0.78×0.48	84	13.3±0.2	24.5±0.3	0.69×0.51	84	1.4±0.1	2.4±0.1	3118	0.03	2.9	T
3	281.90342-2.021090	18:47:36.10	-02:01:15.94	0.90×0.70	81	14.9±0.5	41.4±0.8	0.78×0.68	81	1.0±0.1	2.5±0.1	4200	0.02	3.5	T
4	281.90363-2.013300	18:47:36.15	-02:00:47.87	0.59×0.52	64	9.0±0.3	11.8±0.3	0.61×0.45	62	0.8±0.1*	1.0±0.1	2988	0.06	3.0	T
5	281.90318-2.014100	18:47:36.28	-02:00:50.76	0.67×0.54	175	11.0±0.4	20.1±0.6	0.70×0.54	174	0.7±0.1*	1.2±0.1	3204	0.71	3.5	T
6	281.90314-2.014930	18:47:36.75	-02:00:53.74	0.79×0.73	56	37.7±1.8	86.8±1.8	1.55×0.56	117	1.6±0.1	1.4±0.1	4112	0.02	5.0	F
7	281.90294-2.013210	18:47:36.71	-02:00:47.55	0.72×0.55	118	15.3±0.7	28.7±1.0	0.77×0.59	123	0.8±0.1	1.3±0.1	3304	0.51	3.8	T
8	281.89626-2.019100	18:47:35.10	-02:01:8.770	0.64×0.55	128	5.9±0.2	10.0±0.3	0.66×0.52	121	0.5±0.1*	0.9±0.1	3174	0.06	3.0	T
9	281.90349-2.017390	18:47:36.84	-02:01:2.620	0.74×0.54	132	9.0±0.5	15.4±0.5	0.79×0.57	151	0.6±0.1	0.9±0.1	3276	0.06	3.5	T
10	281.91360-2.007810	18:47:39.26	-02:00:28.12	0.79×0.74	148	15.1±0.7	57.6±1.6	1.02×0.75	35	0.7±0.1*	1.7±0.1	4178	0.02	4.3	T
11	281.89872-2.009030	18:47:35.69	-02:00:32.52	0.62×0.49	148	3.9±0.2	5.7±0.2	0.69×0.48	132	0.3±0.1*	0.4±0.0	2920	0.11	3.2	T
12	281.90272-2.014790	18:47:36.65	-02:00:53.26	0.86×0.72	86	12.1±1.8	31.1±2.0	0.80×0.73	19	0.5±0.2	1.1±0.2	4208	0.05	4.1	T
13	281.90285-2.013350	18:47:36.68	-02:00:48.07	0.69×0.56	168	9.7±0.7	15.6±0.6	0.75×0.54	162	0.8±0.1	1.3±0.1	3318	0.06	3.1	T
14	281.90025-2.024400	18:47:36.06	-02:01:27.84	0.66×0.57	111	4.2±0.3	6.2±0.3	0.58×0.54	113	0.4±0.1	0.6±0.1	3294	0.12	2.9	T
15	281.90343-2.014690	18:47:36.82	-02:00:52.89	1.33×1.24	22	13.4±2.0	70.6±2.2	-	-	-	-	6988	0.04	-	F
16	281.90061-2.012960	18:47:36.15	-02:00:46.64	0.56×0.48	98	3.3±0.3	3.5±0.2	0.57×0.48	110	0.4±0.1	0.4±0.0	2768	0.17	2.7	T
17	281.90959-2.011520	18:47:38.30	-02:00:41.48	0.57×0.48	104	2.5±0.2	2.6±0.1	-	-	-	-	2786	0.21	-	T
19	281.89988-2.013960	18:47:35.97	-02:00:50.27	1.46×1.20	1	1.5±0.3	8.8±0.6	-	-	-	-	7044	0.18	-	F
20	281.90319-2.015320	18:47:36.77	-02:00:55.16	0.72×0.69	110	12.9±1.2	21.7±0.9	-	-	-	-	3854	0.09	-	F
21	281.90057-2.024780	18:47:36.14	-02:01:29.20	0.62×0.62	48	2.8±0.3	4.6±0.4	-	-	-	-	3402	0.17	-	T
22	281.90341-2.014000	18:47:36.82	-02:00:50.41	0.60×0.54	154	6.2±1.7	7.4±1.4	0.59×0.54	117	0.5±0.1	0.6±0.1	3054	0.11	3.1	T
24	281.90314-2.015480	18:47:36.75	-02:00:55.73	0.71×0.61	107	6.1±1.3	9.9±1.1	-	-	-	-	3540	0.16	-	F
25	281.89451-2.017770	18:47:34.68	-02:01:3.960	0.73×0.57	108	2.0±0.3	4.2±0.3	-	-	-	-	3404	0.18	-	T
26	281.90386-2.015230	18:47:36.93	-02:00:54.82	0.94×0.74	83	4.7±1.0	12.7±0.9	-	-	-	-	4420	0.14	-	F
27	281.90033-2.020300	18:47:36.08	-02:01:13.08	0.51×0.47	74	1.3±0.3	1.6±0.2	-	-	-	-	2664	0.35	-	T
28	281.90316-2.012930	18:47:36.76	-02:00:46.56	0.77×0.65	80	2.1±0.5	3.6±0.5	-	-	-	-	3778	0.27	-	T
29	281.90002-2.013770	18:47:36.00	-02:00:49.56	0.78×0.62	80	1.5±0.5	2.2±0.4	-	-	-	-	3676	0.38	-	T
30	281.90019-2.020750	18:47:36.05	-02:01:14.69	0.78×0.68	136	1.6±0.5	3.0±0.4	-	-	-	-	3908	0.29	-	F
31	281.90210-2.019570	18:47:36.50	-02:01:10.44	1.53×0.97	82	0.9±0.3	4.3±0.5	-	-	-	-	6220	0.30	-	F
32	281.90014-2.013760	18:47:36.03	-02:00:49.54	0.77×0.54	97	2.2±0.3	3.7±0.4	-	-	-	-	3362	0.21	-	T
33	281.90281-2.016700	18:47:36.67	-02:01:0.120	0.69×0.52	92	1.9±0.5	2.5±0.4	-	-	-	-	3144	0.35	-	T
35	281.89692-2.017130	18:47:35.26	-02:01:1.680	0.58×0.50	140	1.0±0.2	1.1±0.2	-	-	-	-	2878	0.53	-	T
36	281.89493-2.022230	18:47:34.78	-02:01:20.02	1.03×0.75	78	1.1±0.2	3.0±0.3	-	-	-	-	4608	0.32	-	F
37	281.90492-2.009600	18:47:37.18	-02:00:34.54	1.69×1.23	139	0.5±0.2	1.9±0.3	-	-	-	-	7512	0.79	-	F
38	281.90241-2.013200	18:47:36.58	-02:00:47.54	0.65×0.55	63	1.8±0.6	2.4±0.4	-	-	-	-	3172	0.35	-	T
39	281.90208-2.014020	18:47:36.50	-02:00:50.48	0.79×0.69	104	1.5±0.5	2.7±0.5	-	-	-	-	3960	0.36	-	F
40	281.89611-2.020190	18:47:35.07	-02:01:12.70	0.66×0.54	75	1.0±0.2	0.6±0.2	-	-	-	-	3168	0.98	-	T
44	281.90313-2.015930	18:47:36.75	-02:00:57.33	0.66×0.62	78	2.1±1.0	3.0±0.8	-	-	-	-	3464	0.38	-	T
46	281.91116-2.012340	18:47:38.68	-02:00:44.41	0.80×0.43	132	1.3±0.3	1.7±0.3	-	-	-	-	2914	0.33	-	F
47	281.90154-2.023480	18:47:36.37	-02:01:24.52	1.52×1.07	110	0.9±0.2	4.0±0.4	-	-	-	-	6608	0.37	-	F

A&amp;A proofs: manuscript no. CMF-in-ALMA-IMF

**Notes.** The coordinates are given at the J2000 Epoch. (1) Estimated from the measures at 1.3 mm. (2) Indicates if the source found by *getsf* was also found by *GExt2D* (True or False). The \* next to the uncertainty indicates that the true value is <0.05.



Table D.9: Compact sources extracted by *getsf* in W43-MM3, after smoothing.

n	Core name	RA [ICRS]	DEC [ICRS]	1.3 mm			3 mm			T [K]	Mass <sup>(1)</sup> [M <sub>⊙</sub> ]	Size <sup>(1)</sup> [au]	α <sub>BE</sub> <sup>(1)</sup>	α	GExt2D
				a × b ["×"/]	PA [deg]	S <sup>Peak</sup> [mJy.Beam <sup>-1</sup> ]	S <sup>int</sup> [mJy]	a × b ["×"/]	PA [deg]						
1	281.92380-2.007940	18:47:41.71	-02:00:28.60	0.65×0.50	90	52.0±2.0	82.2±2.6	0.79×0.56	103	2.8±0.3	4.0±0.3	0.16	3.7	T	
2	281.91360-2.007800	18:47:39.26	-02:00:28.09	0.73×0.57	57	17.1±0.4	36.1±0.6	1.05×0.87	106	0.6±0.1*	1.1±0.0	0.43	4.2	T	
3	281.92072-2.005760	18:47:40.97	-02:00:20.74	0.67×0.65	20	7.3±0.2	21.8±0.4	0.68×0.59	136	0.4±0.1*	0.8±0.0	0.05	4.1	T	
4	281.92389-2.007610	18:47:41.73	-02:00:27.40	0.64×0.45	118	22.8±1.7	26.4±1.5	0.79×0.67	100	1.4±0.2	1.6±0.1	0.48	3.4	T	
5	281.91763-2.009590	18:47:40.23	-02:00:34.51	0.56×0.53	111	3.8±0.2	4.7±0.2	-	-	-	-	0.14	-	T	
6	281.92343-2.007050	18:47:41.62	-02:00:25.37	0.64×0.61	44	10.8±1.6	17.2±1.5	-	-	-	-	0.08	-	T	
8	281.91450-2.009140	18:47:39.48	-02:00:32.92	0.54×0.47	82	3.8±0.3	4.0±0.2	-	-	-	-	0.17	-	T	
9	281.92326-2.007870	18:47:41.58	-02:00:28.34	0.55×0.46	88	6.7±1.5	6.7±1.2	0.63×0.52	72	0.5±0.2	0.5±0.1	0.14	3.2	T	
10	281.92428-2.008160	18:47:41.83	-02:00:29.38	0.82×0.62	98	6.8±1.6	12.8±1.5	-	-	-	-	0.11	-	T	
11	281.92738-2.001580	18:47:42.57	-02:00:5.690	1.10×0.94	52	0.7±0.1	3.5±0.2	-	-	-	-	0.38	-	F	
12	281.92500-2.007820	18:47:42.00	-02:00:28.16	0.63×0.51	81	4.8±1.0	5.8±0.8	-	-	-	-	0.20	-	T	
13	281.91342-2.007550	18:47:39.22	-02:00:27.17	1.09×0.93	158	2.8±0.4	7.5±0.4	-	-	-	-	0.20	-	F	
14	281.92171-2.007270	18:47:41.21	-02:00:26.17	0.73×0.64	82	1.2±0.2	2.4±0.2	-	-	-	-	0.44	-	T	
16	281.92450-2.007750	18:47:41.88	-02:00:27.88	0.81×0.76	110	2.7±1.2	5.7±1.1	-	-	-	-	0.29	-	T	
17	281.92933-2.000700	18:47:43.04	-02:00:2.500	1.05×0.66	93	0.9±0.1	2.4±0.1	-	-	-	-	0.42	-	F	
18	281.92098-2.008710	18:47:41.04	-02:00:31.37	0.81×0.69	89	0.8±0.1	1.8±0.1	-	-	-	-	0.58	-	T	
19	281.92159-2.011120	18:47:41.18	-02:00:40.02	1.15×1.12	64	0.6±0.2	2.6±0.2	-	-	-	-	0.54	-	F	
20	281.91911-2.010160	18:47:40.59	-02:00:36.56	1.19×1.04	140	0.7±0.2	2.9±0.3	-	-	-	-	0.45	-	F	
21	281.91998-2.010220	18:47:40.80	-02:00:36.80	0.77×0.72	99	0.8±0.2	1.6±0.1	-	-	-	-	0.57	-	T	
22	281.91896-2.006130	18:47:40.55	-02:00:22.07	1.05×0.73	176	0.9±0.2	2.2±0.2	-	-	-	-	0.48	-	T	
23	281.92689-1.994930	18:47:42.45	-01:59:41.75	0.59×0.50	114	2.5±0.5	2.9±0.4	-	-	-	-	0.22	-	F	
24	281.91398-2.007970	18:47:39.36	-02:00:28.70	1.10×0.75	140	1.7±0.5	4.7±0.5	-	-	-	-	0.30	-	F	
25	281.92072-2.008790	18:47:40.97	-02:00:31.64	0.76×0.64	59	0.7±0.1	1.4±0.2	-	-	-	-	0.65	-	F	
26	281.91744-2.000740	18:47:40.19	-02:00:2.670	0.64×0.40	14	0.5±0.1	0.5±0.1	-	-	-	-	1.10	-	F	
27	281.93179-2.014040	18:47:43.63	-02:00:50.56	1.00×0.79	119	0.6±0.1	1.3±0.2	-	-	-	-	0.80	-	F	
28	281.91385-2.009150	18:47:39.32	-02:00:32.94	0.61×0.51	22	1.1±0.3	1.3±0.2	-	-	-	-	0.57	-	T	
29	281.91310-2.007770	18:47:39.14	-02:00:27.97	0.69×0.57	68	1.6±0.3	2.0±0.3	-	-	-	-	0.44	-	T	
31	281.91629-2.008910	18:47:39.91	-02:00:32.08	0.58×0.50	14	0.9±0.2	1.1±0.2	-	-	-	-	0.61	-	T	
32	281.92385-2.000150	18:47:41.72	-02:00:0.550	1.28×1.05	45	0.3±0.1	1.2±0.1	-	-	-	-	1.26	-	F	
33	281.92353-2.006670	18:47:41.65	-02:00:24.01	0.77×0.59	92	2.6±1.0	4.0±0.8	-	-	-	-	0.37	-	F	
34	281.92111-2.007050	18:47:42.03	-02:00:25.38	0.70×0.65	146	1.4±0.6	2.1±0.5	-	-	-	-	0.71	-	T	
36	281.92742-1.995350	18:47:42.58	-01:59:43.27	0.90×0.60	129	1.9±0.4	4.2±0.6	-	-	-	-	0.20	-	F	
37	281.91123-2.012390	18:47:38.69	-02:00:44.62	1.47×1.27	97	1.1±0.3	1.8±0.6	-	-	-	-	0.88	-	F	
38	281.91524-2.008860	18:47:39.66	-02:00:31.91	0.57×0.52	49	0.9±0.3	0.9±0.3	-	-	-	-	0.83	-	F	
39	281.91557-2.008130	18:47:39.26	-02:00:29.28	1.06×0.88	174	1.5±0.5	3.8±0.5	-	-	-	-	0.40	-	F	
40	281.92131-2.006990	18:47:41.11	-02:00:25.15	1.36×1.00	153	0.7±0.2	2.2±0.4	-	-	-	-	0.75	-	T	
7	281.92993-2.006580	18:47:41.74	-02:00:23.68	1.49×1.05	113	4.4±1.4	21.7±2.1	1.56×1.17	120	4.4±1.6	23.3±2.0	-	-0.1	T	

F. Louvet et al.: ALMA-IMF

Notes. The coordinates are given at the J2000 Epoch. (1) Estimated from the measures at 1.3 mm. (2) Indicates if the source found by *getsf* was also found by *GExt2D* (True or False). The \* next to the uncertainty indicates that the true value is <0.05.

Table D.10: Compact sources extracted by *getsf* in W51-E, after smoothing.

n	Core name	RA [J2000]	DEC [J2000]	1.3 mm			3 mm			T [K]	Mass <sup>(1)</sup> [ $M_{\odot}$ ]	Size <sup>(1)</sup> [au]	$\alpha_{\text{BE}}^{(1)}$	$\alpha$	GExt2D
				$a \times b$ ["x"']	PA [deg]	$S^{\text{Peak}}$ [mJy.Beam <sup>-1</sup> ]	$S^{\text{int}}$ [mJy]	$a \times b$ ["x"']	PA [deg]						
2	290.93316+14.509590	19:23:43.96	14:30:34.52	1.11×0.66	177	756.4±9.4	2856.0±18.3	0.81×0.51	178	112.5±0.8	419.6±2.8	0.05	2.4	T	
4	290.93297+14.507830	19:23:43.90	14:30:28.18	0.85×0.73	6	531.1±35.3	1238.0±40.6	0.72×0.55	7	81.8±3.5	211.1±6.4	0.01	2.2	T	
8	290.93304+14.510150	19:23:43.93	14:30:36.55	1.07×0.71	167	105.7±16.5	307.1±17.0	1.00×0.68	167	13.2±1.0	34.5±1.2	0.02	2.7	F	
11	290.92284+14.504040	19:23:41.48	14:30:14.54	0.79×0.68	20	10.7±1.0	21.3±1.0	-	-	-	-	0.04	-	F	
12	290.93325+14.509130	19:23:43.99	14:30:32.86	0.89×0.81	153	39.7±9.4	84.4±8.1	0.93×0.86	170	3.9±0.7	7.4±0.6	0.05	3.0	F	
13	290.93245+14.505480	19:23:43.79	14:30:19.73	0.77×0.68	27	27.5±10.4	54.7±10.8	0.61×0.52	50	5.3±1.1	10.4±1.4	0.03	2.0	T	
14	290.93261+14.510130	19:23:43.83	14:30:36.45	0.65×0.61	174	46.9±13.1	67.9±11.2	0.67×0.58	126	6.4±0.9	9.4±0.8	0.05	2.4	F	
15	290.93151+14.509960	19:23:43.56	14:30:35.85	0.92×0.80	26	12.8±2.3	31.3±2.4	-	-	-	-	0.05	-	T	
16	290.93275+14.507360	19:23:43.86	14:30:26.49	0.91×0.48	21	64.6±30.0	70.2±30.9	0.70×0.41	35	11.5±5.4	5.0±8.6	0.06	3.2	T	
17	290.92998+14.514150	19:23:43.19	14:30:50.95	1.24×0.83	150	13.0±2.8	46.6±3.7	1.27×0.74	137	2.2±0.3	6.3±0.4	0.03	2.5	T	
19	290.93273+14.511210	19:23:43.86	14:30:40.35	0.60×0.51	11	14.8±3.7	16.4±2.8	0.72×0.49	107	1.9±0.5	1.7±0.3	0.05	2.8	T	
20	290.92557+14.511260	19:23:42.14	14:30:40.54	0.77×0.57	2	8.6±1.5	14.8±1.6	-	-	-	-	0.05	-	T	
21	290.92758+14.500600	19:23:42.62	14:30:2.150	0.64×0.57	142	3.5±0.6	5.0±0.6	-	-	-	-	0.13	-	T	
22	290.92778+14.500990	19:23:42.67	14:30:3.550	0.80×0.69	174	4.1±0.8	9.2±0.9	-	-	-	-	0.09	-	T	
26	290.92440+14.514940	19:23:41.86	14:30:53.79	1.47×1.00	168	8.2±1.9	37.3±3.0	-	-	-	-	0.04	-	F	
28	290.93199+14.508960	19:23:43.68	14:30:32.24	0.63×0.54	65	12.5±4.0	15.0±3.1	0.61×0.57	141	2.3±0.5	2.7±0.3	0.08	2.1	T	
29	290.92964+14.514940	19:23:43.11	14:30:53.78	1.02×0.93	44	5.2±1.8	17.6±2.2	-	-	-	-	0.07	-	T	
30	290.92622+14.515340	19:23:42.29	14:30:55.22	0.65×0.57	70	5.1±1.3	6.7±1.0	-	-	-	-	0.11	-	T	
31	290.92882+14.515980	19:23:42.92	14:30:57.51	0.96×0.88	29	3.9±1.3	18.1±2.3	-	-	-	-	0.06	-	F	
33	290.92667+14.501710	19:23:42.40	14:30:6.150	0.74×0.64	8	2.3±0.5	3.9±0.5	-	-	-	-	0.19	-	F	
34	290.93253+14.513110	19:23:43.81	14:30:47.20	1.08×0.94	134	4.6±1.0	15.1±1.3	-	-	-	-	0.07	-	F	
38	290.93495+14.507830	19:23:44.39	14:30:28.20	0.84×0.71	48	6.6±1.9	13.8±1.9	-	-	-	-	0.08	-	T	
39	290.93426+14.508900	19:23:44.22	14:30:32.05	1.02×0.89	78	9.1±3.6	25.3±3.7	-	-	-	-	0.08	-	T	
1	290.93296+14.509590	19:23:43.91	14:30:34.53	1.04×0.64	180	459.2±15.1	1171.0±17.4	0.58×0.54	18	557.8±1.0	1541.6±2.4	-	-	T	
3	290.92446+14.515760	19:23:41.87	14:30:56.72	0.66×0.55	162	8.5±1.4	12.1±1.4	0.61×0.53	72	30.4±0.2	41.6±0.2	-	-	T	
5	290.93281+14.509990	19:23:43.88	14:30:35.95	1.02×0.76	130	188.1±15.4	485.0±14.7	0.75×0.57	132	30.6±1.1	103.6±1.8	-	-	T	
6	290.94244+14.496350	19:23:46.19	14:29:46.84	0.70×0.64	26	14.4±4.2	24.4±4.3	0.56×0.51	74	11.6±0.5	20.9±0.8	-	-	T	
9	290.94268+14.496430	19:23:46.24	14:29:47.14	0.86×0.71	13	23.1±3.7	62.0±4.9	0.78×0.46	16	7.0±0.3	16.0±0.6	-	-	T	
10	290.93245+14.506210	19:23:43.79	14:30:22.34	0.69×0.65	80	40.8±13.1	61.6±10.5	0.65×0.57	72	9.4±1.3	14.3±1.2	-	-	T	
18	290.92666+14.502200	19:23:42.40	14:30:7.900	0.72×0.64	68	2.7±0.3	4.3±0.3	-	-	-	-	-	-	T	
27	290.93346+14.507530	19:23:44.03	14:30:27.12	0.82×0.56	164	20.7±10.3	34.4±10.3	0.56×0.45	165	4.4±0.8	7.6±1.2	-	-	T	

**Notes.** The coordinates are given at the J2000 Epoch. (1) Estimated from the measures at 1.3 mm. (2) Indicates if the source found by *getsf* was also found by GExt2D (True or False). The \* next to the uncertainty indicates that the true value is <0.05.

Table D.11: Compact sources extracted by *getsf* in G351, after smoothing.

n	Core name	RA [J2000]	DEC [J2000]	1.3 mm			3 mm			T [K]	Mass <sup>(1)</sup> [ $M_{\odot}$ ]	Size <sup>(1)</sup> [au]	$\alpha_{\text{BE}}^{(1)}$	$\alpha$	GExt2D
				$a \times b$ ["x'"]	PA [deg]	$S^{\text{Peak}}$ [mJy.Beam <sup>-1</sup> ]	$S^{\text{int}}$ [mJy]	$a \times b$ ["x'"]	PA [deg]						
1	261.67725-36.15480	17:26:42.54	-36:09:17.28	2.40x1.79	91	743.6±13.6	1817.0±18.6	2.24x1.68	98	43.8±3.8	92.7±4.3	3952	0.07	3.6	T
2	261.67677-36.15517	17:26:42.43	-36:09:18.62	2.88x2.22	126	824.7±23.1	2877.0±34.7	3.13x2.46	120	59.3±1.1	191.7±1.6	4836	0.05	3.3	T
4	261.67616-36.15493	17:26:42.28	-36:09:17.76	1.62x1.33	78	431.4±31.0	490.6±24.5	1.71x1.54	79	55.2±2.0	55.8±1.3	2840	0.03	2.6	T
5	261.67837-36.15570	17:26:42.81	-36:09:20.52	1.56x1.46	122	179.9±32.2	207.4±25.4	1.51x1.42	37	13.1±4.5	14.2±3.7	2982	0.48	3.3	T
6	261.67786-36.15512	17:26:42.69	-36:09:18.45	2.30x2.05	45	287.7±36.4	639.6±34.0	-	-	-	-	4264	0.05	-	T
7	261.67881-36.15535	17:26:42.91	-36:09:19.25	1.84x1.72	99	105.4±32.5	157.4±25.6	1.82x1.36	72	4.9±2.6	7.1±2.6	3520	0.15	3.8	F
8	261.67848-36.14315	17:26:42.84	-36:08:35.35	1.42x1.28	61	9.0±0.8	9.1±0.6	-	-	-	-	2656	0.55	-	T
10	261.68823-36.15028	17:26:45.18	-36:09:0.990	1.76x1.51	149	10.1±0.9	16.7±1.1	-	-	-	-	3180	0.38	-	T
11	261.67533-36.15879	17:26:42.08	-36:09:31.63	1.88x1.62	84	13.5±2.3	19.8±1.8	-	-	-	-	3400	0.59	-	T
12	261.67434-36.15262	17:26:41.84	-36:09:9.430	1.76x1.55	111	15.9±3.5	21.2±2.7	-	-	-	-	3232	0.60	-	T
13	261.68787-36.15539	17:26:45.09	-36:09:19.42	1.64x1.48	155	8.6±1.4	10.1±1.1	-	-	-	-	3064	0.71	-	T
14	261.68010-36.15443	17:26:43.22	-36:09:15.94	2.04x1.68	92	32.1±10.6	48.0±8.2	-	-	-	-	3576	0.38	-	T
15	261.67579-36.15700	17:26:42.19	-36:09:25.21	1.97x1.67	141	17.4±6.3	25.7±4.9	-	-	-	-	3532	0.57	-	T
16	261.67348-36.14667	17:26:41.63	-36:08:48.00	1.78x1.68	153	7.0±1.6	10.0±1.2	-	-	-	-	3424	0.77	-	T
18	261.67802-36.15067	17:26:42.72	-36:09:2.420	1.95x1.68	82	11.6±3.5	18.1±2.7	-	-	-	-	3532	0.68	-	T
19	261.68203-36.15181	17:26:43.69	-36:09:6.510	1.95x1.72	65	16.1±5.7	26.8±4.8	-	-	-	-	3578	0.46	-	T
20	261.67846-36.15333	17:26:42.83	-36:09:11.97	2.05x1.42	180	34.9±12.1	47.4±9.3	-	-	-	-	3208	0.38	-	T
23	261.68338-36.15449	17:26:44.01	-36:09:16.18	1.99x1.73	89	8.5±4.2	14.1±3.3	-	-	-	-	3622	0.96	-	T
3	261.68195-36.15453	17:26:43.67	-36:09:16.32	2.14x1.74	138	18.1±7.3	32.7±6.5	3.94x3.03	65	40.8±0.7	67.5±0.5	3736	-	-0.9	T

**Notes.** The coordinates are given at the J2000 Epoch. (1) Estimated from the measures at 1.3 mm. (2) Indicates if the source found by *getsf* was also found by GExt2D (True or False). The \* next to the uncertainty indicates that the true value is <0.05.



Table D.13: Continuation of Table D.12

n	Core name	RA	DEC	1.3 mm			3 mm			T	Mass <sup>(1)</sup>	Size <sup>(1)</sup>	$\alpha_{\text{BE}}^{(1)}$	$\alpha$	GExt2D <sup>(2)</sup>
				$a \times b$	PA	$S^{\text{Peak}}$	$S^{\text{int}}$	$a \times b$	PA						
44	262.60301-34.69564	17:30:24.72	-34:41:44.31	1.76×1.55	97	5.9±1.9	6.9±1.9	-	24±06	0.4±0.1	3236	0.83	-	T	
45	262.61430-34.69094	17:30:27.43	-34:41:27.38	4.09×3.38	67	5.4±1.2	36.5±2.2	-	23±06	2.1±0.1	7204	0.33	-	T	
46	262.61876-34.69124	17:30:28.50	-34:41:28.46	2.76×2.12	53	5.4±2.1	12.3±2.8	-	23±06	0.7±0.2	4626	0.62	-	F	
47	262.61785-34.69199	17:30:28.28	-34:41:31.18	3.17×2.90	168	6.0±2.6	22.4±3.5	-	24±06	1.3±0.2	5982	0.45	-	F	
1	262.60906-34.69597	17:30:26.17	-34:41:45.49	2.12×1.49	83	136.7±21.5	240.2±21.8	2.18×1.55	82	176.9±3.7	330.6±4.5	-	-0.4	F	

**Notes.** The coordinates are given at the J2000 Epoch. (1) Estimated from the measures at 1.3 mm. (2) Indicates if the source found by *getsf* was also found by *GExt2D* (True or False). The \* next to the uncertainty indicates that the true value is <0.05.

Table D.14: Compact sources extracted by *getsf* in G008, after smoothing.

n	Core name	RA [IRCS]	DEC [ICRS]	1.3 mm				3 mm				T [K]	Mass <sup>(1)</sup> [ $M_{\odot}$ ]	Size <sup>(1)</sup> [au]	$\alpha_{\text{BE}}^{(1)}$	$\alpha$	GExt2D
				$a \times b$ ["x'"]	PA [deg]	$S^{\text{Peak}}$ [mJy.Beam <sup>-1</sup> ]	$S^{\text{int}}$ [mJy]	$a \times b$ ["x'"]	PA [deg]	$S^{\text{Peak}}$ [mJy.Beam <sup>-1</sup> ]	$S^{\text{int}}$ [mJy]						
2	271.59883-21.61959	18:06:23.48	-21:37:10.53	0.96x0.87	92	70.4±2.1	98.5±2.6	1.06x0.98	93	5.4±0.2	7.5±0.2	100±50	3.3±0.1	3044	0.36	3.1	T
3	271.57961-21.62503	18:06:19.11	-21:37:30.13	0.90x0.79	71	71.9±8.4	76.7±6.7	0.91x0.81	52	7.3±1.0	7.6±0.7	34±09	8.7±0.7	2804	0.04	2.8	T
4	271.58876-21.62371	18:06:19.38	-21:37:25.35	1.42x1.36	168	15.4±1.0	41.7±1.2	-	-	-	-	28±07	5.7±0.2	4682	0.09	-	T
5	271.57853-21.62223	18:06:18.85	-21:37:20.03	1.06x0.91	95	19.8±1.4	29.6±1.3	1.13x0.84	64	1.3±0.2	1.4±0.2	24±06	4.9±0.2	3268	0.07	3.7	T
6	271.59805-21.61989	18:06:23.53	-21:37:11.60	1.13x1.11	4	17.8±2.1	29.1±1.6	-	-	-	-	32±08	3.4±0.2	3788	0.14	-	T
7	271.58801-21.62520	18:06:19.20	-21:37:30.71	1.35x0.96	92	41.2±9.3	73.2±9.6	-	-	-	-	33±08	8.3±1.1	3652	0.06	-	F
8	271.59542-21.62039	18:06:22.90	-21:37:13.41	0.97x0.73	80	5.8±0.4	6.3±0.3	-	-	-	-	25±06	1.0±0.1*	2732	0.30	-	T
9	271.59851-21.61984	18:06:23.64	-21:37:11.43	1.09x0.85	99	12.5±2.5	16.3±2.0	-	-	-	-	30±08	2.1±0.3	3132	0.18	-	T
10	271.57744-21.62712	18:06:18.58	-21:37:37.63	1.62x1.30	153	13.6±2.5	41.5±3.2	-	-	-	-	32±08	4.9±0.4	4748	0.12	-	T
11	271.57915-21.62477	18:06:19.00	-21:37:29.18	1.14x1.03	156	19.2±6.9	32.3±6.8	-	-	-	-	32±08	3.8±0.8	3634	0.12	-	T
12	271.57965-21.62087	18:06:19.12	-21:37:15.14	1.18x0.98	28	5.1±0.7	8.7±0.6	-	-	-	-	21±05	1.7±0.1	3552	0.18	-	T
13	271.57815-21.62226	18:06:18.76	-21:37:20.13	0.95x0.81	94	9.8±1.6	11.4±1.3	-	-	-	-	24±06	1.9±0.2	2910	0.15	-	T
14	271.57980-21.62398	18:06:19.15	-21:37:26.33	1.24x1.06	1	13.8±4.1	23.2±3.3	-	-	-	-	29±07	3.0±0.4	3788	0.15	-	T
15	271.57859-21.62711	18:06:18.86	-21:37:37.59	1.25x1.15	148	11.2±3.1	21.8±3.0	-	-	-	-	31±08	2.6±0.4	4014	0.20	-	T
16	271.59384-21.61827	18:06:22.52	-21:37:5.780	1.25x1.05	77	3.6±0.5	6.2±0.5	-	-	-	-	20±05	1.3±0.1	3792	0.24	-	T
17	271.57975-21.62189	18:06:19.14	-21:37:18.82	1.04x0.83	91	8.0±1.6	9.8±1.2	-	-	-	-	22±06	1.8±0.2	3050	0.16	-	T
19	271.59161-21.61907	18:06:21.99	-21:37:8.650	2.16x1.40	52	1.9±0.3	3.5±0.5	-	-	-	-	19±05	0.8±0.1	5496	0.55	-	F
21	271.59775-21.61907	18:06:23.46	-21:37:8.650	1.62x1.21	4	4.5±2.0	10.6±1.8	-	-	-	-	30±08	1.3±0.2	4536	0.42	-	F
22	271.59798-21.62025	18:06:23.52	-21:37:12.89	1.47x1.41	31	6.0±1.3	13.0±1.5	-	-	-	-	30±08	1.6±0.2	4850	0.36	-	F
1	271.57924-21.62562	18:06:19.02	-21:37:32.21	1.37x1.32	176	256.2±8.7	733.1±12.1	1.48x1.34	106	185.9±1.5	620.3±2.9	-	-	4548	-	0.2	F

A&amp;A proofs: manuscript no. CMF-in-ALMA-IMF

**Notes.** The coordinates are given at the J2000 Epoch. (1) Estimated from the measures at 1.3 mm. (2) Indicates if the source found by *getsf* was also found by GExt2D (True or False). The \* next to the uncertainty indicates that the true value is <0.05.



Table D.16: Continuation of Table D.15

n	Core name	RA	DEC	1.3 mm			3 mm			T	Mass <sup>(1)</sup>	Size <sup>(1)</sup>	$\alpha_{BE}^{(1)}$	$\alpha$	GExt2D <sup>(2)</sup>
				$a \times b$	PA	$S^{Peak}$	$S^{int}$	$a \times b$	PA						
62	272.61455-19.92407	18:10:27.49	-19:55:26.65	1.04×0.83	156	1.3±0.5	2.9±0.6	-	-	25±06	0.9±0.2	4432	0.49	-	T
1	272.61942-19.93045	18:10:28.66	-19:55:49.63	1.51×0.94	128	448.8±9.5	2115.0±17.4	2603.5±10.7	498.4±4.5	-	-	5444	-	-0.3	T
10	272.62004-19.93072	18:10:28.81	-19:55:50.59	1.17×0.87	109	30.9±15.0	83.9±14.7	72.4±5.6	26.5±6.0	-	-	4768	-	0.2	T
12	272.62021-19.93024	18:10:28.85	-19:55:48.88	0.79×0.71	161	15.7±4.7	20.8±4.0	30.8±3.3	20.7±4.1	-	-	3644	-	-0.5	T
13	272.61756-19.92881	18:10:28.21	-19:55:43.73	1.59×1.01	44	7.9±1.6	35.3±2.2	38.3±1.0	8.4±0.6	-	-	5824	-	-0.1	T
15	272.62009-19.93089	18:10:28.82	-19:55:51.21	1.02×0.87	107	29.8±11.9	67.7±10.5	21.5±3.8	8.7±3.5	-	-	4558	-	1.4	T
23	272.61925-19.92999	18:10:28.62	-19:55:47.95	0.81×0.73	159	18.4±8.7	25.9±6.7	22.9±3.3	18.8±5.5	-	-	3726	-	0.2	T
28	272.61975-19.93094	18:10:28.74	-19:55:51.37	0.87×0.78	54	22.4±9.6	39.7±7.4	22.4±3.6	12.3±5.7	-	-	4000	-	0.7	T
41	272.61945-19.93242	18:10:28.67	-19:55:56.72	0.81×0.74	50	2.2±0.9	3.5±0.7	3.8±0.8	2.2±0.9	-	-	3772	-	-0.1	T

**Notes.** The coordinates are given at the J2000 Epoch. (1) Estimated from the measures at 1.3 mm. (2) Indicates if the source found by *getsf* was also found by *GExt2D* (True or False). The \* next to the uncertainty indicates that the true value is <0.05.



Table D.17: Compact sources extracted by *getsf* in G012, after smoothing.

n	Core name	RA [J2000]	DEC [J2000]	1.3 mm			3 mm			T [K]	Mass <sup>(1)</sup> [ $M_{\odot}$ ]	Size <sup>(1)</sup> [au]	$\alpha_{\text{BE}}^{(1)}$	$\alpha$	GExT2D	
				$a \times b$ ["x"]	PA [deg]	$S^{\text{Peak}}$ [mJy.Beam <sup>-1</sup> ]	$S^{\text{int}}$ [mJy]	$a \times b$ ["x"]	PA [deg]							$S^{\text{Peak}}$ [mJy.Beam <sup>-1</sup> ]
1	273.54933-17.92568	18:14:11.84	-17:55:32.45	1.60x1.17	57	243.9±4.5	363.3±4.2	1.96x1.61	59	27.5±0.7	25.4±0.4	6.2±0.1	3122	0.20	3.2	T
3	273.55735-17.92251	18:14:13.76	-17:55:21.04	1.84x1.52	8	135.6±4.8	315.4±6.2	1.57x1.37	3	11.8±4.8	13.3±5.8	5.3±0.1	3898	0.29	3.9	T
4	273.54443-17.93753	18:14:10.66	-17:56:15.12	1.41x1.09	92	37.6±1.7	43.7±1.7	1.59x1.31	77	3.4±0.2	2.7±0.1	3.1±0.1	2850	0.10	3.4	T
5	273.54822-17.94582	18:14:11.57	-17:56:44.95	1.44x1.14	89	57.6±2.7	74.9±2.4	1.68x1.27	74	6.8±0.3	5.7±0.2	5.9±0.2	2956	0.05	3.1	T
6	273.55315-17.92082	18:14:12.76	-17:55:14.95	1.60x1.11	54	46.2±2.1	77.2±2.6	2.32x1.92	131	5.5±1.4	3.8±0.5	4.4±0.1	3004	0.09	3.7	T
8	273.54862-17.92621	18:14:11.67	-17:55:34.36	2.35x1.54	69	95.5±7.9	216.8±8.0	2.46x1.75	70	12.3±1.2	20.3±0.9	3.6±0.1	4250	0.47	2.9	T
9	273.55574-17.91511	18:14:13.38	-17:54:54.39	1.46x1.40	26	22.2±1.3	34.0±1.3	1.66x1.46	48	3.6±0.3	4.1±0.2	2.4±0.1	3404	0.16	2.6	T
10	273.55421-17.91416	18:14:13.01	-17:54:50.99	1.53x1.09	73	19.8±0.8	25.0±0.7	1.82x1.39	77	2.5±0.3	2.3±0.2	1.9±0.1	2932	0.16	2.9	T
11	273.55477-17.92790	18:14:13.14	-17:55:40.44	1.72x1.42	77	117.2±30.2	222.2±31.9	1.75x1.69	46	15.5±13.8	18.4±8.7	3.7±0.5	3632	0.39	3.0	T
12	273.54449-17.93029	18:14:10.68	-17:55:49.04	1.50x1.37	72	23.9±2.2	36.4±2.0	1.78x1.55	58	2.0±0.4	1.9±0.3	2.3±0.1	3386	0.17	3.6	T
13	273.54844-17.94125	18:14:11.62	-17:56:28.49	1.75x1.54	17	11.0±0.6	23.2±0.6	-	-	-	-	1.7±0.1*	3860	0.24	-	T
16	273.55268-17.92857	18:14:12.64	-17:55:42.84	1.35x1.07	67	22.7±1.8	25.2±1.4	1.80x1.60	134	3.8±1.2	2.5±0.5	1.2±0.1	2772	0.36	2.8	T
19	273.55616-17.92129	18:14:13.48	-17:55:16.65	1.78x1.46	176	30.4±4.0	61.3±4.2	-	-	-	-	3.2±0.2	3744	0.17	-	T
20	273.55693-17.92331	18:14:13.66	-17:55:23.91	1.82x1.27	41	26.1±4.8	37.8±3.7	-	-	-	-	1.9±0.2	3434	0.25	-	T
22	273.56610-17.92342	18:14:15.86	-17:55:24.31	1.56x1.18	54	18.4±2.0	24.5±1.5	1.66x1.36	65	2.3±0.3	2.1±0.2	1.5±0.1	3116	0.26	3.0	T
23	273.54644-17.92862	18:14:11.15	-17:55:43.03	1.68x1.35	61	29.2±6.4	43.6±5.0	-	-	-	-	2.8±0.3	3488	0.15	-	T
24	273.56897-17.93902	18:14:16.55	-17:56:20.47	2.10x1.31	68	7.3±0.6	14.7±0.6	-	-	-	-	1.1±0.1*	3678	0.33	-	T
25	273.56902-17.92472	18:14:16.57	-17:55:29.00	1.85x1.23	90	11.9±1.2	21.0±1.3	-	-	-	-	1.4±0.1	3384	0.26	-	T
26	273.54200-17.93274	18:14:10.08	-17:55:57.88	1.98x1.30	57	22.7±3.1	40.3±2.8	2.14x1.57	58	2.8±0.4	3.3±0.2	2.7±0.2	3582	0.15	3.1	T
27	273.55616-17.93485	18:14:13.48	-17:56:5.460	1.97x1.82	171	12.4±1.9	30.7±2.1	-	-	-	-	1.8±0.1	4480	0.33	-	T
29	273.55167-17.91895	18:14:12.40	-17:55:8.220	1.91x1.67	112	11.3±1.9	26.6±2.1	-	-	-	-	1.7±0.1	4188	0.29	-	T
30	273.55761-17.93118	18:14:13.83	-17:55:52.23	1.68x1.49	16	36.5±7.6	57.8±6.2	-	-	-	-	2.9±0.3	3718	0.19	2.8	T
31	273.56769-17.92049	18:14:16.24	-17:55:13.76	2.18x1.55	158	8.0±0.9	21.0±1.2	2.66x1.61	1	4.9±7.5	5.6±3.4	1.5±0.1	4168	0.31	-	T
32	273.54704-17.93339	18:14:11.29	-17:56:0.210	1.60x1.32	29	10.8±1.6	17.8±1.5	-	-	-	-	1.2±0.1	3378	0.33	-	T
33	273.55816-17.92523	18:14:13.96	-17:55:30.84	2.16x1.68	25	25.7±5.0	61.7±4.8	-	-	-	-	2.9±0.2	4384	0.23	-	T
34	273.54651-17.92768	18:14:11.16	-17:55:39.65	1.63x1.42	37	20.5±6.1	31.7±4.7	-	-	-	-	2.0±0.3	3572	0.21	-	T
39	273.56654-17.92283	18:14:15.97	-17:55:22.18	1.80x1.36	50	14.0±1.9	24.0±1.6	-	-	-	-	1.5±0.1	3580	0.18	-	T
40	273.54579-17.92847	18:14:10.99	-17:55:42.48	2.12x1.76	40	20.4±5.7	47.6±5.0	-	-	-	-	3.0±0.3	4490	0.18	-	T
41	273.56623-17.92567	18:14:15.89	-17:55:32.43	1.69x1.47	48	7.3±1.1	12.7±1.0	-	-	-	-	0.8±0.1	3694	0.61	-	T
42	273.56481-17.92624	18:14:15.55	-17:55:34.48	2.01x1.65	98	7.1±1.0	15.7±1.0	-	-	-	-	0.9±0.1	4232	0.63	-	T
44	273.57149-17.92495	18:14:17.16	-17:55:29.81	1.37x1.00	73	9.8±1.4	9.5±1.2	-	-	-	-	0.7±0.1	2674	0.37	-	T
45	273.55778-17.91824	18:14:13.39	-17:55:5.660	2.76x2.44	7	5.1±0.9	23.8±1.2	-	-	-	-	1.5±0.1	6092	0.51	-	T
46	273.55792-17.93067	18:14:13.90	-17:55:50.39	1.83x1.74	45	33.9±9.1	75.9±9.8	-	-	-	-	3.7±0.5	4256	0.17	-	T
47	273.54900-17.92729	18:14:11.52	-17:55:38.25	2.22x1.72	44	15.9±6.0	37.1±6.2	-	-	-	-	2.3±0.4	4500	0.24	-	T
51	273.54880-17.92897	18:14:10.99	-17:55:44.30	1.75x1.43	77	18.6±5.4	28.0±4.2	-	-	-	-	1.8±0.3	3674	0.24	-	T
52	273.55338-17.92285	18:14:12.09	-17:55:22.26	1.60x1.12	67	11.5±2.5	14.9±1.9	-	-	-	-	0.9±0.1	3034	0.46	-	T
53	273.54637-17.94216	18:14:11.13	-17:56:31.77	1.84x1.37	34	7.2±1.7	12.6±1.5	-	-	-	-	0.9±0.1	3634	0.40	-	T
55	273.55816-17.93570	18:14:13.24	-17:56:8.540	2.55x1.99	136	5.5±1.4	17.8±3.0	-	-	-	-	1.1±0.2	5178	0.57	-	T
57	273.56445-17.91871	18:14:14.75	-17:55:7.350	2.34x1.89	61	9.7±3.1	30.8±3.8	-	-	-	-	1.7±0.2	4870	0.39	-	T
58	273.55554-17.91790	18:14:14.29	-17:55:4.420	1.59x1.45	158	7.8±2.2	12.0±1.7	-	-	-	-	0.7±0.1	3582	0.69	-	T
59	273.55298-17.93749	18:14:12.71	-17:56:14.98	1.70x1.46	117	4.4±1.1	7.8±1.0	-	-	-	-	0.6±0.1	3696	0.73	-	T

F. Louvet et al.: ALMA-IMF

Table D.18: Continuation of Table D.17

n	Core name	1.3 mm			3 mm			T	Mass <sup>(1)</sup>	Size <sup>(1)</sup>	$\alpha_{BE}^{(1)}$	$\alpha$	GExt2D <sup>(2)</sup>				
		RA	DEC	$a \times b$	PA	$S_{Peak}$	$S_{int}$							$a \times b$	PA	$S_{Peak}$	$S_{int}$
61	273.54755-17.92664	18:14:11.41	-17:55:35.90	1.69×1.04	60	16.5±7.7	19.6±6.0	-	-	-	29±07	1.2±0.4	2938	0.28	-	T	
65	273.55977-17.91869	18:14:14.34	-17:55:7.270	1.70×1.52	51	6.9±2.7	12.6±2.7	-	-	-	34±09	0.7±0.1	3792	0.75	-	T	
66	273.54772-17.93073	18:14:11.45	-17:55:50.62	2.13×1.44	75	5.0±1.3	11.4±1.7	-	-	-	30±08	0.7±0.1	3934	0.68	-	T	
2	273.55762-17.92916	18:14:13.83	-17:55:44.97	2.74×1.40	95	335.2±43.5	737.2±48.2	2.95×1.62	92	582.1±54.0	1054.4±47.6	-	-	4202	-	-0.4	T
7	273.55950-17.92033	18:14:14.28	-17:55:13.20	2.98×2.37	107	47.8±6.5	216.1±8.5	3.07×2.24	103	69.0±15.1	205.9±16.3	-	-	6134	-	0.1	T
17	273.55809-17.93286	18:14:13.94	-17:55:58.29	3.15×2.18	120	18.5±6.4	86.4±9.6	3.40×2.74	121	27.3±8.0	87.4±7.5	-	-	5918	-	-0.0	T
21	273.56210-17.93023	18:14:14.91	-17:55:48.82	3.93×2.70	112	20.9±4.6	149.3±9.6	3.93×2.45	109	36.3±13.6	206.2±26.2	-	-	7342	-	-0.4	T
28	273.55880-17.92769	18:14:14.11	-17:55:39.67	1.96×1.48	85	73.8±28.5	147.8±26.6	2.46×2.38	125	24.8±29.0	31.1±11.3	-	-	3904	-	1.9	T
35	273.56146-17.92945	18:14:14.75	-17:55:46.01	2.36×1.90	120	28.0±5.8	86.0±6.5	-	-	-	-	-	-	4898	-	-	T
36	273.55694-17.92390	18:14:13.67	-17:55:26.04	1.71×1.45	68	21.1±4.4	35.3±3.6	-	-	-	-	-	-	3682	-	-	T
37	273.55935-17.92094	18:14:14.24	-17:55:15.40	1.39×1.27	43	17.5±6.0	22.0±4.6	1.68×1.54	52	34.0±13.9	30.6±7.3	-	-	3134	-	-0.4	T
43	273.55598-17.92725	18:14:13.43	-17:55:38.09	1.88×1.26	88	66.0±30.4	95.9±23.5	-	-	-	-	-	-	3448	-	-	T
49	273.56052-17.93077	18:14:14.52	-17:55:50.78	1.80×1.59	24	16.6±6.5	33.4±6.5	1.90×1.57	5	26.2±10.6	35.3±7.9	-	-	3986	-	-0.1	T
50	273.55856-17.93226	18:14:14.05	-17:55:56.14	1.55×1.36	135	13.9±4.8	19.8±3.7	1.65×1.08	125	16.1±6.0	20.0±5.5	-	-	3402	-	-0.0	T
56	273.56290-17.93361	18:14:15.10	-17:56:1.000	2.02×1.77	74	7.0±1.8	16.0±1.7	2.06×1.58	80	5.8±3.3	9.8±2.8	-	-	4440	-	0.6	T
62	273.55339-17.92803	18:14:12.81	-17:55:40.92	2.13×1.63	94	10.8±4.4	22.9±4.0	-	-	-	-	-	-	4280	-	-	T

A&amp;A proofs: manuscript no. CMF-in-ALMA-IMF

**Notes.** The coordinates are given at the J2000 Epoch. (1) Estimated from the measures at 1.3 mm. (2) Indicates if the source found by *getsf* was also found by *GExt2D* (True or False). The \* next to the uncertainty indicates that the true value is <0.05.

Table D.19: Compact sources extracted by *getsf* in G333, after smoothing.

n	Core name	RA [J2000]	DEC [J2000]	1.3 mm				3 mm				T [K]	Mass <sup>(1)</sup> [ $M_{\odot}$ ]	Size <sup>(1)</sup> [au]	$\alpha_{\text{BE}}^{(1)}$	$\alpha$	GExT2D
				$a \times b$ ["x"]	PA [deg]	$S^{\text{Peak}}$ [mJy.Beam <sup>-1</sup> ]	$S^{\text{int}}$ [mJy]	$a \times b$ ["x"]	PA [deg]	$S^{\text{Peak}}$ [mJy.Beam <sup>-1</sup> ]	$S^{\text{int}}$ [mJy]						
1	245.54680-50.09881	16:22:11.23	-50:05:55.71	1.41x0.90	67	117.0x3.4	350.6x5.1	1.09x0.94	147	12.4x3.8	15.7x6.8	49x12	42.5x0.5	4402	0.02	3.8	T
2	245.53562-50.10481	16:22:8.550	-50:06:17.33	0.94x0.75	67	50.6x2.1	91.3x2.3	1.22x0.77	51	2.9x2.2	2.8x1.7	41x10	13.0x0.3	3392	0.04	4.3	T
3	245.52839-50.10507	16:22:6.810	-50:06:18.24	0.83x0.79	88	23.3x2.1	37.1x2.1	0.81x0.71	110	1.8x0.2	2.7x0.2	36x09	5.8x0.3	3368	0.08	3.2	T
4	245.54606-50.09905	16:22:11.05	-50:05:56.59	0.85x0.63	47	63.4x4.7	91.7x6.5	-	-	-	-	100x50	4.8x0.3	2930	0.25	-	T
5	245.52853-50.10455	16:22:6.850	-50:06:16.39	0.74x0.71	8	24.8x2.9	29.3x2.2	0.72x0.68	51	2.4x0.3	2.9x0.2	35x09	4.7x0.3	3020	0.09	2.8	T
7	245.53700-50.10280	16:22:8.880	-50:06:10.07	1.30x0.96	24	46.0x4.5	138.4x5.8	-	-	-	-	45x11	17.1x0.7	4462	0.05	-	T
8	245.52830-50.10681	16:22:6.790	-50:06:24.53	1.00x0.77	50	10.6x0.8	24.5x1.2	-	-	-	-	31x08	4.5x0.2	3528	0.10	-	T
11	245.53570-50.10339	16:22:8.570	-50:06:12.20	1.33x1.13	36	31.6x4.6	100.7x5.7	1.54x1.07	174	4.9x2.9	14.2x3.2	100x50	5.2x0.3	5016	0.39	2.4	T
14	245.52713-50.10569	16:22:6.510	-50:06:20.48	1.01x0.77	18	9.6x1.0	18.3x1.1	-	-	-	-	31x08	3.4x0.2	3550	0.13	-	T
18	245.52963-50.10644	16:22:7.110	-50:06:23.19	0.69x0.60	43	8.2x1.3	8.0x1.0	0.74x0.56	180	0.8x0.1	0.9x0.1	31x08	1.5x0.2	2638	0.22	2.7	T
19	245.52704-50.10895	16:22:6.490	-50:06:32.20	1.25x1.07	151	3.1x0.3	9.3x0.5	-	-	-	-	27x07	2.0x0.1	4748	0.26	-	T
21	245.53118-50.10427	16:22:7.480	-50:06:15.38	1.17x1.04	16	6.1x0.9	15.4x1.0	-	-	-	-	35x09	2.4x0.2	4532	0.27	-	T
22	245.51702-50.10900	16:22:4.090	-50:06:32.39	0.86x0.71	54	5.4x1.0	7.9x1.0	-	-	-	-	26x07	1.8x0.2	3164	0.19	-	T
23	245.54742-50.09600	16:22:11.38	-50:05:45.59	1.08x0.82	150	8.9x1.3	17.1x1.4	-	-	-	-	35x09	2.7x0.2	3760	0.20	-	T
25	245.51746-50.10830	16:22:4.190	-50:06:29.87	0.96x0.82	129	4.9x1.5	8.3x1.3	-	-	-	-	27x07	1.6x0.2	2796	0.19	-	T
26	245.53535-50.10417	16:22:8.480	-50:06:15.03	0.95x0.75	148	15.7x3.3	27.8x3.3	-	-	-	-	40x10	3.8x0.5	3404	0.14	-	T
28	245.55083-50.09141	16:22:12.20	-50:05:29.08	1.34x0.90	169	1.2x0.2	2.9x0.2	-	-	-	-	31x08	0.5x0.1*	4314	1.03	-	F
30	245.54753-50.09897	16:22:11.41	-50:05:56.29	1.68x1.32	117	15.4x3.0	63.6x3.4	-	-	-	-	45x11	7.7x0.4	6006	0.14	-	F
31	245.54798-50.09933	16:22:11.52	-50:05:57.59	0.97x0.91	95	11.7x3.3	22.5x3.2	-	-	-	-	41x10	3.0x0.4	3892	0.22	-	T
33	245.54969-50.09216	16:22:11.92	-50:05:31.79	1.70x1.11	168	1.7x0.2	6.8x0.3	-	-	-	-	31x08	1.2x0.1	5382	0.56	-	F
35	245.51746-50.10830	16:22:4.190	-50:06:29.87	0.96x0.82	129	4.9x1.5	8.3x1.3	-	-	-	-	27x07	1.8x0.3	3614	0.22	-	T
37	245.53080-50.10345	16:22:7.390	-50:06:12.43	1.29x1.16	132	3.8x0.7	10.8x0.9	-	-	-	-	34x09	1.8x0.1	5048	0.39	-	T
43	245.52230-50.11055	16:22:5.350	-50:06:37.97	0.81x0.69	113	0.9x0.1	1.2x0.1	-	-	-	-	25x06	0.3x0.1*	3066	1.12	-	F
44	245.51651-50.10989	16:22:3.960	-50:06:35.59	1.57x1.26	44	2.3x0.5	9.0x0.7	-	-	-	-	25x06	2.1x0.2	5684	0.27	-	F
45	245.54930-50.09849	16:22:11.83	-50:05:54.55	1.45x1.03	48	8.2x2.3	25.4x2.9	-	-	-	-	38x10	3.7x0.4	4842	0.20	-	T
46	245.55307-50.08862	16:22:12.74	-50:05:19.04	1.24x1.08	42	1.1x0.2	3.0x0.2	-	-	-	-	28x07	0.6x0.1*	4754	0.85	-	F
47	245.54963-50.09886	16:22:11.91	-50:05:55.88	1.06x0.99	26	4.4x2.1	9.4x2.0	-	-	-	-	37x09	1.4x0.3	4272	0.45	-	T
49	245.54719-50.09822	16:22:11.33	-50:05:53.58	1.33x0.94	38	8.1x2.7	19.5x2.8	-	-	-	-	43x11	2.5x0.4	4420	0.31	-	T
50	245.54262-50.10605	16:22:10.23	-50:06:21.78	1.98x1.11	176	5.7x1.6	21.3x2.4	-	-	-	-	34x09	3.5x0.4	5666	0.23	-	T
61	245.55158-50.09201	16:22:12.38	-50:05:31.22	1.23x1.03	3	1.4x0.3	3.3x0.3	-	-	-	-	31x08	0.6x0.1	4572	0.96	-	F
62	245.53580-50.10099	16:22:8.590	-50:06:3.560	1.21x0.97	74	27.4x11.4	62.1x10.8	-	-	-	-	44x11	7.8x1.3	4372	0.10	-	T
63	245.53521-50.08610	16:22:7.970	-50:05:9.950	1.86x1.14	92	1.1x0.3	3.8x0.4	-	-	-	-	26x07	0.9x0.1	5642	0.68	-	F
65	245.53641-50.10819	16:22:9.460	-50:06:29.48	1.17x0.90	113	1.5x0.3	3.3x0.3	-	-	-	-	33x08	0.6x0.1	4140	1.00	-	F
66	245.5224-50.10608	16:22:7.020	-50:06:21.91	1.06x0.67	80	2.9x1.1	2.7x1.2	-	-	-	-	31x08	0.5x0.2	3286	0.84	-	T
71	245.55546-50.10937	16:22:13.31	-50:06:33.73	1.52x1.20	45	1.1x0.3	3.4x0.4	-	-	-	-	26x07	0.8x0.1	5472	0.75	-	F
74	245.52850-50.09985	16:22:6.360	-50:05:59.47	1.12x0.90	159	1.4x0.3	2.8x0.4	-	-	-	-	29x07	0.5x0.1	4062	0.87	-	F
76	245.53812-50.10246	16:22:7.710	-50:06:8.870	0.86x0.70	20	5.3x1.6	6.6x1.2	-	-	-	-	36x09	1.0x0.2	3148	0.46	-	T
77	245.50951-50.10812	16:22:2.280	-50:06:29.22	0.78x0.57	18	4.1x0.9	4.2x0.7	-	-	-	-	24x06	1.1x0.2	2666	0.24	-	F
80	245.5386-50.10443	16:22:8.130	-50:06:15.95	1.47x1.15	59	3.0x0.8	10.1x1.0	-	-	-	-	36x09	1.5x0.2	5244	0.50	-	F
81	245.51271-50.11184	16:22:3.770	-50:06:42.63	1.42x1.16	106	1.7x0.5	5.4x0.7	-	-	-	-	24x06	1.3x0.2	5220	0.39	-	F
84	245.51211-50.10846	16:22:4.110	-50:06:30.46	0.95x0.67	159	3.7x1.3	5.9x1.4	-	-	-	-	27x07	1.3x0.3	3170	0.28	-	T

F. Louvet et al.: ALMA-IMF

Table D.20: Continuation of Table D.19

n	Core name	RA	DEC	1.3 mm			3 mm			$S^{\text{int}}$	T	Mass <sup>(1)</sup>	Size <sup>(1)</sup>	$\alpha_{\text{BE}}^{(1)}$	$\alpha$	GExT2D <sup>(2)</sup>
				$a \times b$	PA	$S^{\text{Peak}}$	$S^{\text{int}}$	PA	$S^{\text{Peak}}$							
85	245.51446-50.10667	16:22:3.470	-50:06:24.02	1.27×1.18	97	1.6±0.3	5.5±0.3	-	-	25±06	1.3±0.1	5068	0.39	-	F	
88	245.54876-50.10451	16:22:11.70	-50:06:16.24	0.94×0.78	17	1.7±0.4	2.8±0.4	-	-	32±08	0.5±0.1	3500	0.91	-	T	
91	245.55637-50.10999	16:22:13.53	-50:06:35.96	1.05×0.80	42	1.0±0.2	2.3±0.3	-	-	26±07	0.5±0.1	3668	0.73	-	F	
94	245.55462-50.10766	16:22:13.11	-50:06:27.56	1.17×1.08	49	0.9±0.3	2.8±0.4	-	-	26±07	0.6±0.1	4664	0.80	-	F	
98	245.53135-50.10181	16:22:7.520	-50:06:6.510	0.83×0.73	68	3.7±1.2	5.1±0.9	-	-	35±09	0.8±0.1	3202	0.55	-	T	
99	245.55838-50.10296	16:22:14.01	-50:06:10.65	0.85×0.82	18	1.0±0.3	1.4±0.3	-	-	26±07	0.3±0.1	3476	1.14	-	F	
101	245.52670-50.10047	16:22:6.410	-50:06:1.680	1.52×1.14	39	1.1±0.4	3.4±0.5	-	-	29±07	0.7±0.1	5254	0.94	-	F	
103	245.53263-50.08669	16:22:7.830	-50:05:12.09	0.80×0.70	68	0.9±0.2	1.2±0.2	-	-	26±07	0.3±0.1	3082	1.19	-	F	
104	245.53558-50.10531	16:22:8.540	-50:06:19.12	0.93×0.81	178	3.6±1.5	5.3±1.2	-	-	38±10	0.8±0.2	3550	0.72	-	F	
105	245.53632-50.10336	16:22:8.720	-50:06:12.11	0.83×0.68	126	8.8±3.5	10.6±2.7	-	-	43±11	1.3±0.3	3062	0.39	-	T	
108	245.52463-50.10358	16:22:5.910	-50:06:12.87	1.71×1.39	46	1.2±0.4	5.6±0.6	-	-	28±07	1.2±0.1	6256	0.61	-	F	
112	245.54733-50.10810	16:22:11.36	-50:06:29.15	1.33×0.99	72	1.1±0.5	2.9±0.6	-	-	29±07	0.6±0.1	4598	0.97	-	F	
116	245.52636-50.10340	16:22:6.330	-50:06:12.24	1.24×0.99	78	1.6±0.5	3.8±0.6	-	-	29±07	0.8±0.1	4478	0.70	-	F	
6	245.54007-50.10002	16:22:9.620	-50:06:0.060	1.26×0.92	175	196.8±36.5	448.4±34.7	1.21×0.90	176	231.9±44.4	561.3±45.3	4308	-	-0.3	F	
9	245.53991-50.09967	16:22:9.580	-50:05:58.80	1.02×0.82	152	167.4±47.3	306.1±41.9	1.00×0.87	162	203.2±54.4	374.4±46.4	3706	-	-0.2	F	
10	245.53841-50.09911	16:22:9.220	-50:05:56.81	1.10×0.97	151	78.1±24.0	180.8±27.4	1.13×0.99	156	89.3±27.2	206.3±29.8	4262	-	-0.2	F	
12	245.54026-50.10047	16:22:9.660	-50:06:1.680	1.27×1.21	120	109.1±32.2	305.8±32.2	1.39×1.29	128	140.9±33.5	440.2±55.8	5178	-	-0.4	F	
13	245.53994-50.09930	16:22:9.590	-50:05:57.48	1.41×1.22	38	132.1±47.6	496.0±62.9	1.39×1.17	36	154.8±53.9	580.6±74.9	5358	-	-0.2	F	
16	245.53814-50.10138	16:22:9.150	-50:06:4.960	1.27×1.01	128	56.7±19.3	154.6±23.8	1.38×1.02	124	66.6±22.4	175.3±26.6	4574	-	-0.2	F	
17	245.53702-50.10059	16:22:8.890	-50:06:2.140	1.28×1.08	160	59.2±13.6	163.8±15.1	1.37×1.16	162	37.8±17.0	94.3±15.2	4812	-	0.7	F	
20	245.53850-50.10093	16:22:9.240	-50:06:3.350	1.30×1.16	103	37.9±14.6	107.7±13.9	1.33×1.16	105	43.5±16.5	122.4±15.3	5068	-	-0.2	F	
24	245.54270-50.09981	16:22:10.25	-50:05:59.31	1.22×0.85	156	48.8±14.9	100.8±15.3	1.33×0.83	156	41.8±16.8	83.4±16.2	4034	-	0.2	F	
27	245.54453-50.09689	16:22:10.69	-50:05:48.80	0.96×0.89	102	7.8±1.4	14.3±1.3	1.06×0.90	118	8.2±1.6	14.6±1.4	3844	-	-0.0	F	
29	245.54751-50.09975	16:22:11.40	-50:05:59.11	0.95×0.84	19	13.3±3.1	21.9±2.7	-	-	-	-	3688	-	-	F	
36	245.54432-50.09772	16:22:10.64	-50:05:51.79	1.13×1.10	131	9.4±2.3	23.0±2.3	1.36×1.30	154	7.2±2.3	16.5±1.6	4674	-	0.4	F	
40	245.55063-50.10724	16:22:12.15	-50:06:26.07	1.32×1.08	95	1.3±0.2	3.9±0.3	1.33×1.31	61	1.1±0.3	3.1±0.3	4844	-	0.3	F	
42	245.54585-50.09489	16:22:11.00	-50:05:41.59	1.12×0.91	114	2.9±0.6	5.9±0.6	1.04×0.87	103	3.4±0.5	7.1±0.6	4086	-	-0.2	F	
48	245.54487-50.10146	16:22:10.77	-50:06:5.250	0.92×0.80	38	12.9±5.7	19.2±4.4	0.97×0.80	41	15.1±5.2	22.0±3.8	3514	-	-0.2	F	
51	245.53289-50.09880	16:22:7.890	-50:05:55.69	1.24×0.98	179	3.9±1.2	8.7±1.3	1.40×1.06	177	3.9±1.2	8.9±1.0	4454	-	-0.0	F	
53	245.54888-50.09999	16:22:11.73	-50:05:59.98	0.96×0.73	144	5.1±1.1	7.2±0.9	1.22×0.88	131	4.1±1.2	5.8±0.8	3346	-	0.3	F	
55	245.54659-50.10366	16:22:11.18	-50:06:13.19	1.44×1.21	161	4.9±1.5	19.0±2.0	1.26×1.14	35	2.9±1.4	9.5±1.8	5398	-	0.8	F	
56	245.54717-50.10144	16:22:11.32	-50:06:5.170	1.64×1.37	29	5.3±1.6	22.4±1.8	1.89×1.66	12	4.2±1.7	19.0±1.6	6112	-	0.2	F	
57	245.55155-50.10056	16:22:12.37	-50:06:2.020	1.24×1.16	106	1.8±0.4	5.4±0.5	1.40×0.89	142	1.6±0.5	4.4±0.7	4988	-	0.3	F	
58	245.54399-50.09044	16:22:10.56	-50:05:25.59	1.29×1.01	117	1.0±0.3	2.8±0.4	1.22×1.16	155	1.1±0.2	2.8±0.2	4598	-	-0.0	F	
59	245.54153-50.09792	16:22:9.970	-50:05:52.52	0.94×0.86	146	11.3±5.6	18.6±4.6	1.03×0.91	151	12.3±6.8	19.4±4.8	3712	-	-0.1	F	
60	245.53882-50.10456	16:22:9.320	-50:06:16.42	1.78×1.21	140	7.0±2.6	29.3±4.0	1.86×1.27	151	7.1±2.9	29.1±4.0	5794	-	0.0	F	
64	245.54564-50.09878	16:22:10.95	-50:05:55.61	1.49×0.84	159	14.7±4.7	33.8±5.2	-	-	-	-	4268	-	-	F	
67	245.54667-50.09950	16:22:11.20	-50:05:58.19	1.14×0.88	174	8.0±3.0	16.0±2.9	1.00×0.80	62	6.6±1.8	13.2±1.8	4038	-	-	F	
69	245.54289-50.10494	16:22:10.29	-50:06:17.78	1.09×0.91	37	6.8±1.6	14.1±1.6	-	-	-	-	4070	-	0.1	F	
70	245.54669-50.10475	16:22:11.21	-50:06:17.08	1.11×0.92	43	2.1±0.4	4.7±0.5	-	-	-	-	4116	-	-	F	
82	245.52411-50.10001	16:22:5.790	-50:06:0.050	1.21×1.12	2	1.3±0.5	3.4±0.5	1.41×1.20	24	1.1±0.7	2.6±0.6	4846	-	0.3	F	
83	245.54413-50.10514	16:22:10.59	-50:06:18.51	1.20×0.97	28	4.3±1.5	9.7±1.4	0.99×0.84	45	5.0±1.9	12.0±2.3	4390	-	-0.3	F	

Table D.21: Continuation of Table D.19

n	Core name	RA	DEC	1.3 mm			3 mm			T	Mass <sup>(1)</sup>	Size <sup>(1)</sup>	$\alpha_{BE}^{(1)}$	$\alpha$	GExt2D <sup>(2)</sup>		
				a × b	PA	S <sup>Peak</sup>	a × b	PA	S <sup>Peak</sup>								
86	245.54286-50.09718	16:22:10.29	-50:05:49.83	0.94×0.84	74	4.9±2.2	8.5±1.9	1.07×0.99	151	5.0±2.3	7.5±1.5	-	-	3662	-	0.1	F
90	245.53378-50.10306	16:22:8.110	-50:06:11.02	0.96×0.80	173	3.4±1.0	5.2±0.9	-	-	-	-	-	-	3554	-	-	F
93	245.54375-50.10809	16:22:10.50	-50:06:29.12	1.29×0.94	84	1.8±0.9	2.8±0.9	1.23×0.92	74	2.5±1.1	5.5±1.2	-	-	4382	-	-0.8	F
95	245.52211-50.10055	16:22:5.310	-50:06:1.960	1.28×0.99	117	1.6±0.7	4.5±0.9	1.80×1.46	95	1.5±0.8	3.3±0.4	-	-	4518	-	0.4	F
96	245.54761-50.10307	16:22:11.43	-50:06:11.06	0.81×0.76	173	3.2±1.3	4.0±1.0	0.96×0.77	16	3.1±1.4	3.7±0.9	-	-	3268	-	0.1	F
97	245.54776-50.10350	16:22:11.46	-50:06:12.58	0.86×0.66	35	3.1±1.0	4.4±1.0	0.94×0.62	45	1.9±1.2	2.2±0.9	-	-	3036	-	0.8	F
102	245.54582-50.10286	16:22:11.00	-50:06:10.28	1.20×0.88	16	4.6±1.8	9.0±1.6	-	-	-	-	-	-	4098	-	-	F
106	245.54506-50.10387	16:22:10.82	-50:06:13.95	1.63×1.23	72	2.8±1.0	12.5±1.6	1.65×1.24	74	2.5±1.2	9.5±1.4	-	-	5682	-	0.3	F
107	245.54215-50.10035	16:22:10.12	-50:06:1.260	1.50×0.99	116	35.1±14.2	66.5±18.2	0.92×0.54	97	19.0±17.5	21.8±52.0	-	-	4786	-	1.4	F
114	245.53208-50.09852	16:22:7.700	-50:05:54.66	1.12×0.88	121	2.1±1.0	4.4±1.0	1.20×0.76	18	2.0±1.1	3.9±1.2	-	-	3992	-	0.2	F
115	245.54639-50.10552	16:22:11.13	-50:06:19.87	0.91×0.70	53	2.3±0.9	2.8±0.7	-	-	-	-	-	-	3204	-	-	F
118	245.54331-50.10828	16:22:10.39	-50:06:29.82	1.23×0.76	81	2.9±1.0	5.3±1.1	1.03×0.80	93	2.4±1.3	4.3±1.3	-	-	3736	-	0.2	F

**Notes.** The coordinates are given at the J2000 Epoch. (1) Estimated from the measures at 1.3 mm. (2) Indicates if the source found by *getsf* was also found by *GExt2D* (True or False). The \* next to the uncertainty indicates that the true value is <0.05.

Table D.22: Compact sources extracted by *getsf* in W51-IRS2, after smoothing.

n	Core name	RA [J2000]	DEC [J2000]	1.3 mm			3 mm			T [K]	Mass <sup>(1)</sup> [ $M_{\odot}$ ]	Size <sup>(1)</sup> [au]	$\alpha_{\text{BE}}^{(1)}$	$\alpha$	GExT2
				$a \times b$ ["x"]	PA [deg]	$S^{\text{Peak}}$ [mJy.Beam <sup>-1</sup> ]	$S^{\text{int}}$ [mJy]	$a \times b$ ["x"]	PA [deg]						
1	290.91688+14.518190	19:23:40.05	14:31:5.480	0.72x0.66	89	886.9±16.1	1816.0±21.5	0.64x0.55	74	82.0±8.4	151.4±11.8	0.07	3.1	T	
2	290.91647+14.518160	19:23:39.95	14:31:5.370	0.63x0.59	106	346.2±15.1	489.5±12.8	0.58x0.52	66	40.6±8.6	56.5±8.6	0.02	2.7	T	
4	290.91072+14.511610	19:23:38.57	14:30:4.178	0.74x0.61	150	70.6±1.2	193.6±2.7	0.68x0.60	118	4.7±0.2	9.6±0.3	0.08	3.7	T	
6	290.91662+14.518290	19:23:40.00	14:31:5.850	0.74x0.68	166	270.9±14.4	505.0±13.5	0.64x0.60	148	17.2±7.8	29.9±8.2	0.03	3.5	T	
7	290.91567+14.518130	19:23:39.75	14:31:5.280	0.67x0.59	69	149.3±15.5	204.0±12.0	0.72x0.54	73	9.3±5.5	12.0±4.2	0.07	3.5	T	
8	290.90916+14.518580	19:23:38.20	14:31:6.880	0.69x0.55	145	23.5±0.9	36.4±0.9	0.64x0.51	151	2.7±0.1	4.3±0.1	0.04	2.6	T	
9	290.91037+14.511330	19:23:38.49	14:30:40.77	0.71x0.66	84	18.4±0.8	35.4±0.8	0.66x0.55	162	2.0±0.2	3.5±0.3	0.05	2.8	T	
10	290.91118+14.512660	19:23:38.68	14:30:45.57	0.61x0.54	11	19.0±1.0	25.3±1.0	0.55x0.51	36	2.2±0.1	2.6±0.1	0.05	2.8	T	
11	290.91876+14.517740	19:23:40.50	14:31:3.880	0.82x0.67	139	23.3±1.6	52.4±2.0	0.87x0.67	123	2.0±0.5	4.5±0.5	0.05	3.0	T	
12	290.90858+14.518250	19:23:38.06	14:31:5.710	0.57x0.56	103	7.2±0.3	9.0±0.3	0.53x0.49	117	0.9±0.1	1.1±0.2	0.12	2.6	T	
13	290.90600+14.505230	19:23:37.44	14:30:18.83	0.71x0.59	11	22.2±1.0	38.2±1.1	0.69x0.54	7	2.6±0.2	4.3±0.2	0.01	2.7	T	
14	290.90919+14.509210	19:23:38.21	14:30:33.16	0.65x0.55	8	12.3±1.1	19.0±1.1	0.59x0.51	15	1.4±0.2	1.9±0.2	0.06	2.8	T	
15	290.91002+14.510190	19:23:38.40	14:30:36.68	0.95x0.76	47	12.4±1.2	36.5±1.7	0.88x0.76	15	1.1±0.2	2.7±0.2	0.57	3.0	T	
16	290.90873+14.518410	19:23:38.10	14:31:6.290	0.60x0.54	109	1.6±0.5	1.5±0.5	-	-	-	-	0.77	3.0	F	
17	290.92460+14.519780	19:23:41.90	14:31:11.19	1.01x0.78	46	8.4±0.6	24.8±0.8	0.73x0.54	176	0.9±0.2	2.7±0.4	0.07	2.7	T	
19	290.92493+14.519590	19:23:41.98	14:31:10.52	0.56x0.49	150	8.5±0.5	9.0±0.4	0.66x0.54	118	1.0±0.1	1.0±0.1	0.14	2.7	T	
20	290.90567+14.518290	19:23:37.36	14:31:5.860	1.64x1.12	133	2.1±0.4	9.7±1.1	-	-	-	-	0.21	2.7	F	
22	290.92557+14.511270	19:23:42.14	14:30:40.56	0.62x0.48	7	14.2±1.3	16.4±1.1	-	-	-	-	0.07	2.8	T	
23	290.92186+14.521120	19:23:41.25	14:31:16.05	0.95x0.64	106	3.8±0.2	8.2±0.3	-	-	-	-	0.17	2.7	T	
24	290.91147+14.518690	19:23:38.75	14:31:7.280	0.92x0.64	38	6.6±0.6	16.8±0.8	-	-	-	-	0.08	2.7	T	
25	290.91466+14.517600	19:23:39.52	14:31:3.360	0.66x0.56	72	18.4±2.7	31.4±3.0	-	-	-	-	0.48	2.7	T	
26	290.92090+14.509560	19:23:41.02	14:30:34.42	0.63x0.57	63	3.4±0.2	4.8±0.2	-	-	-	-	0.23	2.7	T	
27	290.90837+14.519900	19:23:38.01	14:31:11.62	1.26x0.99	90	2.8±0.2	12.0±0.3	-	-	-	-	0.15	2.7	F	
28	290.90529+14.518470	19:23:37.27	14:31:6.500	0.94x0.82	146	6.8±0.5	21.2±0.8	-	-	-	-	0.06	2.7	T	
29	290.91177+14.511220	19:23:38.83	14:30:40.38	0.58x0.50	167	7.9±1.0	8.7±0.8	0.53x0.47	55	0.9±0.1	0.9±0.1	0.12	2.7	T	
31	290.91225+14.509870	19:23:38.94	14:30:35.55	0.56x0.50	174	4.2±0.3	4.5±0.3	-	-	-	-	0.20	2.7	T	
32	290.90695+14.506490	19:23:37.67	14:30:23.36	0.69x0.54	50	13.4±1.2	20.2±1.1	0.62x0.50	24	1.7±0.2	2.3±0.2	0.05	2.7	T	
33	290.92351+14.517170	19:23:41.64	14:31:1.810	0.86x0.69	170	7.8±1.1	16.8±1.2	-	-	-	-	0.12	-	T	
34	290.92591+14.515090	19:23:42.22	14:30:54.31	0.56x0.54	8	12.1±1.8	14.0±1.4	0.59x0.43	151	1.2±1.4	1.4±1.3	0.09	2.8	T	
35	290.91218+14.511570	19:23:38.92	14:30:41.67	0.59x0.51	25	2.9±1.1	3.2±0.9	-	-	-	-	0.30	-	T	
37	290.91197+14.515950	19:23:38.87	14:30:57.43	0.93x0.77	107	1.4±0.4	3.0±0.4	-	-	-	-	0.51	-	T	
38	290.92623+14.515360	19:23:42.29	14:30:55.29	0.62x0.58	35	12.3±1.5	17.0±1.3	-	-	-	-	0.09	-	T	
40	290.92079+14.511690	19:23:40.99	14:30:42.10	0.66x0.62	126	3.0±0.3	4.6±0.2	-	-	-	-	0.26	-	T	
41	290.91618+14.518140	19:23:39.88	14:31:5.310	0.82x0.61	85	55.6±16.6	90.0±12.8	-	-	-	-	0.07	-	F	
42	290.91808+14.517960	19:23:40.34	14:31:4.670	0.78x0.67	104	13.6±2.5	25.7±2.4	-	-	-	-	0.11	-	T	
43	290.91142+14.513230	19:23:38.74	14:30:47.62	0.66x0.60	13	4.5±0.5	7.1±0.5	-	-	-	-	0.16	-	T	
44	290.92313+14.519420	19:23:41.55	14:31:9.900	0.56x0.54	148	4.7±0.6	5.5±0.5	-	-	-	-	0.19	-	T	
45	290.91842+14.517910	19:23:40.42	14:31:4.480	0.86x0.72	65	3.8±1.9	7.5±2.0	-	-	-	-	0.43	-	T	
46	290.90792+14.519910	19:23:37.90	14:31:11.69	1.58x1.27	117	1.7±0.2	11.4±0.3	-	-	-	-	0.20	-	T	
47	290.91005+14.519680	19:23:38.41	14:31:10.84	0.64x0.57	133	3.2±0.3	6.1±0.4	-	-	-	-	0.17	-	F	
48	290.91370+14.517070	19:23:39.29	14:31:1.440	0.65x0.50	22	6.9±0.8	8.3±0.6	-	-	-	-	0.15	-	T	

Table D.23: Continuation of Table D.22

n	Core name	RA	DEC	1.3 mm		3 mm		$S_{\text{int}}$	T	Mass <sup>(1)</sup>	Size <sup>(1)</sup>	$\alpha_{\text{BE}}^{(1)}$	$\alpha$	GExT2D <sup>(2)</sup>
				$a \times b$	PA	$S_{\text{Peak}}$	PA							
49	290.91144+14.512710	19:23:38.75	14:30:45.75	0.84×0.76	102	5.3±0.7	13.7±0.9	-	31±08	4.3±0.3	4246	0.12	-	T
51	290.91169+14.510730	19:23:38.81	14:30:38.64	0.63×0.50	124	5.6±0.8	6.8±0.6	-	28±07	2.4±0.2	2900	0.14	-	T
52	290.91681+14.514650	19:23:40.03	14:30:52.75	0.66×0.57	57	3.7±0.4	5.1±0.4	-	28±07	1.7±0.1	3222	0.21	-	T
53	290.91961+14.506820	19:23:40.71	14:30:24.55	0.55×0.50	156	3.7±0.4	3.9±0.3	-	28±07	1.4±0.1	2772	0.23	-	T
54	290.92473+14.508460	19:23:41.93	14:30:30.45	0.55×0.49	129	7.2±1.3	7.5±1.0	-	29±07	2.5±0.3	2748	0.13	-	T
55	290.90698+14.505980	19:23:37.68	14:30:21.51	0.62×0.57	143	9.5±1.6	12.5±1.2	-	27±07	4.5±0.4	3180	0.08	-	T
57	290.91111+14.511110	19:23:38.67	14:30:39.98	0.63×0.55	62	5.2±1.2	6.9±1.0	-	32±08	2.1±0.3	3124	0.19	-	T
59	290.90857+14.508740	19:23:38.06	14:30:31.47	0.65×0.63	158	3.5±0.5	5.0±0.4	-	28±07	1.8±0.2	3438	0.22	-	T
60	290.91182+14.511740	19:23:38.84	14:30:42.25	1.30×0.82	52	4.9±1.1	18.2±1.7	-	30±08	5.9±0.5	5162	0.11	-	T
61	290.91113+14.519010	19:23:38.67	14:31:8.440	0.58×0.49	113	3.8±0.6	4.1±0.4	-	28±07	1.4±0.1	2798	0.23	-	T
62	290.90549+14.506300	19:23:37.32	14:30:22.66	0.62×0.51	116	5.3±0.5	6.3±0.4	-	27±07	2.2±0.1	2948	0.14	-	T
63	290.92055+14.518770	19:23:40.93	14:31:7.580	0.54×0.46	127	2.3±0.2	2.3±0.2	-	29±07	0.7±0.1	2634	0.43	-	T
64	290.90540+14.507240	19:23:37.30	14:30:26.07	0.55×0.51	1	3.9±0.4	4.2±0.3	-	27±07	1.5±0.1	2836	0.21	-	T
65	290.92036+14.514100	19:23:40.89	14:30:50.75	0.60×0.57	120	2.0±0.2	2.7±0.2	-	28±07	0.9±0.1	3130	0.40	-	T
66	290.92735+14.517930	19:23:42.56	14:31:4.560	0.86×0.69	161	4.7±0.5	10.9±0.6	-	28±07	3.8±0.2	4024	0.12	-	T
67	290.92428+14.515240	19:23:41.83	14:30:54.87	0.64×0.40	174	10.4±3.6	10.1±2.9	0.8±0.4	100±50	0.9±0.2	2512	1.17	3.1	T
68	290.91492+14.517820	19:23:39.58	14:31:4.160	0.81×0.69	47	11.6±4.0	20.3±3.2	-	45±11	4.2±0.7	3920	0.17	-	T
69	290.91824+14.517600	19:23:40.38	14:31:3.370	0.74×0.57	113	8.2±2.1	12.1±1.7	-	39±10	2.8±0.4	3380	0.19	-	T
70	290.92749+14.519810	19:23:42.60	14:31:11.32	0.60×0.54	85	5.4±0.7	6.9±0.6	-	28±07	2.4±0.2	3014	0.14	-	T
71	290.90752+14.507350	19:23:37.81	14:30:26.47	0.59×0.57	115	4.6±0.8	5.6±0.6	-	27±07	2.1±0.2	3114	0.16	-	T
72	290.92342+14.518720	19:23:41.62	14:31:7.370	0.63×0.53	113	4.9±1.0	6.0±0.8	-	29±07	2.0±0.3	3022	0.18	-	T
73	290.91733+14.517590	19:23:40.16	14:31:3.330	0.63×0.47	172	6.4±2.1	7.1±1.6	-	44±11	1.4±0.3	2806	0.35	-	T
74	290.91143+14.509500	19:23:38.74	14:30:34.20	0.59×0.52	11	1.4±0.2	1.7±0.1	-	27±07	0.6±0.1*	2920	0.52	-	T
75	290.91764+14.521310	19:23:40.23	14:31:16.71	0.91×0.75	173	4.0±0.9	9.3±0.9	-	30±08	2.9±0.3	4302	0.18	-	T
76	290.90740+14.506940	19:23:37.78	14:30:24.97	0.77×0.51	37	7.4±1.3	12.2±1.3	-	27±07	4.5±0.5	3150	0.08	-	T
77	290.91301+14.518340	19:23:39.12	14:31:6.030	1.01×0.71	141	5.2±0.8	14.4±1.0	-	32±08	4.3±0.3	4308	0.13	-	T
78	290.90365+14.517420	19:23:36.88	14:31:2.700	0.63×0.51	129	5.2±0.8	6.2±0.6	-	27±07	2.2±0.2	2944	0.14	-	T
79	290.90846+14.504780	19:23:38.03	14:30:17.21	0.57×0.44	159	6.3±0.7	6.8±0.5	-	27±07	2.4±0.2	2578	0.12	-	T
80	290.90621+14.505490	19:23:37.49	14:30:19.76	0.85×0.69	51	6.6±1.1	12.7±1.0	-	27±07	4.6±0.4	4016	0.10	-	T
81	290.90828+14.508280	19:23:37.99	14:30:29.79	1.38×0.85	54	4.2±0.7	15.1±1.0	-	27±07	5.5±0.3	5384	0.11	-	T
84	290.92246+14.520940	19:23:41.39	14:31:15.37	0.79×0.65	39	1.2±0.2	2.3±0.2	-	29±07	0.8±0.1	3734	0.57	-	T
85	290.90905+14.506620	19:23:38.17	14:30:23.82	0.77×0.57	29	3.7±0.5	6.1±0.5	-	27±07	2.2±0.2	3408	0.17	-	T
86	290.91150+14.517300	19:23:38.76	14:31:2.290	1.05×0.83	133	1.8±0.4	5.8±0.5	-	28±07	2.0±0.2	4834	0.28	-	T
87	290.90729+14.510200	19:23:37.75	14:30:36.72	0.78×0.69	81	1.4±0.2	2.8±0.3	-	27±07	1.0±0.1	3884	0.41	-	T
88	290.90479+14.518210	19:23:37.15	14:31:5.570	0.70×0.64	3	2.8±0.5	4.1±0.4	-	27±07	1.5±0.1	3552	0.26	-	T
89	290.92006+14.513220	19:23:40.82	14:30:47.60	0.77×0.65	154	2.0±0.5	3.6±0.5	-	28±07	1.2±0.2	3700	0.35	-	T
90	290.92633+14.515710	19:23:42.32	14:30:56.55	0.76×0.65	9	5.8±1.4	11.4±1.4	-	32±08	3.4±0.4	3720	0.14	-	T
91	290.91255+14.515000	19:23:39.01	14:30:53.99	0.69×0.59	174	1.7±0.3	2.4±0.3	-	28±07	0.8±0.1	3364	0.46	-	T
92	290.92282+14.525440	19:23:41.48	14:31:31.59	0.78×0.53	27	1.6±0.3	2.1±0.2	-	28±07	0.7±0.1	3248	0.50	-	T
94	290.91723+14.517320	19:23:40.13	14:31:2.350	0.57×0.50	14	5.2±1.5	5.6±1.2	-	44±11	1.1±0.2	2824	0.44	-	T
95	290.90672+14.506980	19:23:37.61	14:30:25.14	0.70×0.54	171	4.1±1.2	5.4±0.9	-	27±07	2.0±0.3	3172	0.17	-	T
97	290.92431+14.517550	19:23:41.83	14:31:3.190	0.80×0.61	166	3.3±0.9	5.2±0.8	-	30±08	1.6±0.2	3586	0.27	-	T

Table D.24: Continuation of Table D.22

n	Core name	1.3 mm			3 mm			$S^{\text{int}}$	T	Mass <sup>(1)</sup>	Size <sup>(1)</sup>	$\alpha_{\text{BE}}^{(1)}$	$\alpha$	GExt2D <sup>(1)</sup>
		RA	DEC	PA	$a \times b$	PA	$S^{\text{Peak}}$							
99	290.92043+14.513530	19:23:40.90	14:30:48.70	65	0.66×0.63	1.9±0.6	2.8±0.5	-	29±07	0.9±0.2	3454	0.43	-	T
100	290.90944+14.509660	19:23:38.26	14:30:34.78	53	0.64×0.59	2.7±1.1	3.7±0.8	-	29±07	1.2±0.3	3292	0.32	-	T
101	290.91386+14.517350	19:23:39.33	14:31:2.440	103	0.66×0.65	3.1±1.1	4.5±0.9	-	34±09	1.2±0.2	3512	0.39	-	T
102	290.91539+14.521770	19:23:39.69	14:31:18.36	86	0.72×0.58	1.9±0.5	2.7±0.4	-	30±08	0.9±0.1	3364	0.47	-	T
104	290.90931+14.520160	19:23:38.23	14:31:12.59	4	0.86×0.67	1.7±0.4	3.6±0.4	-	27±07	1.3±0.1	3926	0.35	-	T
105	290.92552+14.519050	19:23:42.12	14:31:8.580	53	1.35×1.13	1.3±0.4	6.3±0.6	-	29±07	2.1±0.2	6466	0.36	-	F
106	290.92533+14.515250	19:23:42.08	14:30:54.89	69	0.92×0.74	3.5±1.5	8.2±1.5	-	32±08	2.5±0.5	4300	0.22	-	T
107	290.90723+14.505910	19:23:37.73	14:30:21.27	16	0.74×0.63	6.8±1.9	12.1±1.9	-	27±07	4.4±0.7	3584	0.09	-	T
108	290.92878+14.515980	19:23:42.91	14:30:57.54	172	1.73×1.21	3.0±0.8	14.5±1.6	-	20±05	7.8±0.8	7352	0.08	-	F
109	290.91096+14.515680	19:23:38.63	14:30:56.45	125	0.99×0.68	1.2±0.2	2.6±0.2	-	28±07	0.9±0.1	4144	0.53	-	T
111	290.90842+14.517400	19:23:38.02	14:31:2.650	29	1.53×1.17	1.2±0.3	6.9±0.5	-	27±07	2.5±0.2	6902	0.30	-	F
114	290.90989+14.510420	19:23:38.37	14:30:37.52	33	0.76×0.68	2.5±1.0	4.2±0.8	-	31±08	1.3±0.2	3816	0.38	-	F
117	290.91145+14.510910	19:23:38.75	14:30:39.28	139	0.75×0.56	3.3±1.4	4.3±1.1	-	29±07	1.4±0.4	3320	0.28	-	T
119	290.90948+14.507840	19:23:38.28	14:30:28.24	37	1.03×0.72	1.4±0.5	3.5±0.6	-	27±07	1.3±0.2	4376	0.37	-	F
122	290.91432+14.517630	19:23:39.44	14:31:3.480	121	1.04×0.79	3.3±1.6	8.5±1.6	-	39±10	2.0±0.4	4666	0.38	-	F
123	290.91431+14.517970	19:23:39.43	14:31:4.690	79	0.90×0.74	2.6±1.3	5.9±1.3	-	40±10	1.3±0.3	4252	0.50	-	F
3	290.92443+14.515750	19:23:41.86	14:30:56.71	145	0.56×0.50	21.7±0.7	23.9±0.6	30.2±0.2	-	-	2818	-	-0.3	F
5	290.91593+14.518080	19:23:39.82	14:31:5.090	35	0.71×0.65	231.9±16.5	361.6±13.2	77.8±5.2	-	-	3604	-	1.9	F
18	290.91641+14.518940	19:23:39.94	14:31:8.190	23	0.94×0.86	48.8±15.1	125.6±14.4	127.8±11.5	-	-	4792	-	-0.0	F
36	290.91644+14.519200	19:23:39.95	14:31:9.140	140	1.03×0.79	36.2±15.1	90.8±14.5	102.9±19.1	-	-	4656	-	-0.2	F
56	290.91745+14.518760	19:23:40.19	14:31:7.550	137	1.10×0.86	14.9±5.5	48.0±6.3	50.2±5.2	-	-	5058	-	-0.1	F
58	290.91511+14.525150	19:23:39.63	14:31:30.53	109	0.73×0.66	1.2±0.1	2.1±0.1	2.8±0.1	-	-	3706	-	-0.4	F
98	290.92390+14.514700	19:23:41.74	14:30:52.90	76	0.61×0.55	2.6±1.0	3.4±0.8	-	-	-	3086	-	-	F
113	290.91700+14.520310	19:23:40.08	14:31:13.13	60	0.55×0.46	2.7±0.9	2.5±0.7	-	-	-	2634	-	-	F
118	290.91879+14.519040	19:23:40.51	14:31:8.560	20	0.93×0.89	1.6±0.7	4.7±1.0	-	-	-	4894	-	-	F
124	290.91453+14.519370	19:23:39.49	14:31:9.720	164	1.00×0.60	2.7±1.0	5.4±1.1	-	-	-	3858	-	-	F

A&amp;A proofs: manuscript no. CMF-in-ALMA-IMF

**Notes.** The coordinates are given at the J2000 Epoch. (1) Estimated from the measures at 1.3 mm. (2) Indicates if the source found by *getsf* was also found by *GExt2D* (True or False). The \* next to the uncertainty indicates that the true value is <0.05.



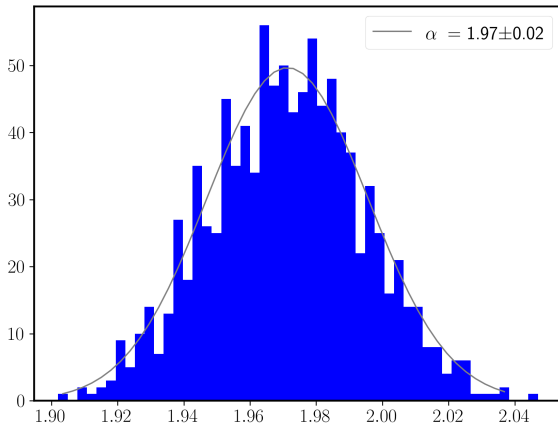


Fig. E.1: The plot shows the probability density function for a power-law on the  $10^3$  draws to estimate the fit error on the CMF (see Sect. 5.2).

### Appendix E: Monte Carlo simulations for fitting the slope of the CMF

In this Appendix we display in Fig. a:incertitudes the functional parameters retrieved when adjusting a power-law (in blue), an exponential (in green), or a log-normal (in orange) with the MLE technique (see Sect. 5.2.1).